# INVESTIGATION OF GLASS AQUEOUS CORROSION USING SURFACE CHARACTERIZATION TOOLS

BY

YUXUAN GONG

A THESIS

SUBMITTED TO THE FACULTY OF

ALFRED UNIVERSITY

IN PARTIAL FULFILLMENT OF THE REQUIREMENTS
FOR THE DEGREE OF

DOCTOR OF PHILOSOPHY

IN

GLASS SCIENCE

ALFRED, NEW YORK

OCTOBER, 2016

INVESTIGATION OF GLASS AQUEOUS CORROSION USING

SURFACE CHARACTERIZATION TOOLS

BY

YUXUAN GONG

B.S. SHAANXI UNIVERSITY OF SCIENCE & TECHNOLOGY (2010)

M.S. UNIVERSITY OF CINCINNATI (2013)

SIGNATURE OF AUTHOR _____

APPROVED BY_____
ALASTAIR N. CORMACK, ADVISOR

_____
SCOTT T. MISTURE, ADVISORY COMMITTEE

_____
S.K. SUNDARAM, ADVISORY COMMITTEE

_____
ALEXIS G. CLARE, ADVISORY COMMITTEE

_____
CHAIR, ORAL THESIS DEFENSE

ACCEPTED BY _____
ALASTAIR N. CORMACK, DEAN
KAZUO INAMORI SCHOOL OF ENGINEERING

ACCEPTED BY _____
NANCY J. EVANGELISTA, ASSOCIATE PROVOST
FOR GRADUATE AND PROFESSIONAL PROGRAMS
ALFRED UNIVERSITY

# ACKNOWLEDGMENTS

All or nothing. In 2012, I made the decision to give up the near completion Ph.D degree in University of Cincinnati and came to Alfred University in the pursuit of my interests in glass science. I have experienced success and failures with tears and joys throughout my Ph.D study in Alfred University. It was quite a journey filled with happiness, bitterness, and hard-knocks. I would like to express my deepest thanks to my academic advisor Dr. Alastair N. Cormack, whose guidance and support made me a qualified glass scientist. Dr. Nathan P. Mellott, thank you for guidance as my advisor during your time in Alfred University. I would also like to thank my committee members for spending time with me in planning and discussing my thesis work. Thank you, Dr. Scott T. Misture, Dr. S.K. Sundaram, and Dr. Alexis G. Clare. Particularly, Dr. Scott T. Misture spent countless hours discussing with me on various aspects of XRR and XDS. Additionally, I would like to express my gratitude for the companionship and friendship from my friends and labmates, especially my best friend Chokchai Yatongchai and Peng Gao.

I would like to thank my parents and parents-in-law for their wholehearted support and unconditional love. I am greatly in debt of my beloved wife Bo Pang who supports me unconditionally through the hardships. Bo, you and our daughter Maggie are the anchor of my life and I owe you both so much. Last but not least, I thank God for this wonderful journey and the journeys waiting in the next chapter of my life.

# TABLE OF CONTENTS


**Page**

Acknowledgments ..... iii

Table of Contents ..... iv

List of Tables ..... vii

List of Figures ..... ix

Abstract ..... xiv

**INTRODUCTION ..... 1**

**CHAPTER I. AQUEOUS CORROSION OF NUCLEAR WASTE GLASSES: APPLICATION AND ADDITION OF SURFACE CHARACTERIZATION TOOLS ..... 3**

1. Introduction ..... 3

2. What do we know about the interaction between "aqua" and glass? ..... 5

3. Probing the chemical and morphological information of altered glass with surface characterization tools ..... 11

3.1 Electron beam based characterization techniques ..... 11

3.2 Depth profiles of altered glass using SIMS ..... 13

3.3 Characterization of altered glass surface using XRR, AFM, and Interferometry ..... 16

4. What additions of advanced surface characterization tools advanced our understanding of glass corrosion? ..... 21

Conclusion ..... 25

References ..... 26

**CHAPTER II. QUANTITATIVE MORPHOLOGICAL AND COMPOSITIONAL EVALUATION OF LABORATORY PREPARED ALUMINOBOROSILICATE GLASS SURFACES ..... 34**

1. Introduction ..... 34

2. Materials and Methods ..... 37

2.1 Glass Melting and Bulk Glass Composition Analysis ..... 37

2.2 Bulk Glass Thermal Analysis ..... 37

2.3 Glass Surface Preparation ..... 38

2.4 Glass Surface Composition ..... 39

2.5 Glass Surface Morphology ..... 40

3. Results and Discussion ..... 43

3.1 Bulk Glass Composition ..... 43

3.2 Thermal analysis of bulk ISG glass ..... 44
3.3 XPS analysis of ISG glass surfaces ..... 45
3.4 AFM imaging & statistics of melt/polished ISG glass surfaces ..... 49
3.5 Power spectral density (PSD) analysis of ISG glass surfaces ..... 53
Conclusions ..... 60
References ..... 60
**CHAPTER III. A LEAP TOWARDS THE UNDERSTANDING OF GLASS DISSOLUTION: A NOVEL ATOMIC FORCE MICROSCOPY APPROACH ..... 67**
1. Introduction ..... 67
2. Materials and Methods ..... 72
2.1 Characterization of bulk glass and preparation of melt surface ..... 72
2.2 Corrosion experiment ..... 73
2.3 Materials of masking and strategy of post-reaction exfoliation ..... 75
2.4 X-ray photoelectron spectroscopy ..... 77
2.5 Atomic force microscopy ..... 79
2.6 Recession rate measurement and error analysis ..... 81
3. Results ..... 83
3.1 Evaluation of experimental methods, strategies and hypotheses ..... 83
3.2 Surface retreat rates and dissolution rates ..... 87
3.3 Compositional and topographical evolution of reacted glass surfaces ..... 93
4. Discussion ..... 100
4.1 Validation of experimental method ..... 100
4.2 Kinetics and mechanisms of glass corrosion at pH2, 7 and 10 ..... 103
4.3 Correlations between glass dissolution and roughening ..... 106
Conclusions ..... 110
References ..... 111
**CHAPTER IV. NEW EVIDENCE OF THE INTERFACIAL DISSOLUTION REPRECIPITATION MECHANISM OF SILICA LAYER FORMATION DURING GLASS CORROSION: INSIGHT FROM SYNCHROTRON RADIATED X-RAY REFLECTIVITY AND DIFFUSE SCATTERING ..... 122**
1. Introduction ..... 122
2. Materials and methods ..... 124
2.1 Sample preparation ..... 124
2.2 Synchrotron radiated X-ray reflectivity and X-ray diffuse scattering ..... 126
2.3 X-ray photoelectron spectroscopy ..... 128
3. Results and discussion ..... 130

3.1 Identification of a textured, dense silica gel and a de-alkalized glass without density-gradient ..... 130
3.2 Determination and simulation of the origin of the dense silica layer ..... 138
3.3 Comparison between modeled and measured surface composition ..... 141
Conclusions ..... 143
References ..... 144
**APPENDIX A. SURFACE ROUGHNESS MEASUREMENTS USING POWER SPECTRUM DENSITY ANALYSIS WITH ENHANCED SPATIAL CORRELATION LENGTH ..... 147**
Introduction ..... 147
Experimental Methods ..... 150
Atomic force microscopy ..... 150
Theory ..... 151
Results and Discussion ..... 155
Conclusions ..... 161
References ..... 161
**APPENDIX B. AFM IMAGES AND XPS DEPTH PROFILES OF CORRODED ISG MELT SURFACES AND POLISHED SURFACES ..... 170**
Materials and Methods ..... 170
AFM Images of Corroded Glass Surfaces ..... 173
XPS Depth Profiles ..... 174
**APPENDIX C. DETAILED CHEMICAL COMPOSITION OF REACTED ALUMINOBOROSILICATE GLASS SURFACES IN CHAPTER III ..... 176**
**APPENDIX D. FITTED PARAMETERS OF XRR/XDS CURVES ..... 177**

# LIST OF TABLES

**Page**

Table 2.1 Composition of Melt and Polished ISG Glass Surfaces ..... 44

Table 2.2 Fitting Coefficients of PSD Spectra of Melt and Polished ISG Glass Surfaces 52

Table 4.1 Summary of the Peak Positions and FWHMs of the Masked Glass Surface (after exfoliation), No Variation of Values were Observed as a Function of Reaction Time ..... 86

Table 4.2 Summary of Surface Retreat Rates and their Corresponding Fitting Rate Laws at Different pHs ..... 92

Table 4.3 Summary of Dissolution Rates and their Corresponding Fitting Rate Law at Different pHs ..... 92

Table 4.1 Composition (wt%) of the SLS and D263 Bulk Glass using Spectrochemical Analysis ..... 124

Table 4.2 Variations of Solution pH (as measured at 90 $^{o}$C) as a Function of Reaction Time for SLS and D263 Experiments ..... 125

Table 4.3 Composition of the Outermost Surface of SLS and D263 Glass Samples after Different Reaction Times. Errors are Generated by Probing Five Different Spots on an Identical Glass Sample ..... 132

Table 4.4 The Calculated Composition Range of the Outermost Glass Surface after the Formation of Dense Silica Layer Occurs ..... 143

Table A.1 Fitting Coefficients of PSD Spectra of 1 μm Scans ..... 166

Table A.2 Fitting Coefficients of PSD Spectra of 5 μm Scans ..... 167

Table A.3 Fitting Coefficients of PSD Spectra of 10 μm Scans ..... 168

Table A.4 Fitting Coefficients of Combined PSD Spectra ..... 169

Table C.1 Chemical Composition of Reacted Glass Surfaces in Buffered pH2 Solution ..... 176

Table C.2 Chemical Composition of Reacted Glass Surfaces in Buffered pH7 Solution ..... 176

Table C.3 Chemical Composition of Reacted Glass Surfaces in Buffered pH10 Solution ..... 176

Table D.1 Summary of Fitted Parameters of XRR/XDS Curves of SLS Glass Samples177

Table D.2 Summary of Fitted Parameters of XRR/XDS Curves of D263 Glass Samples ..... 177

# LIST OF FIGURES

**Page**

Figure I.1 Time sequence of different rate regimes and sodium and silicon concentrations in solution: I – initial diffusion, II – initial rate, III – rate drop, IV – residual rate, V – resumption of alteration in particular conditions. Courtesy of Gin et. al. [11]. ..... 6

Figure I.2 Schematic drawing of the surface region of an altered glass. Courtesy of Geisler et. al. [9]. ..... 8

Figure I.3 Schematic outline of the proposed interface-coupled glass dissolution–silica reprecipitation process. Courtesy of Geisler et. al. [10]. ..... 9

Figure I.4 Optical images of (a) an unreacted and (b) a reacted glass cuboid in aqueous solution. (c) SE image of reacted glass cuboid surface in (b). (d) BSE image of the cross section of the cuboid in (b), inset shows the Si spherules. (e) BSE image of the corrosion zone (pz: outer plane; ptz: oscillating patterned zone; p: pristine bulk glass) and its corresponding EDX line profile. (f) BSE image of another reacted glass cuboid. (g) BSE image of a 2500 year old, and naturally altered glass. Courtesy of Geisler et. al. [9]. ..... 12

Figure I.5 Elemental profiles of international simple glass corroded in pH=7 solution for 209 days, with deuterium dioxide and dyes as tracers. Courtesy of Gin et. al. [27]. ..... 14

Figure I.6 a) The total alkali intensity normalized to Al across the sample depth for the CJ-6 (a simplified nuclear waste reference glass to SON68) samples and b) the profiles of $^{6}$Li, $^{7}$Li, and Na normalized to Al for the CJ-6 sample after 89.0 days of contact with $^{6}$Li solution. The intensities have been normalized to the $^{27}$Al intensity as a function of depth. Courtesy of Neeway et. al. [37]. ..... 15

Figure I.7 The morphological evolution and corrosion mechanism of a French nuclear waste glass (SON68) summarized from XRR measurement. Courtesy of Rebiscoul et. al. [38]. ..... 16

Figure I.8 Atomic force microscopy images and corresponding RMS values of CAS1 (a calcium aluminosilicate glass) fiber surfaces; (a) unreacted, (b) reacted pH 1 100 h, (c) reacted pH 6.4 100 h, and (d) reacted pH 9 100 h. All images are 500 nm × 500 nm with z-range = 10 nm. Courtesy of Mellott and Pantano [44]. ..... 19

Figure I.9 Three-dimensional interferometer images (A and C) and corresponding height profiles (B and D) of two 360 × 270 μm areas on a glass monolith surface. Courtesy of Icenhower and Steefel [48]. ..... 20

Figure I.10 NDP profile of 17.5 h leach specimen. Courtesy of Trivelpiece et. al [50]..... 22

Figure I.11 Element-specific atom maps from a subsection of an APT reconstruction of the hydrated glass/pristine glass interface in SON68. Courtesy of Gin et. al. [51]. ..... 24

Figure I.12 a)Three-dimensional chemical maps for B and Ca b) Chemical profiles derived from three-dimensional chemical maps, extending from the altered zone to the pristine glass (note two different ordinate scales, depending on element). Courtesy of Hellmann et. al. [1]..... 24

Figure II.1 Thermal expansion curve and differential thermal analysis curve for ISG glass..... 45

Figure II.2 3-D surface topography of ISG glasses; (a) micro cloth polished, (b) micro cloth polished & etched, (c) trident cloth polished, (d) trident cloth polished & etched, (e) 675 $^{o}$C melt process, (f) 700 $^{o}$C melt process and (g) 725 $^{o}$C melt process. Scan area of all images are 1μm × 1μm with a 25nm z-scale. ..... 50

Figure II.3 The experimental PSD profiles of all ISG glass surfaces. ..... 53

Figure II.4 Fitting of experimental PSD profile of 725 $^{o}$C melt processed ISG glass surfaces using both the Fractal model and ABC (k-correlation) model. ..... 54

Figure II.5 Fitting of the experimental PSD profiles of (a) 675 $^{o}$C melt surface, (b) 675 $^{o}$C melt surface with feature removal, (c) 700 $^{o}$C melt surface and (d) 700 $^{o}$C melt surface with feature removal using the Fractal model and ABC (k-correlation) model. ..... 56

Figure II.6 Fitting of the experimental PSD profiles of (a) micro cloth polished, (b) micro cloth polished & etched, (c) trident cloth polished and (d) trident cloth polished & etched ISG glass surfaces using the Fractal model and ABC (k-correlation) model. ..... 58

Figure III.1 Schematic of experimental strategy upon morphological measurement of corrosion rate. ..... 75

Figure III.2 Animation of exfoliating the polymeric composite mask from the glass substrate. ..... 77

Figure III.3 Image (left) of the interface between reacted area and masked area (post-exfoliation) as obtained from optics attached to AFM, the contrast of image was enhanced by PhotoShop®; plot (right) of the line profile of the reacted/masked glass interface subtracted from AFM image and its corresponding fitting. ..... 79

Figure III.4 C1s spectra of a) masked glass surface (post exfoliation) and b) reacted glass surface. ..... 85

Figure III.5 Measured value of height standard as a function of scanning cycle; inset is the 20 μm X 20 μm AFM image of the height standard in the shape of cylindrical pillar (colored vertical scale: -25 to 25 nm). ..... 87

Figure III.6 Representative AFM image and corresponding fitting of surface retreat of glass coupon reacted at a) pH=2, 25 $^{o}$C for 120 hours, b) pH=7, 90 $^{o}$C for 96 hours and c) pH=10, 25 $^{o}$C for 24 hours. ..... 89

Figure III.7 Surface retreat of glass coupon reacted in pH=2, pH=7, and pH=10 as a function of reaction time. ..... 90

Figure III.8 Comparison of dissolution rates (star) obtained in this study comparing to literature values (solid cube) obtained from glasses of similar composition; dissolution rates were plotted as a function of pH. ..... 93

Figure III.9 Composition of reacted glass surface as a function of reaction time; upper row is from the glass coupon reacted at pH=2, 25 $^{o}$C; middle row is from the glass reacted at pH=7, 90 $^{o}$C; bottom row is from the glass coupon reacted at pH=10, 25 $^{o}$C. ..... 94

Figure III.10 Topography of reacted glass surface; upper row is the topographies of reacted glass coupon at pH=2, middle row is the topographies of reacted glass coupon at pH=7, and lower row is the topographies of reacted glass coupon at pH=10; each column of topography represents a close value of surface retreat from each image. ..... 97

Figure III.11 Equivalent RMS roughness vs reaction time of reacted area of glass coupon reacted at pH=2 (black), pH=7 (olive), and pH=10 (orange); lines are the simulated curve using the sigmoidal logistic function, the simulation can model the maximum roughening rate, initial and final surface roughness value. ..... 98

Figure III.12 Plots of PSD profiles obtained from the AFM image of glass coupons reacted at a) pH2, b) pH7 and c) pH10. ..... 99

Figure III.13 Schematic showing the surface roughness after a certain period of time of reaction Δt. Surface profile before Δt is the left schematic, and surface profile after Δt is the right schematic. ..... 107

Figure IV.1 (a) XRR curve, (b) XDS curve at low angle, (c) XDS curve at high angle of pristine SLS glass; (d) XRR curve, (e) XDS curve at low angle, and (f) XDS curve at high angle of pristine D263 glass. ..... 131

Figure IV.2 (a) XRR curve, (b) XDS curve at low angle, (c) XDS curve at high angle of SLS glass reacted in dilute HCl for 150 hours; (d) XRR curve, (e) XDS curve at low angle, and (f) XDS curve at high angle of D263 glass reacted in dilute HCl for 250 hours. Both sets of curves were the first observation of a dense silica layer. ..... 134

Figure IV.3 (a) roughness and density of layers as a function of reaction time glass, (b) thickness of layers as a function of reaction time for test performed on SLS glass; (c) roughness and density of layers as a function of reaction time glass, (d) thickness of layers as a function of reaction time for test performed on D263 glass. Lines are guides to eyes in exception of the dashed lines used to fit layer#1 thickness prior to the formation of layer#2. ..... 135

Figure IV.4 The schematic of the cross-section of the SLS and D263 sample at different time and construction of layers. ..... 137

Figure IV.5 The modeled thickness of de-alkalized glass as a function of time under two different mechanisms. Red line: recondensation of the de-alkalized glass; black line: precipitation of dense silica layer from bulk solution. The insets show the corresponding mechanism of dense silica layer formation, particularly the recondensation of the de-alkalized glass mechanism is associated with the dense silica layer thickness. ..... 139

Figure IV.6 The schematics of a corroded glass sample cross-section after forming a textured (zigzag shaped) dense silica gel. ..... 142

Figure A.1 Exemplary AFM images of TipCheck standard captured at a) 1 μm scan scale, b) 5 μm scan scale and c) 10 μm scan scale. ..... 155

Figure A.2 PSD profiles of a) 1 μm scan scale, b) 5 μm scan scale and c) 10 μm scan scale at different scan cycles. ..... 157

Figure A.3 PSD profile of a) 1$^{st}$ scan performed at 1 μm, 5 μm and 10 μm scan scale, b) algorithm combined 1$^{st}$ scan of 1 μm, 5 μm and 10 μm scan scale with k-correlation model fitting. ..... 158

Figure A.4 Exemplary fittings of 1st scan PSD profiles at a) 1 μm scan scale (fractal model and k-correlation model), b) 5 μm scan scale (k-correlation model) and c) 10 μm scan scale (k-correlation model). ..... 159

Figure B.1 Atomic force micrographs in 1 μm X 1 μm of ISG glass a) melt surface reacted in acid for 25 days, b) melt surface reacted in neutral for 45 days and c) pristine fracture surface reacted in acid for 15 days; all presented micrographs show clearly identified pits. ..... 173

Figure B.2 Atomic force micrograph of a) polished ISG glass surface reacted in acid for 45 days and b) polished ISG glass surface reacted in neutral for 45 days.... 173

Figure B.3 XPS depth profiling of (a) unreacted melt ISG glass surface, (b) melt ISG glass surface reacted in acid for 15 days, (c) melt ISG glass surface reacted in DI-water for 15 days, (d) melt ISG glass surface reacted in acid for 45 days and (e) melt ISG glass surface reacted in DI-water for 45 days. ..... 174

Figure B.4 XPS depth profiling of (a) unreacted polished ISG glass surface, (b) polished ISG glass surface reacted in acid for 15 days, (c) polished ISG glass surface reacted in DI-water for 15 days, (d) polished ISG glass surface reacted in acid for 45 days and (e) polished ISG glass surface reacted in DI-water for 45 days. ..... 175

# ABSTRACT

The aqueous corrosion of glass is of considerable interest given its critical role in industrial applications, biomedical processes, and carbon dioxide sequestration in earth's crust. Particularly, a thorough understanding of corrosion of nuclear waste form glass is a prioritized task for its use in the application of nuclear waste storage under current energy demands. The modifier ions in the glass network exchange with hydrogen species upon contact with aqueous solution, and this ion-exchange process leads to the dissolution of Si from the glass network. In order to quantify the kinetics of glass dissolution, phenomenological observations of corroded glass has led to the discovery of a hydration coupled ion-exchange mechanism of glass corrosion. However, those observations were mostly based on the corrosion of pulverized glasses or bulk glasses of interest and lacked the use of surface characterization tools in investigating the glass corrosion behavior. In this study, attention was focused on how surface characterization techniques can contribute to the understanding of glass corrosion. Firstly, a series of glass surface finishing techniques was evaluated both compositionally and morphologically using X-ray photoelectron spectroscopy and atomic force microscopy. Also, advanced fractal algorithms were used when analyzing the AFM images in search of an atomically smooth glass surface with surface composition close to the bulk composition. For the very first time, an aluminoborosilicate glass melt surface prepared by heat treatment was used to develop a novel method of measuring glass dissolution rates and monitoring surface roughening behavior via AFM. The obtained glass dissolution rate (via AFM) is similar to the reported dissolution rates of other glasses with similar composition. Additionally, it was found that the corrosion of glass can lead to the roughening of glass surfaces. A similar relationship was observed using synchrotron radiated X-ray reflectivity and diffuse scattering. The XRR and XDS study of two different flat panel silicate glasses highlights a new series of evidence favoring the interfacial dissolution and reprecipitation mechanism of glass dissolution. The XRR/XDS evidence in favor of this mechanism is also supported by XPS data and associated calculations.

# INTRODUCTION

Silicate minerals are naturally abundant on the earth's crust, and such abundance led to the development of materials such as ceramics, glass, cement, etc. Significant progress has been achieved upon development of silicate based materials, which now have become a major materials category in daily life (e.g. electrical circuits, silicon processors, panel glasses and crystal lenses in a modern smart phone). However, although not obvious, silicates degrade when being exposed to atmosphere or aqueous media. Particularly, the degradation or corrosion of silicate glasses is of considerable interest due to its critical role in storing nuclear wastes. In a typical strategy of storing nuclear wastes, the radioactive nuclear waste is vitrified with a silicate matrix and stored in a deep repository. The modifier ions in the nuclear waste form glass exchange with hydrogen species (either from the atmosphere or groundwater), and this ion-exchange process leads to the breakdown of silica networks as well as leakage of radioactive elements. Thus, a detailed understanding of the kinetics, phenomena, and mechanisms of glass corrosion is critical prior to the use of nuclear energy as a sustainable and renewable energy source.

It was found that the ion-exchange process during glass corrosion forms an amorphous silica gel layer on top of the de-alkalized glass (as a result of ion-exchange). The silica gel layer has been given a lot of attention in various glass corrosion studies due to its role as a diffusion barrier for the hydration process. The findings from these studies were based on correlating the phenomenological observations on monoliths (SEM, EDS and SIMS) and the ion release data of pulverized glass. However, the glass surface experiences morphological evolution (particularly roughening behavior) when being attacked by water. The morphological evolution of glass surfaces increases the surface area, changes the properties of glass surfaces, and further introduces possible errors when accounting for the dissolution rate. A detailed study solving the "evolving glass surface area" problem has yet to be reported and evaluated with careful attention. This study attempts to solve this problem in glass corrosion studies using surface sensitive characterization techniques such as AFM and XPS.

For decades, it was believed that the formation of the silica gel layer is due to the restructuring of de-alkalized glass. Models were developed using this hydration coupled ion-exchange mechanism in order to kinetically estimate the long term behavior (millions of years) of nuclear waste forms. However, recent studies using atom probe tomography (APT) and nanometer resoluted secondary ion mass spectrometry (SIMS) suggested that a dominant glass corrosion mechanism, so-called interfacial dissolution and reprecipitation, was promising. Instead of having a corroded glass surface with a diffusion profile of elemental concentrations, it was found that the interface between the silica gel and the pristine glass was sharp. However, the interfacial dissolution and reprecipitation mechanism was discovered using atom probe tomography, which is notoriously difficult to use and subject to errors (e.g. sample preparation and error analysis). X-ray reflectometry and diffuse scattering, as established characterization tools, can be useful to test the interfacial dissolution and reprecipitation mechanism given their sensitivity in measuring density, thickness and roughness of surface layers. In this study, XRR and XDS were used to test the theory of interfacial dissolution reprecipitation. Also, the densities and compositions of observed surface layers were calculated using the XRR/XDS and XPS data to establish the correctness of the model used for XRR/XDS simulation.

The purpose of this study is summarized as follows:

- Evaluate the glass surface finishing techniques such as polishing, etching and heat treatment in search for a method of obtaining atomically smooth glass surfaces.
- Develop a method of measuring dissolution rate and monitoring the morphological evolution of glass surfaces using atomic force microscopy in order to solve the “evolving glass surface area” problem during corrosion.
- Use synchrotron-radiated XRR and XDS to preliminarily test the theory of interfacial dissolution and reprecipitation with the assistance of other surface characterization tools.

# CHAPTER I. AQUEOUS CORROSION OF NUCLEAR WASTE GLASSES: APPLICATION AND ADDITION OF SURFACE CHARACTERIZATION TOOLS

## 1. Introduction

A detailed understanding of the mechanistic and kinetic behavior of glass toward aqueous corrosion is of considerable importance for evaluating the nuclear safety of nuclear waste glass storage strategies [1], preserving objects of our cultural heritage [2], assessing the performance of glasses used in biomedical processes [3], consumer electronic, and industrial applications [4]. Glass is thermodynamically described as a metastable supercooled liquid with microscopically short range order and macroscopically long range disorder, where network formers (e.g. Si, Al, B) construct the order by forming connected polyhedrons, and modifier ions (e.g. Li, Na, K, Ca and Mg) retain the disorder by breaking the linkage (e.g. Si-O-Si bond) between polyhedra [5]. The composition of those glasses of interest varies from nuclear waste aluminoborosilicate glass containing more than 60 oxides (e.g. SON68 French nuclear waste reference glass) to ancient soda-lime-silicate glass (e.g. Egyptian, Greek, or Roman glasses) with only 3 oxides [1]. The composition of the glass plays an important role in determining the mechanistic and kinetic behavior of glass under aqueous attack, and attention has been particularly focused on the ratios between network formers and modifier ions by various researchers [6, 7, 8]. However, the mechanisms and kinetics as interchangeable factors affecting the general phenomena of glass corrosion are most important to evaluating nuclear safety as well as preserving ancient glassy artifacts [1, 7, 9].

Rapid growth in the semiconductor industry, microelectronics, and computer algorithms provides modern glass scientists, geologists, and mineralogists a set of non-destructive, nanometer-resoluted, and surface sensitive characterization tools to study the aqueous corrosion of glass in great detail. These tools include modern electron microscope in scanning (SEM) and transmission (TEM) mode, atomic force microscopy (AFM), energy/wavelength dispersive X-ray spectroscopy (EDS/WDS), X-ray photoelectron spectroscopy (XPS), secondary-ion mass spectrometry (SIMS), and recently developed techniques such as Nano-SIMS, helium ion microscopy, and atom probe tomography (APT). With the new addition of characterization tools such as APT, scientists were able to unveil the interfacial dissolution and reprecipitation mechanism of glass corrosion [1, 9, 10], which reportedly led to insights into the rate limiting factors of glass corrosion and thus provided better models toward evaluation of nuclear waste glass safety. Prior to the discovery of the interfacial dissolution and reprecipitation, the aqueous corrosion of glass was identified as an ion exchange reaction between hydrogen-bearing species of the aqueous medium and the alkali or the alkaline-earth ions in the glass, causing the formation of silanol groups, which led to the dissolution of glass into aqueous media [6, 7, 11]. Regardless of the debate between the ion exchange model and interfacial dissolution and reprecipitation model, the surface sensitive characterization tools are always the key to understanding glass corrosion.

In this study, the mechanism of glass corrosion as explored by various case studies using surface characterization tools was reviewed, and the advantages and limitations of the surface characterization techniques were evaluated. Overall, this chapter provides a state-of-the-art perspective/review on three main themes in glass

corrosion. i) What is the current state-of-the-knowledge on glass corrosion mechanisms? What will happen when the glass is exposed to aqueous media? ii) What is the "unknown" aspect in glass corrosion mechanisms? What characterization tools might help the investigation of the "unknowns"? iii) What conclusions have been drawn from studying glass corrosion using surface characterization tools? How might the limitations of each characterization technique affect the conclusions that have been reached? Given the complexity of atmospheric corrosion, the discussion here is limited to the aqueous media in liquid form. Also, special attention is given to the nuclear waste glass (aluminoborosilicate glass) due to the urgency in strategizing nuclear waste storage protocols [12].

## 2. What do we know about the interaction between "aqua" and glass?

Aqua, a Latin word, is defined as water, sea or rain; and the word aqueous is a derivative of the Latin word "aqua". In 1766, Cavendish made an extraordinary scientific discovery that a water molecule is composed of two hydrogens and one oxygen [13]. Hence, the aqueous corrosion of glass is the interaction between glass and hydrogen-bearing species. Understanding the physio-chemical phenomenon occurring on glass surface during aqueous corrosion requires a basic knowledge of glass structure at the atomistic scale, primarily the structure of silicate glasses. Greaves proposed the modified random network (MRN) model of silicate glass structure, which is characterized by percolation channels of network regions constructed by network formers and inter-network regions filled with modifier ions [14]. The non-bridging oxygen (NBO) bonds such as –Si–O–M and –Si–O–M–O–Si– is essentially an ionic bond. On the other hand, the bridging oxygen (BO) bonds are covalent bonds between network formers [5, 14]. It is quite clear that

the concentration of NBO and BO plays an important role in determining the glass durability since $H^+$ exchanges with $M^{n+}$ ($M^+$ for example in eq.1) and $OH^-$ breaks the –Si–O–Si– linkage (shown as eq.1 and eq.2, respectively) [15, 16, 17].

$$\equiv Si{-}O{-}M_{(glass)} + H^+_{(aq)} \rightarrow \equiv Si\text{-}O\text{-}M_{(glass)} + M^+_{(aq)} \quad (1)$$

$$\equiv Si{-}O{-}Si\equiv_{(glass)} + 2OH^-_{(aq)} \rightarrow 2\equiv Si\text{-}OH_{(glass)} \quad (2)$$

Apart from the basic chemistry knowledge of glass corrosion in an aqueous media, the current understanding of glass corrosion is based on the phenomenological discovery of glass corrosion kinetics and morphological change of glass. The studies of glass corrosion kinetics were often studied by the approach of measuring the concentration of released ions in leachate solution. Figure I.1 shows a typical plot of extracted Si concentration as a function of time, which features five distinguishable rate regimes as discussed in detail by Gin et. al. [11].

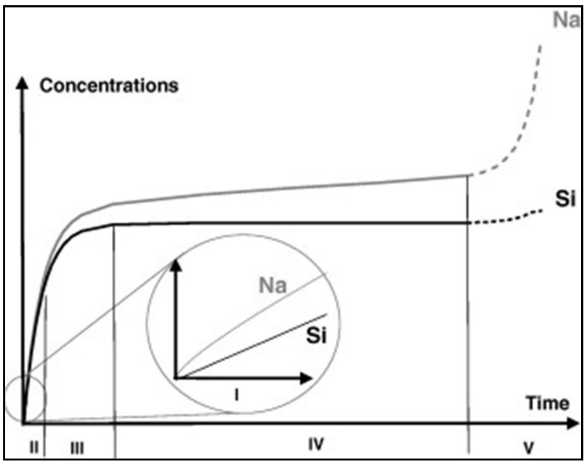


Figure I.1 Time sequence of different rate regimes and sodium and silicon concentrations in solution: I – initial diffusion, II – initial rate, III – rate drop, IV – residual rate, V – resumption of alteration in particular conditions. Courtesy of Gin et. al. [11].

The regime I, reported in the literature as interdiffusion regime, feature a diffusive process where protons in an aqueous media exchange with modifying ions in glass

network. Kinetically, the regime I exhibits a root-square time dependence of ion release [7, 11]. However, boron as a glass network former (not involved in the ion exchange process) was reported to have an identical release kinetics and concentration profile in corroded glass comparing to alkali or alkaline earth ions [18, 19, 20]. The regime II, initial rate or forward rate, refers to the hydrolysis of [$SiO_4$] tetrahedral into water-soluble orthosilicic acid, $H_4SiO_4$. The ion release in regime II is always congruent (stoichiometric to bulk glass composition), but was never found in most of the studied nuclear waste glass due to the existence of rigid bonds such as Si−O−Zr [11, 18]. The initial dissolution rate in regime II was experimentally found to be dependent on temperature, pH, and the glass composition [11, 21, 22]. In particular, an equation that describes such dependence has been reported in the pH of 6 to 10 and temperature range from 25 $^{o}$C to 100 $^{o}$C [11]. The regime III shows a rate drop, which is accompanied with the recondensation of orthosilicic acid to form an amorphous, hydrated "gel" (cross-linked, polymerized silica). The rate drop in regime III was accounted by two opposing theories, one based on the difference in chemical affinity between Si in solution and Si in bulk glass, and another one based on the passivating effect of the "gel" as a diffusion barrier [23, 24, 25, 26]. After the rate drop occurs, the rate of ion release becomes constant (regime IV). During this regime, the water diffuses through the gel and formation of secondary crystalline phase (e.g. zeolite) occurs [11]. Under some conditions (e.g. pH=11), the rate starts to increase, but was not often reported. With these five regimes of reaction, a morphological model of altered glass is conceptualized as shown in Figure I.2, and, furthermore, a model of estimating glass dissolution kinetics named as GRAAL (*Glass Reactivity with the Allowance for Alteration Layer*) model was developed [11].

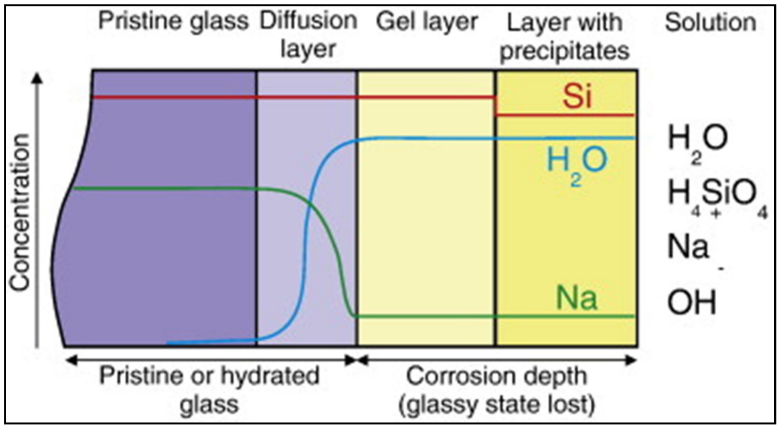


Figure I.2 Schematic drawing of the surface region of an altered glass. Courtesy of Geisler et. al. [9].

The most significant feature observed in the morphological model of altered glass, as a consequence of those five regimes of reaction, is the diffusion layer between the pristine glass and depleted "gel" layer. The diffusion layer features a "diffusion-type" of modifier ion concentration as a function of depth. Such concentration depth profile has been experimentally observed mostly using dynamic SIMS [27]. However, a new mechanism toward the description of glass alteration was reported by Geisler et. al. in 2010 [9]. This model opposes the ion exchange model with findings (based on TEM, SEM, and EDX) including: 1) no observable diffusion profile was found for oxygen and modifier ion isotopes; 2) highly porous and textured layers on the pristine glass surface with oscillation of chemical composition; 3) occurrence of silica spherules on the altered glass surface; 4) and, most importantly, a sharp phase boundary of the reaction rim towards the pristine glass [9]. The new model of glass corrosion, as firstly initiated by Geisler et. al. in 2010 [9], was later proven by a set of data from emerging new characterization techniques with the work of Hellmann et. al. in 2015 [1]. The evidence shows that there was no diffusion profile for modifier ions but a sharp chemical

composition difference between reaction rims and pristine glass [1]. Such evidence was collected using APT, Nano-SIMS, and new capabilities of TEM, which contributed to the conceptualization of the interfacial dissolution-reprecipitation model. A more detailed description of this interfacial dissolution-reprecipitation model was reported by Geisler et. al. in 2015 [10]. Figure I.3 shows a schematic presentation of such mechanism.

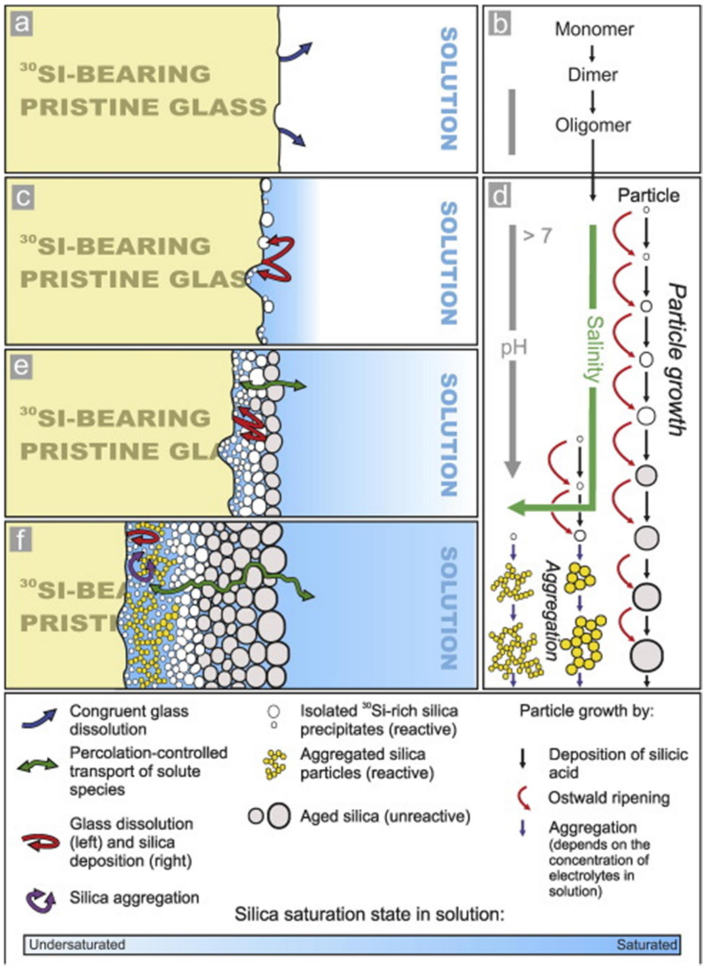


Figure I.3 Schematic outline of the proposed interface-coupled glass dissolution–silica reprecipitation process. Courtesy of Geisler et. al. [10].

The interfacial dissolution reprecipitation model basically describes a process that: congruent dissolution of the glass stops when the saturation of amorphous silica occurs at the glass surface (Figure I.3a), monomeric silica polymerizes in solution to

form dimers and oligomers (Figure I.3b), supersaturation occurs at the solution/glass interface and triggers the nucleation of silica at the hydroxylated glass surface sites (Figure I.3c), silica nuclei grows into spherules through Ostwald ripening to form a silica gel (Figure I.3d), and the decrease of bulk solution Si concentration due to formation of silica gel drives the interfacial solution away from the equilibrium (Figure I.3e) [10]. Thus, the chemically oscillating layers are formed by the supersaturation-precipitation-supersaturation cycle; and eventually, the transportation of molecular water and ions is limited (Figure I.3f).

This theory is quite plausible in explaining the phenomenological behavior occurring on the glass surface but greatly relies on a couple of assumptions. Two of the assumptions are 1) silica saturation occurs at the early stage of reaction (apart from the congruent dissolution regime), and the reprecipitation of silica occurs immediately after being dissolved from the glass; 2) the reaction rim of silica moves at a constant velocity towards the glass [1, 9, 10]. Questions are raised such as "How can one prove these assumptions are essentially true?", "Is there any way to test these assumptions with current characterization tools?", and "If one cannot directly observe the supersaturated solution-glass interface, can such phenomena be studied indirectly?". Certainly, assumptions mentioned above can be deliberately tested with carefully designed experiments, advanced characterization tools, and in-depth understanding of glass corrosion. Therefore, the most important goal of this chapter is to expand a discussion on the addition and application of surface characterization tools in recent years of glass corrosion studies that eventually will aid in unveiling the answer to these questions.

## 3. Probing the chemical and morphological information of altered glass with surface characterization tools

The foundation of the examination toward the mechanistic and kinetic behavior of glass in aqueous media is based on non-destructive analysis of laboratory or field degraded glass samples. The solution analysis of leachate ions combined with the characterization on glass objects correlates the kinetics (e.g. change of rate) to mechanisms (e.g. formation of "gel") [15]. Thus, a concise overview of applications, principles and limitations of surface characterization tools in glass corrosion studies is appropriate.

### 3.1 Electron beam based characterization techniques

The invention of the electron microscope helps scientists and engineers observe phenomenological features under an extremely high resolution [28]. The electron microscope (both scanning and transmission) has a significant impact on all aspects of science and engineering including studies of glass corrosion. The electron microscope with X-ray analyzer (EPMA, SEM/EDX, SEM/WDS and etc.) allows simultaneous imaging and compositional analysis on nano/micro-sized features of an altered glass. The principle of electron beam based characterization technique is the interaction between a highly focused beam (less than 10 nm, and the resolution depends on the material of emission filament) of electrons and a particular sample [28]. Subsequent detection of elastically (BSE, backscattered electron), inelastically scattered electrons (SE, secondary electron), and characteristic X-ray lines reveal the electron density contrast, topography, and compositional information of imaged domain, respectively [29]. Figure 4 serves as an excellent example of how the modern electron microscope is being used in analyzing corroded glass.

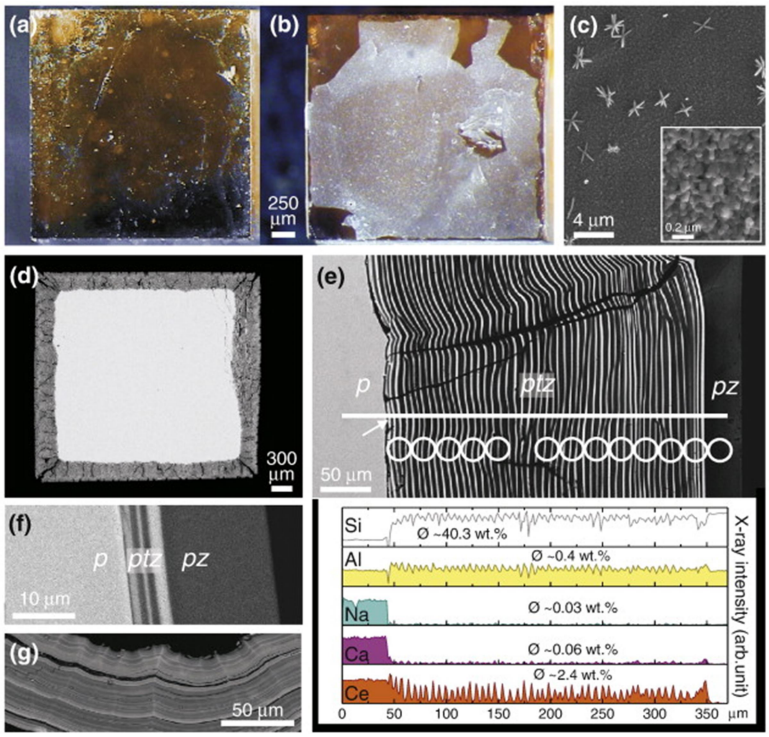


Figure I.4 Optical images of (a) an unreacted and (b) a reacted glass cuboid in aqueous solution. (c) SE image of reacted glass cuboid surface in (b). (d) BSE image of the cross section of the cuboid in (b), inset shows the Si spherules. (e) BSE image of the corrosion zone (pz: outer plane; ptz: oscillating patterned zone; p: pristine bulk glass) and its corresponding EDX line profile. (f) BSE image of another reacted glass cuboid. (g) BSE image of a 2500 year old, and naturally altered glass. Courtesy of Geisler et. al. [9].

The findings shown in Figure I.4 build the foundation of the interfacial dissolution and reprecipitation theory: SE image in Figure I.4c inset shows the Si spherules formed by Ostwald ripening, and Figure I.4e, f & g shows the textured "gel" layers formed by the localized supersaturation of Si in solution. In this work by Geilser [9], BSE signal was used to distinguish each patterned "gel" layer as well as pristine glass, SE signal was used to capture topographical features like the spherules, and characteristic X-ray lines allow the compositional investigation as a function of depth of altered glass. Commonly, the limitations of these techniques at least include: introduction of artifacts

during sample preparation (e.g. change of "gel" structure) [30]; low lateral resolution of characteristic X-ray lines (e.g. EDX line profile in Figure I.4e) [31]; charging of the sample sometimes need to be compensated by conductive carbon or noble metal coatings [32].

### 3.2 Depth profiles of altered glass using SIMS

The depth profile of altered glass surface interests the glass corrosion community given the correlation between kinetics and developed surface structure on the glass during aqueous corrosion. Commonly used techniques in materials science and geochemistry community are primarily XPS depth profile and dynamic SIMS. However, the inability of XPS to detect hydrogen and the low energy ion beam (< 5 kV) is the Achilles heel of XPS depth profile when it comes to using XPS in studying the surface structures on corroded glass [33]. Despite the great sensitivity and accuracy of quantitative chemical analysis (chemical environment and composition) of XPS [34], another Achilles heel of XPS depth profile is that the estimation of etching rate highly depends on the electron density of materials [35]. Thus, SIMS is more useful and appropriate to study the corroded glass.

The basic principle of SIMS is based on the detection of secondary ion, which is emitted by bombarding the sample surface with high energy (e.g. 25 keV) ion beam [36]. SIMS is capable of detecting all elements in the periodic table, and its static and dynamic mode allow elemental mapping, quantitative analysis of top material surface, and depth profiles [36]. A natural limitation of SIMS is that the sensitivity is often sacrificed at the cost of the lateral resolution [36]. Additionally, SIMS is a destructive surface characterization technique, which also limits its use when studying rare objects such as ancient glass artifacts. But, the advance in SIMS technique greatly helped the glass corrosion

community with its versatile capability in materials characterization. Figure I.5 shows depth profiles of a nuclear waste glass corroded for 209 days with heavy water and dyes.

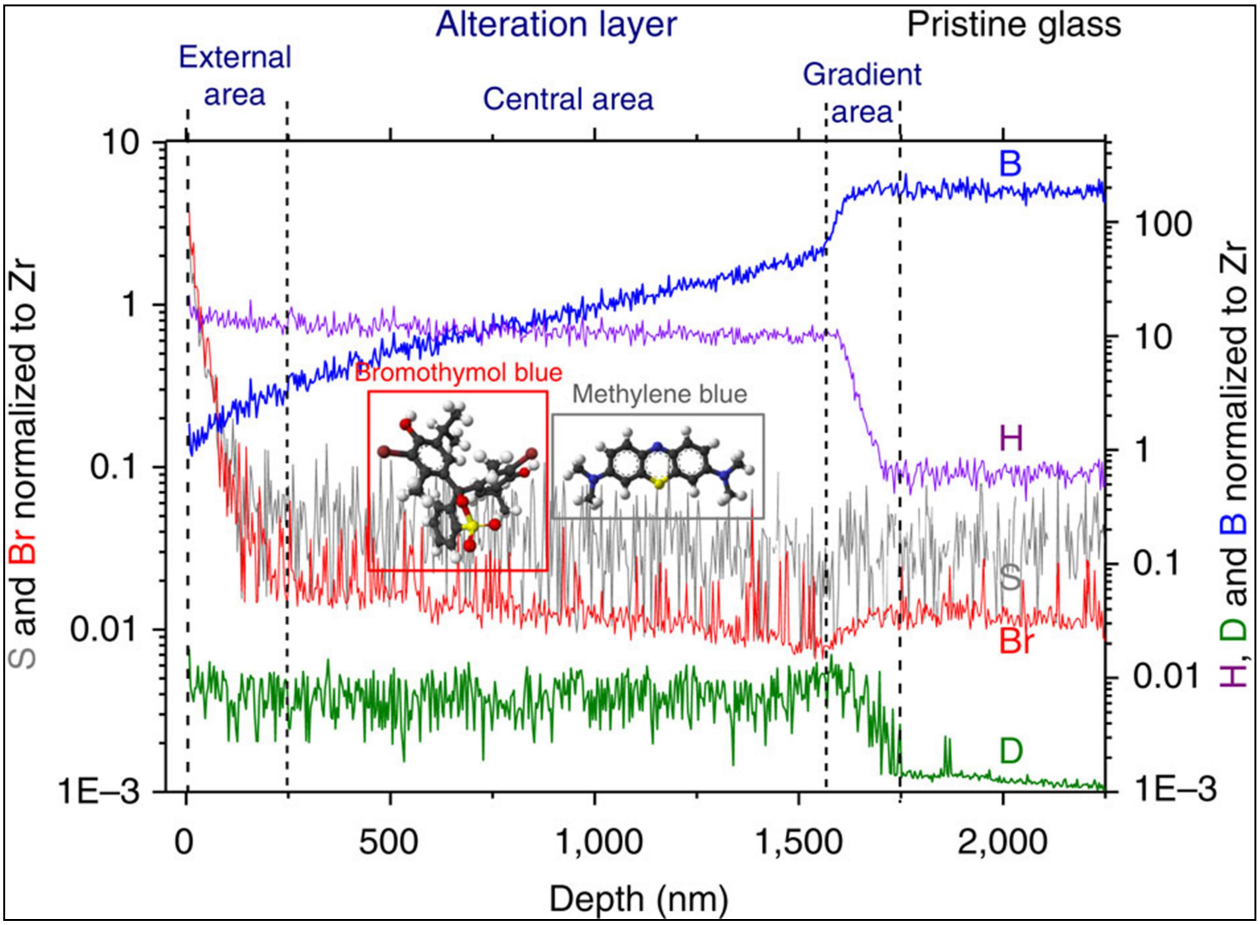


Figure I.5 Elemental profiles of international simple glass corroded in pH=7 solution for 209 days, with deuterium dioxide and dyes as tracers. Courtesy of Gin et. al. [27].

As shown in Figure I.5, the shape of the elemental profiles was used to assign the characteristic regions of each section of the line, e.g. the gradient shape line is assigned as the chemical gradient area. Also, the authors were able to theoretically determine the altered glass structure by correlating the penetration depth of the dye and the size of the dye molecule. Interestingly, the shape of elemental profile of B as a function of time presented in this study of Gin et. al. [27] was also used to determine the mechanism of glass corrosion. It is arguable whether the approach of using the shape of B depth profile to

model the reaction mechanism of glass aqueous corrosion is valid or not, but to some extent, it shows the confidence and advancement scientists have in contemporary SIMS. More often, SIMS was used to collect the depth profile of isotopes when studying the aqueous corrosion of nuclear waste glass as shown in Figure I.6.

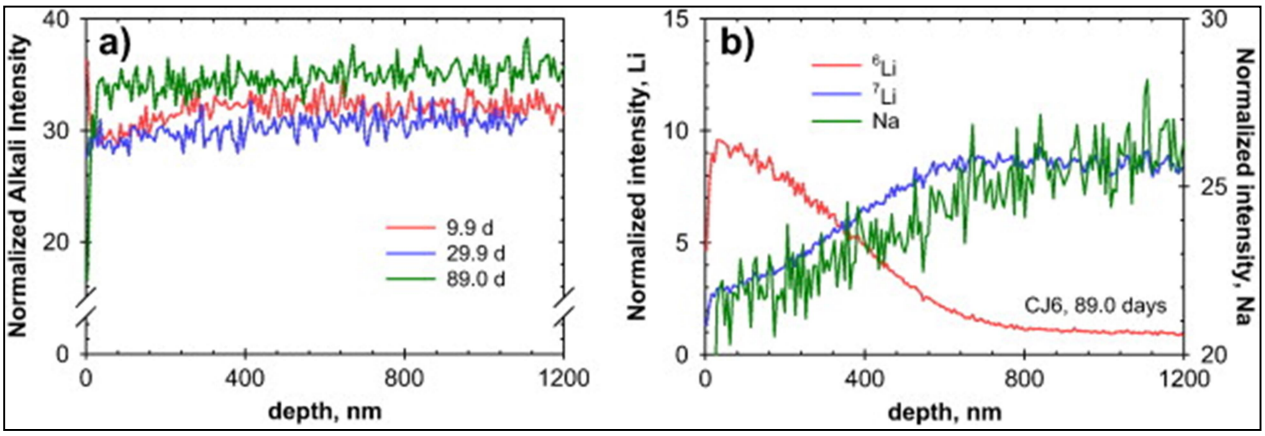


Figure I.6 a) The total alkali intensity normalized to Al across the sample depth for the CJ-6 (a simplified nuclear waste reference glass to SON68) samples and b) the profiles of $^{6}$Li, $^{7}$Li, and Na normalized to Al for the CJ-6 sample after 89.0 days of contact with $^{6}$Li solution. The intensities have been normalized to the $^{27}$Al intensity as a function of depth. Courtesy of Neeway et. al. [37].

Figure I.6a shows that the depletion of alkali element in bulk glass only occurs at the very top surface of altered glass regardless of reaction time, while the alkali content across the depth profile is almost constant. The depth profile presented in Figure 6b allows Neeway et. al. [37] to identify the altered glass thickness as well as understand the ion exchange between $^{6}$Li and $^{7}$Li as an inward-diffusion process. The ability of SIMS as a mass spectrometry method allows the glass corrosion community to design experiments using isotopes, and more importantly to interpret the glass corrosion behavior using imaging and depth profiles of isotopic elements.

Limitations also come with SIMS given its nature as a "destructive" characterization technique. The main limitations of SIMS include: 1) change in the

chemistry of sample due to destructive sputtering; 2) preferential sputtering due to the difference in ion yield of each element; 3) the "knock-on effect", which describe the ions being impinged onto the sample surface [36]. These limitations mentioned in this chapter are almost unavoidable but can be compensated by other depth profiling technique such as XPS [33, 36, 37].

### 3.3 Characterization of altered glass surface using XRR, AFM, and Interferometry

XRR is a non-destructive technique in characterizing the density, thickness, and interface roughness (also its lateral distribution) of multilayer materials. As discussed above in the context, glass develops an altered reaction rim (including secondary phases, the silica gel, and the de-alkalized glass) on top of the pristine glass when being corroded. The properties of the altered layer/layers helped to conceptualize the glass corrosion mechanism, and the density of those layers can only be accurately measured using XRR. In the study of Rebiscoul et. al [38], the authors derived the diffusion coefficient of water in glass by measuring the thickness of the hydrated glass. Additionally, the mechanism of the reaction was conceptualized via the measurement of properties of the developed "gel" layers as shown in Figure I.7.

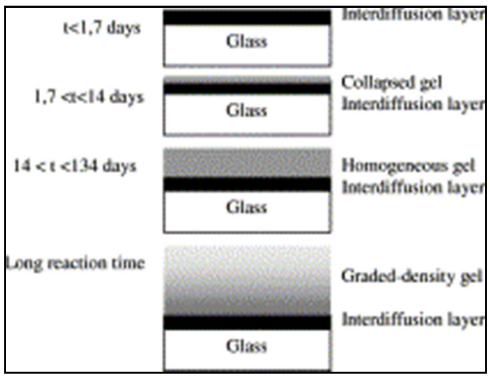


Figure I.7 The morphological evolution and corrosion mechanism of a French nuclear waste glass (SON68) summarized from XRR measurement. Courtesy of Rebiscoul et. al. [38].

Upon contact with aqueous solution, the glass starts to form an interdiffusion layer by ionic exchange, and further forms a homogeneous gel, and then forms a graded density "gel" layer. However, the effect of interface roughness on the measurement of the density of layers or identification of the number of layers, as greatly dependent on the constraints applied to the modeling of XRR curve, was not discussed [38]. Typical features observed on a XRR curve are critical angle, oscillation, and the drop in intensity, as shown in Figure I.8. The critical angle, the width of oscillation, and the drop of intensity after critical angle of a XRR curve determines the density, thickness, and roughness of layers, respectively [39]. A limitation of XRR is the requirement for the flatness of sample surface [39], which sometimes cannot be solved by polishing the samples that have already been corroded (e.g. ancient glass from a wreck ship). Another limitation of XRR is the inability to offer a depth of analysis deeper than 350 nm [38, 39]; also, the created scattering event due to roughness at the interface or top surface is a great concern for collecting or analyzing XRR curves. However, the relatively large probing area of XRR makes it an excellent technique for roughness measurement compare to AFM (scan size: tens of micrometers).

Since the invention of atomic force microscopy (AFM) in 1980s [40], AFM has been used for in-situ study of glass corrosion [41]. The principle of AFM is based on the scanning of a super sharp tip (couple of atoms, or even one single atom) across the sample surface and recording the displacement of piezoelectric component as a function of its scanning location [40]. The displacement of piezoelectric being recorded can be used to generate topography [40], phase map (tribological properties) [42], and even mechanical properties depending on the setup of the instrument [43]. It was argued that AFM only

yields topography of measured sample, and most of the glass corrosion studies associated with AFM were focused on the interpretation of the developed surface features after corrosion. One problematic issue of AFM is that the artifacts/misinterpretations associated with interpreting surface features can hardly be evaluated given the rigid requirement of sample cleanliness and vibration (both mechanical and magnetic) free environment. However, Mellott and Pantano [44] linked the evolution of glass surface roughness to a function of solution pH. In their study, glass melt surface and glass fiber surface were reacted at different solution pHs. With the use of smooth and homogenous melt surface, the authors were able to study the evolution of RMS instead of the evolution of polishing grooves if polished glass surfaces were used. Figure 8, as presented in the study of Mellott and Pantano [44], shows the atomic force micrographs of unreacted and reacted glass fiber surfaces.

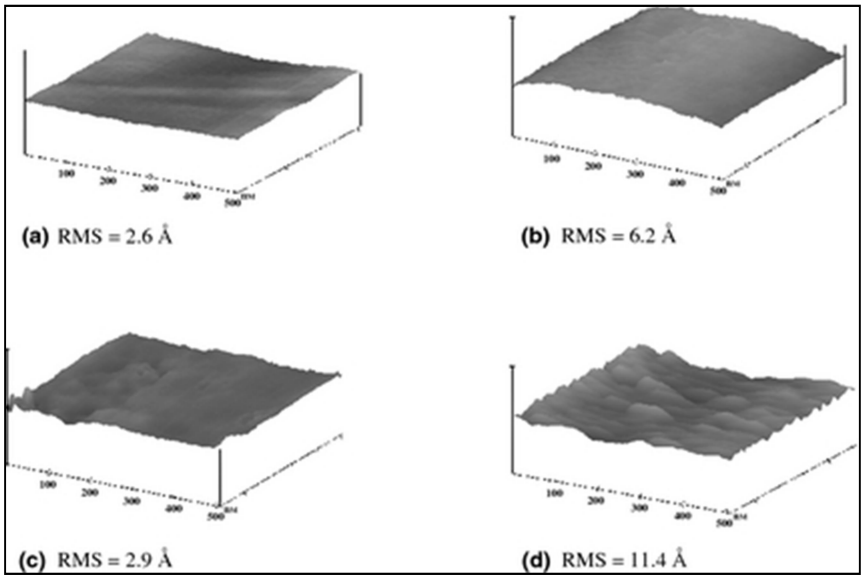

Figure I.8 Atomic force microscopy images and corresponding RMS values of CAS1 (a calcium aluminosilicate glass) fiber surfaces; (a) unreacted, (b) reacted pH 1 100 h, (c) reacted pH 6.4 100 h, and (d) reacted pH 9 100 h. All images are 500 nm × 500 nm with z-range = 10 nm. Courtesy of Mellott and Pantano [44].

It was found that the glass fiber surface roughens at a different level given the same time of reaction, and the roughening level shows a trend that $RMS_{basic} > RMS_{acid} > RMS_{neutral}$. Also, for the very first time, the authors concluded from the XPS result that the mechanism responsible for roughening in basic and acid solution is network dissolution and leaching of modifier ions, respectively. Such interesting relationship between roughening behavior and glass corrosion mechanism led to a question: is the roughening behavior (roughening rate and distribution of roughness in reciprocal space) a reflection of glass structure? The answer appears to be "yes", but it needs to be pointed out that collecting artifact-free AFM images is a time-consuming process. This factor, along with other experimental variables, makes it an extremely hard project to study the relationship between glass surface roughening and structure.

Interferometry, specifically white light interferometry or alternatively named as coherence scanning interferometry, separates a beam of light into two beams and recombines the split beams to create an interference pattern. The interference pattern can be used to analyze the path that the beam travels, and therefore create the surface topography [45]. The white light interferometry has a significant higher vertical limit (up to couple of millimeters) compared to AFM (less than 10 μm); however, both the vertical (~ 3 nm) and lateral resolution (tens of nanometers) are lower than that of AFM (horizontal resolution: less than 10 nm; vertical resolution: ~ 0.1 nm) [46]. The phase scanning interferometry is not discussed here, given its limited applications in metrological studies of smooth samples (RMS less than 30 nm) [47]. Given the limitations of white light

interferometry, this technique is often used to examine the glass surface finishing techniques and is rarely reported to be used in studies of glass corrosion with the exception of Icenhower's work [48]. Icenhower and Steefel [48] used interferometry to measure the surface retreat between a masked and a reacted glass surface, and then used the surface retreat to deduce the dissolution rate of nuclear waste glass. Figure I.9 shows the surface retreat measured by white light interferometry in Icenhower's work.

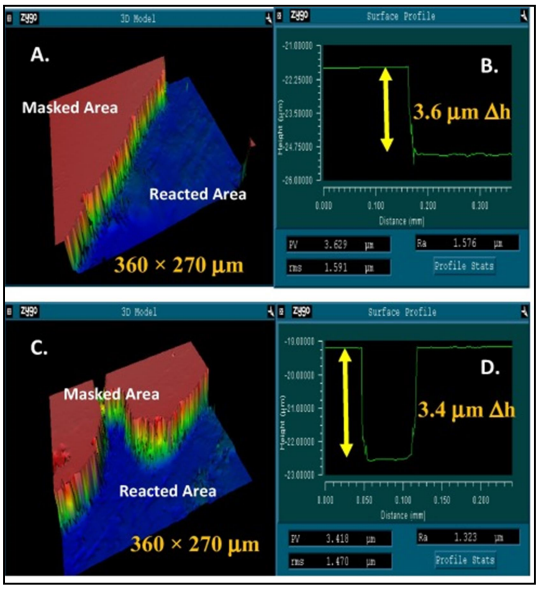


Figure I.9 Three-dimensional interferometer images (A and C) and corresponding height profiles (B and D) of two 360 × 270 µm areas on a glass monolith surface. Courtesy of Icenhower and Steefel [48].

As shown in Figure I.9, the authors were able to quantify the surface retreat by measuring the line profiles (Figure I.9B and D). The surface retreat (nm or µm) was then translated into dissolution rate ($g/m^2d$) in order to compare the rate to conventional dissolution rates obtained from solution analysis. It was found in this study that the dissolution rate obtained from interferometry is comparable to the dissolution rates obtained in field studies (e.g. naturally corroded glass) [48]. One goal underlying this interferometric method of measuring dissolution rate is to eliminate the evolving surface

area during corrosion since the glass surface area is used to normalize the dissolution rate [48]. However, this method of measuring dissolution rate is limited when the glass surface develops "gel" structures (e.g. Icenhower and Steefel exfoliated the "gel" from the surface to measure the surface retreat), and the depth of reaction below the "gel" is hard to quantify without the use of other imaging characterization techniques [48]. The techniques applied to characterize the glass surfaces, in summary, allow one to directly build a relationship between glass dissolution rate, morphological evolution, mechanism of corrosion and even glass structure. However, a general consensus of how each perspective of glass corrosion is associated with one another has not been clear yet.

## 4. What additions of advanced surface characterization tools advanced our understanding of glass corrosion?

During the past six decades, the knowledge in glass corrosion was constantly reiterated with emerging characterization techniques and experimental methods [1, 7, 11, 12]. However, the relationship between the kinetics of glass corrosion, mechanism of glass corrosion and glass structure is still not well understood [49]. The kinetics, mechanism, and glass structure can be reflected by the density of altered layers, structure, thickness of altered layers, and the roughness of glass-water reaction front, respectively. Thus, one goal of this section is to cover and briefly discuss the emerging techniques in glass corrosion community, particularly on the probing of altered layer density and interface between the altered layer and pristine bulk glass.

As discussed previously, the density of the "gel" layer on corroded glass surface determines the transportation of ions or clusters in aqueous solution, and thus partly decides the rate of dissolution. However, the measurement of density using XRR requires

the flatness of sample and introduces misinterpretations when the curve is not properly modeled with constraints. More importantly, the depth of analysis of XRR made itself impractical when testing a corroded glass with micron-thick "gel". Recently, Trivelpiece et. al. [50] reported a new method of measuring the density of altered glass layers using neutron depth profiling with the combination of SEM. Neutron depth profiling determines the energy loss of isotopic elements versus the location of elements via neutron-induced positive Q-value nuclear reactions. Figure I.10 is a neutron depth profile of a lithium di-silicate glass corroded in pH4 hydrochloric acid for 17.5 hours.

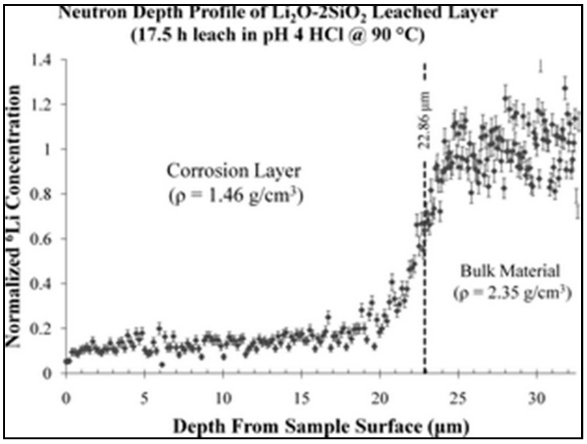


Figure I.10 NDP profile of 17.5 h leach specimen. Courtesy of Trivelpiece et. al [50].

As shown in Figure I.10, the neutron depth profiling technique was able to detect the corrosion layer thicker than 20 μm while obtaining the density of the corrosion layer. The idea behind this method was to use the detected neutron stopping power to calculate the density of altered glass layer at a given surface area (sample was prepared by focused ion beam) [50]. The use of neutron depth profiling enables the density profiling across the "gel" layers on top of the glass surface, and further helps to determine the transportation behavior between the glass and an aqueous medium. However, the application of neutron depth profiling in complex glass systems (e.g. SON68) has yet to be investigated.

The most important goal of using depth profiling technique is to use the shape of certain element profiles across the altered layer to lend insight on the mechanism of glass corrosion. The gradient element profile acquired by SIMS, as shown in Figure I.5 and I.6b, suggests to the glass corrosion community that the observed chemical gradient is caused by the inward diffusion of the water molecule and outward diffusion of elements within the glass. Based on the observations of such chemical gradients across the altered layer, kinetic models of glass corrosion such as the GRAAL model have been used to estimate the long-term alteration behavior of glasses [11]. The chemical gradient in ionic-exchange coupled hydration mechanism has been overturned with evidence from the emerging of new characterization techniques, such as atom probe tomography (APT). Figure I.11 is atom probe tomographs of a nuclear waste glass reacted in the granitic environment.

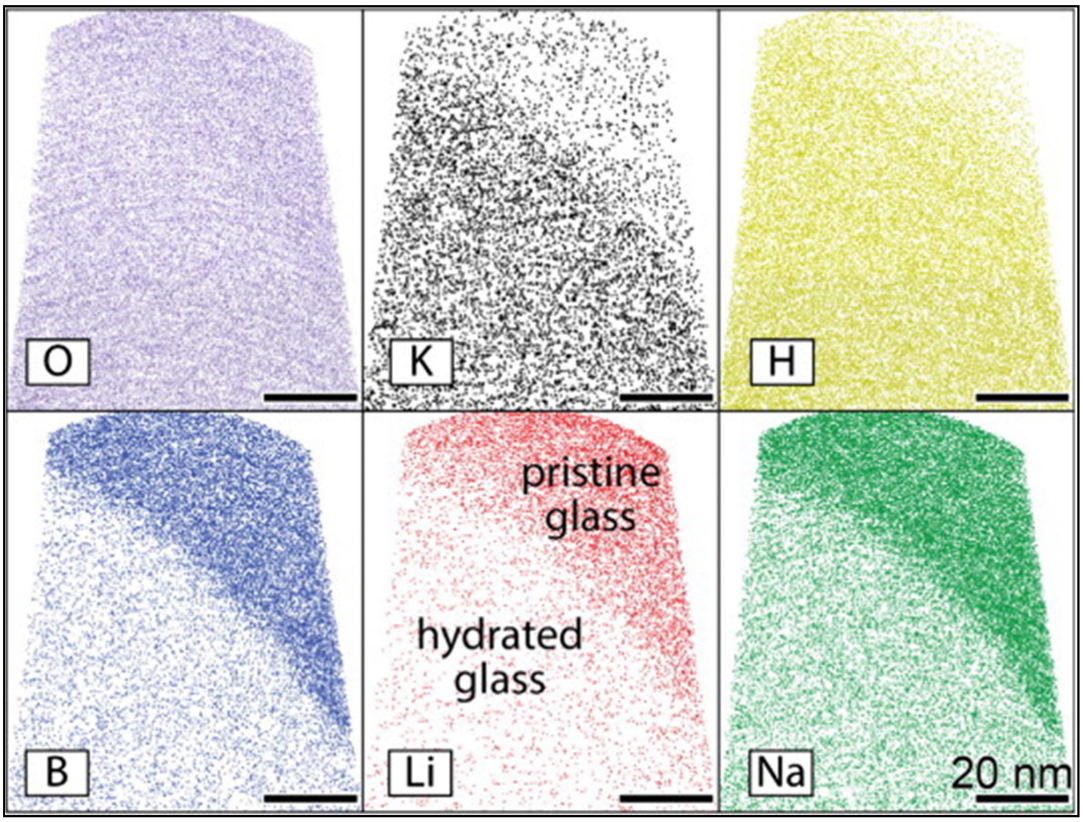

Figure I.11 Element-specific atom maps from a subsection of an APT reconstruction of the hydrated glass/pristine glass interface in SON68. Courtesy of Gin et. al. [51].

As shown in Figure I.11, a super sharp chemical interface (~ 3 nm) was found for boron. The existence of such sharp interface for B contradicts the diffusion control of corrosion process, and the interface observed was concluded to be a dissolution front. Gin et. al. [51] also compared the width of the interface acquired by different techniques: APT is ~ 3 nm, EFTEM is ~ 30 nm, and NanoSIMS (a coaxial design of the ion gun and the secondary ion extract to increase the spatial resolution of static SIMS) is ~ 170 nm. A more recent study of Hellmann et. al. [1] with APT validated the existence of a sharpened interface between pristine glass and altered layers. This recent finding supported the interfacial dissolution and reprecipitation model proposed by Geisler et. al. in 2010 [9]. Figure I.12 is the APT map and elemental profiles of SON68 glass corroded in acid for one month.

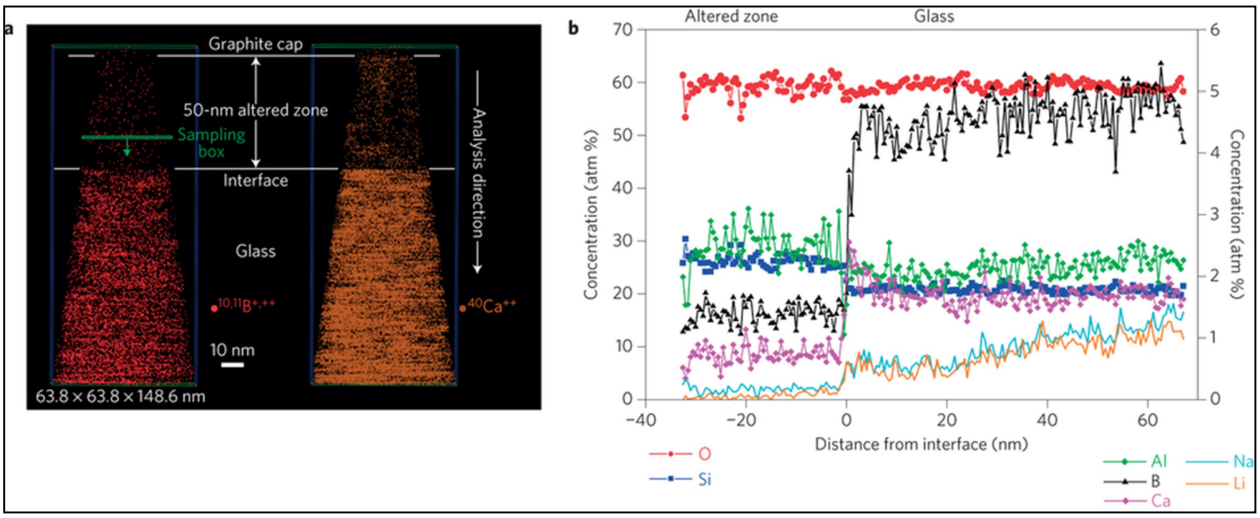


Figure I.12 a)Three-dimensional chemical maps for B and Ca b) Chemical profiles derived from three-dimensional chemical maps, extending from the altered zone to the pristine glass (note two different ordinate scales, depending on element). Courtesy of Hellmann et. al. [1].

A single dot in Figure I.12a represents a single atom. It was found that the altered layer was strongly depleted in B and Ca, and the chemical interfaces separating the pristine glass and altered layer was atomically sharp. Hellmann et. al. [9] also deconvoluted the three-dimensional maps into depth profiles as shown in Figure I.12b. As shown in Figure I.12b, the altered layer/pristine glass interface was characterized by sharp increases in Si, Al and O concentrations and sharp drops in B, Ca, Na and Li concentrations. The monotonical increase of Na and Li concentration at the interface was experimentally determined to be an artifact during laser pulsing. This sharpened interface as observed in different studies using APT helped to conceptualize the underlying mechanism. More importantly, findings from new characterization techniques advanced the understanding and estimation of glass corrosion behavior. It is the advancement in the semiconductor industries, photonics, fundamental physics and chemistry that brought new characterization techniques with more flexible capabilities, faster data collection, and finer resolution. Eventually, the upcoming new characterization technique will help to understand glass corrosion, strategize nuclear waste storage, and eventually provide safer nuclear energy.

**Conclusion**

Investigating the relationship between glass corrosion kinetics/mechanism, glass structure, and morphological evolution of glass surfaces contributes to the estimation of glass dissolution rates in the long term. Surface characterization tools were able to provide scientists with different information with respect to the chemical composition of altered layers and pristine glass, the morphology of interfaces between the altered layer and pristine glass, and even density that controls the transportation of water molecules

and elements from the bulk glass. These phenomenological observations on altered glass identified the corresponding mechanism of glass corrosion and the responsible change of kinetics, and even contributed to the modeling of glass corrosion kinetics (e.g. GRAAL model). More recently, scientists were able to establish a new model so-called interfacial dissolution and reprecipitation model toward glass corrosion, with atomic resolution APT techniques. However, gaps remained unfilled in answering the key question such as "what is the relationship between glass roughening behavior under aqueous corrosion and the glass structure? Or at least, can the roughening behavior of glass reflects its structure?"

**References**


1. R. Hellmann, S. Cotte, E. Cadel, S. Malladi, L. S. Karlsson, S. Lozano-Perez, M. Cabié, and A. Seyeux, "Nanometre-scale evidence for interfacial dissolution–reprecipitation control of silicate glass corrosion," *Nat Mater,* 14[3] 307-11 (2015).
2. M. Melcher, R. Wiesinger, and M. Schreiner, "Degradation of glass artifacts: application of modern surface analytical techniques," *Accounts of Chemical Research,* 43[6] 916-26 (2010).
3. A. Clark, C. Pantano, and L. Hench, "Auger spectroscopic analysis of bioglass corrosion films," *Journal of the American Ceramic Society,* 59[1-2] 37-39 (1976).
4. N. Mellott, C. Durucan, C. Pantano, and M. Guglielmi, "Commercial and laboratory prepared titanium dioxide thin films for self-cleaning glasses: photocatalytic performance and chemical durability," *Thin Solid Films,* 502[1] 112-20 (2006).

5. G. Greaves, "EXAFS and the structure of glass," *Journal of Non-Crystalline Solids,* 71[1] 203-17 (1985).

6. D. Sanders and L. Hench, "Mechanisms of glass corrosion," *Journal of the American Ceramic Society,* 56[7] 373-77 (1973).

7. C. Cailleteau, F. Angeli, F. Devreux, S. Gin, J. Jestin, P. Jollivet, and O. Spalla, "Insight into silicate-glass corrosion mechanisms," *Nature Materials,* 7[12] 978-83 (2008).

8. D. M. Strachan and T. L. Croak, "Compositional effects on long-term dissolution of borosilicate glass," *Journal of Non-crystalline Solids,* 272[1] 22-33 (2000).

9. T. Geisler, A. Janssen, D. Scheiter, T. Stephan, J. Berndt, and A. Putnis, "Aqueous corrosion of borosilicate glass under acidic conditions: a new corrosion mechanism," *Journal of Non-Crystalline Solids,* 356[28] 1458-65 (2010).

10. T. Geisler, T. Nagel, M. R. Kilburn, A. Janssen, J. P. Icenhower, R. O. Fonseca, M. Grange, and A. A. Nemchin, "The mechanism of borosilicate glass corrosion revisited," *Geochimica et Cosmochimica Acta,* 158 112-29 (2015).

11. P. Frugier, S. Gin, Y. Minet, T. Chave, B. Bonin, N. Godon, J.-E. Lartigue, P. Jollivet, A. Ayral, and L. De Windt, "SON68 nuclear glass dissolution kinetics: Current state of knowledge and basis of the new GRAAL model," *Journal of Nuclear Materials,* 380[1] 8-21 (2008).

12. S. Gin, A. Abdelouas, L. J. Criscenti, W. L. Ebert, K. Ferrand, T. Geisler, M. T. Harrison, Y. Inagaki, S. Mitsui, and K. T. Mueller, "An international initiative on long-term behavior of high-level nuclear waste glass," *Materials Today,* 16[6] 243-48 (2013).

13. H. Cavendish, "Three papers, containing experiments on factitious air, by the Hon. Henry Cavendish, FRS," *Philosophical Transactions of the Royal Society,* 56 141-84 (1766).

14. G. N. Greaves, "EXAFS and the structure of glass" *Journal of Non-Crystalline Solids,* 71[1] 203-217 (1985).

15. D. E. Clark, C. G. Pantano Jr, and L. L. Hench, "Corrosion of glass," Books for Industry and the Glass Industry, Division of Magazines for Industry Inc. , New York, NY (1979).

16. M. A. Rana and R. Douglas, "The reaction between glass and water. Part 1. Experimental methods and observations," *Phys. Chem. Glasses,* 2[6] 179-95 (1961).

17. M. Rana and R. Douglas, "The reaction between glass and water. Part 2. Discussion of the results," *Phys. Chem. Glasses,* 2[6] 196-204 (1961).

18. S. Gin, X. Beaudoux, F. Angéli, C. Jégou, and N. Godon, "Effect of composition on the short-term and long-term dissolution rates of ten borosilicate glasses of increasing complexity from 3 to 30 oxides," *Journal of Non-Crystalline Solids,* 358[18] 2559-70 (2012).

19. G. Geneste, F. Bouyer, and S. Gin, "Hydrogen–sodium interdiffusion in borosilicate glasses investigated from first principles," *Journal of Non-Crystalline Solids,* 352[28] 3147-52 (2006).

20. J. P. Icenhower, B. P. McGrail, W. J. Shaw, E. M. Pierce, P. Nachimuthu, D. K. Shuh, E. A. Rodriguez, and J. L. Steele, "Experimentally determined dissolution kinetics of Na-rich borosilicate glass at far from equilibrium conditions:

implications for transition state theory," *Geochimica et Cosmochimica Acta,* 72[12] 2767-88 (2008).

21. T. Advocat, J. Crovisier, E. Vernaz, G. Ehret, and H. Charpentier, "Hydrolysis of R7T7 nuclear waste glass in dilute media: mechanisms and rate as a function of pH,″ pp. 57 in MRS Proceedings. Vol. 212.
22. E. H. Oelkers, "General kinetic description of multioxide silicate mineral and glass dissolution," *Geochimica et Cosmochimica Acta,* 65[21] 3703-19 (2001).
23. É. Y. Vernaz, "Estimating the lifetime of R7T7 glass in various media," *Comptes Rendus Physique,* 3[7] 813-25 (2002).
24. P. Aagaard and H. C. Helgeson, "Thermodynamic and kinetic constraints on reaction rates among minerals and aqueous solutions; I, Theoretical considerations," *American Journal of Science,* 282[3] 237-85 (1982).
25. H. C. Helgeson, W. M. Murphy, and P. Aagaard, "Thermodynamic and kinetic constraints on reaction rates among minerals and aqueous solutions. II. Rate constants, effective surface area, and the hydrolysis of feldspar," *Geochimica et Cosmochimica Acta,* 48[12] 2405-32 (1984).
26. W. M. Murphy and H. C. Helgeson, "Thermodynamic and kinetic constraints on reaction rates among minerals and aqueous solutions. III. Activated complexes and the pH-dependence of the rates of feldspar, pyroxene, wollastonite, and olivine hydrolysis," *Geochimica et Cosmochimica Acta,* 51[12] 3137-53 (1987).
27. S. Gin, P. Jollivet, M. Fournier, F. Angeli, P. Frugier, and T. Charpentier, "Origin and consequences of silicate glass passivation by surface layers," *Nature Communications,* 6 (2015).

28. E. Ruska, "The development of the electron microscope and of electron microscopy," *Reviews of Modern Physics,* 59[3] 627 (1987).

29. S. J. B. Reed and S. J. B. Reed, "Electron microprobe analysis," Vol. 2. Cambridge University Press Cambridge, (1975).

30. L. Muller and T. Jacks, "Rapid chemical dehydration of samples for electron microscopic examinations," *Journal of Histochemistry & Cytochemistry,* 23[2] 107-10 (1975).

31. D. Wollman, K. D. Irwin, G. C. Hilton, L. Dulcie, D. E. NEWBURY, and J. M. MARTINIS, "High-resolution, energy-dispersive microcalorimeter spectrometer for X-ray microanalysis," *Journal of Microscopy,* 188[3] 196-223 (1997).

32. J. Goldstein, D. E. Newbury, P. Echlin, D. C. Joy, A. D. Romig Jr, C. E. Lyman, C. Fiori, and E. Lifshin, "Scanning electron microscopy and X-ray microanalysis: a text for biologists, materials scientists, and geologists." Plenum Press, New York, NY, (2012).

33. S. Hofmann, "Sputter depth profile analysis of interfaces," *Reports on Progress in Physics,* 61[7] 827 (1998).

34. C. Fadley, R. Baird, W. Siekhaus, T. Novakov, and S. Bergström, "Surface analysis and angular distributions in x-ray photoelectron spectroscopy," *Journal of Electron Spectroscopy and Related Phenomena,* 4[2] 93-137 (1974).

35. C. Fadley, "Basic concepts of X-ray photoelectron spectroscopy," *Electron Spectroscopy: Theory, Techniques and Applications,* 2 1-156 (1978).

36. R. G. Wilson, F. A. Stevie, and C. W. Magee, "Secondary ion mass spectrometry: a practical handbook for depth profiling and bulk impurity analysis." Wiley-Interscience, New York, NY, (1989).

37. J. J. Neeway, S. Kerisit, S. Gin, Z. Wang, Z. Zhu, and J. V. Ryan, "Low-temperature lithium diffusion in simulated high-level boroaluminosilicate nuclear waste glasses," *Journal of Non-Crystalline Solids,* 405 83-90 (2014).

38. D. Rebiscoul, A. Van Der Lee, P. Frugier, A. Ayral, and S. Gin, "X-ray reflectometry characterization of SON 68 glass alteration films," *Journal of Non-Crystalline Solids,* 325[1] 113-23 (2003).

39. J. Daillant and A. Gibaud, "X-ray and neutron reflectivity: principles and applications" Vol. 770. Springer, Berlin, Heidelberg, (2008).

40. G. Binnig, C. F. Quate, and C. Gerber, "Atomic force microscope," *Physical Review Letters,* 56[9] 930 (1986).

41. I. Schmitz, M. Schreiner, G. Friedbacher, and M. Grasserbauer, "Tapping-mode AFM in comparison to contact-mode AFM as a tool for in situ investigations of surface reactions with reference to glass corrosion," *Analytical Chemistry,* 69[6] 1012-18 (1997).

42. I. Schmitz, M. Schreiner, G. Friedbacher, and M. Grasserbauer, "Phase imaging as an extension to tapping mode AFM for the identification of material properties on humidity-sensitive surfaces," *Applied Surface Science,* 115[2] 190-98 (1997).

43. B. Briscoe, L. Fiori, and E. Pelillo, "Nano-indentation of polymeric surfaces," *Journal of Physics D: Applied Physics,* 31[19] 2395 (1998).

44. N. P. Mellott and C. G. Pantano, "A Mechanism of Corrosion-Induced Roughening of Glass Surfaces," *International Journal of Applied Glass Science,* 4[3] 274-79 (2013).

45. J. C. Wyant, "White light interferometry.″ pp. 98-107 in AeroSense 2002, International Society for Optics and Photonics, 2002.

46. F. Gao, R. K. Leach, J. Petzing, and J. M. Coupland, "Surface measurement errors using commercial scanning white light interferometers," *Measurement Science and Technology,* 19[1] 015303 (2007).

47. K. Creath, "V phase-measurement interferometry techniques," *Progress in Optics,* 26 349-93 (1988).

48. J. P. Icenhower and C. I. Steefel, "Experimentally determined dissolution kinetics of SON68 glass at 90 C over a silica saturation interval: Evidence against a linear rate law," *Journal of Nuclear Materials,* 439[1] 137-47 (2013).

49. J. D. Vienna, J. V. Ryan, S. Gin, and Y. Inagaki, "Current Understanding and Remaining Challenges in Modeling Long-Term Degradation of Borosilicate Nuclear Waste Glasses," *International Journal of Applied Glass Science,* 4[4] 283-94 (2013).

50. C. L. Trivelpiece, J. J. Petrunis, C. G. Pantano, and R. G. Downing, "Glass Surface Layer Density by Neutron Depth Profiling," *International Journal of Applied Glass Science,* 3[2] 137-43 (2012).

51. S. Gin, J. V. Ryan, D. K. Schreiber, J. Neeway, and M. Cabié, "Contribution of atom-probe tomography to a better understanding of glass alteration mechanisms:

Application to a nuclear glass specimen altered 25years in a granitic environment," *Chemical Geology,* 349 99-109 (2013).

# CHAPTER II. QUANTITATIVE MORPHOLOGICAL AND COMPOSITIONAL EVALUATION OF LABORATORY PREPARED ALUMINOBOROSILICATE GLASS SURFACES

## 1. Introduction

The surface quality has great impact on the performance properties of many novel and emerging technological applications for glasses including those for displays, biomedical applications, microelectronics and advanced optical lithography systems [1, 2]. In some cases, the glass surface morphology and overall roughness has become the threshold for the continued development of novel electronics and portable devices [3, 4]. The surface morphology, chemical composition and homogeneity of glass manufacturing products can influence a wide variety of performance related properties including the mechanical strength and chemical durability [5, 6, 7, 8]. Furthermore, smooth, homogeneous and compositionally reproducible glass surfaces are required for mechanistic investigations associated with glass corrosion, chemical tempering, and thin film coating on glasses [9]. For example, studies on the dissolution behavior of silicate glasses suggested surface morphology and composition can greatly affect the dissolution or alteration rate of these glasses [10, 11, 12].

A variety of processing methods can be utilized to engineer glass surfaces, including mechanical force, chemical and mechanical polishing, and thermal treatment [9, 13, 14]. Each will affect the glass morphology and composition. For example, the annealing of some glass compositions can deplete or enrich the surface in metallic ions due to evaporation and segregation [5]. In the case of chemo-mechanical polishing, chemical

reactions between the glass surface and the polishing media polishing can alter the surface composition relative to the bulk glass composition [15, 16, 17, 18, 19]. These changes in surface morphology and chemistry have been shown to effect mechanical, chemical, and aesthetic properties [5, 6, 7, 8]. There are a variety of characterization tools available for the surface compositional and morphological analysis of glass surfaces, each with their own capabilities and limitations. Of particular interest here is X-ray photoelectron spectroscopy (XPS) for quantification of chemical composition and chemical environment and atomic force microscopy (AFM) for surface topographic imaging and quantitative morphological analysis.

XPS is routinely used to determine both the chemical composition and local chemical environment of elements associated with glass surfaces [19, 20, 21]. In particular, under standard operating conditions, as those used in this work, the XPS probes to a depth of approximately 5 to 10 nm and therefore is a useful probe of the uppermost surface composition and chemistry. Through the empirical derivation of relative sensitivity factors and high resolution peak area analysis, absolute quantification of the glass surface composition is achievable [22]. Furthermore, through analysis of peak position and shape the chemical environment of the glass forming elements can also be analyzed [23, 24].

AFM is one of the more common techniques in the qualitative and quantitative analysis of glass surface morphology, given its flexibility, relatively low cost, high lateral resolution, and high sensitivity to topographic features on the angstrom to micron scale [25, 26]. Quantitative roughness analysis measured by AFM is often represented by simple statistical parameters, such as average roughness, apparent root-mean-squared roughness

(RMS), or peak-to-valley roughness. In these cases, 250,000 data points (512 X 512 pixels per image, for example) are expressed by a single number. However, apparent RMS values are problematic since two drastically different topographies can have the same RMS value [24, 26, 27, 28]. This is due to the fact that apparent RMS values are only sensitive to z-axis (vertical) height deviation, not x, y-axis (horizontal) structures. Therefore, such measurements are greatly dependent on the homogeneity of the surface scanned and can be quite problematic, in some cases leading to the difficulty in understanding surface roughness and its spatial distribution homogeneity.

Rather than using the simple above-mentioned statistical parameters, surfaces can also be represented by power spectral density (PSD) functions over different spatial frequency regions. PSD is advantageous as it allows the comparison of roughness data measured at different spatial frequencies, offering a convenient representation of the spatial distribution and homogeneity of roughness [25]. This is realized through a 2D fast Fourier transformation algorithm allowing correlation of the z-axis height deviation with the x-, y-axis location data in real and reciprocal space. Furthermore, from the PSD profiles a series of spatially sensitive quantitative roughness parameters can be derived including the fractal dimension, Hurst exponent, correlation length, and equivalent RMS roughness [26].

In this chapter, a systematic method to prepare smooth glass melt and polished surfaces with surface compositions similar to that of the bulk is provided. Glass surface composition and morphology were quantified using complementary surface sensitive characterization tools, including XPS and AFM. In particular, both vertical and spatial distribution of roughness was investigated using advanced PSD analysis, and for the first

time, we report spatially sensitive roughness parameters of a variety of glass surfaces, as a function of processing.

## 2. Materials and Methods

### 2.1 Glass Melting and Bulk Glass Composition Analysis

The aluminoborosilicate glass used in this study, referred to as the international simple glass (ISG), is a reference waste glass composition developed and utilized by a 6-nation collaborative effort in examining nuclear waste glass corrosion [28]. The ISG glass used in this study was commercially melted by Mo-Sci Corporation, with melting procedures documented in detail elsewhere and briefly described here [29]. The ISG glasses were batched to yield a nominal weight% composition of 56.2 % $SiO_2$, 17.3 % $B_2O_3$, 12.2 % $Na_2O$, 6.1 $Al_2O_3$, 5.0 % CaO and 2.8 % $ZrO_2$. Initial batch melting was performed in a platinum-rhodium crucible in an electric furnace at 1300 $^oC$ for 4 hours. Following the initial batch melting, the resultant water quenched & dried glass cullet was then remelted twice under the same conditions. The melted glass was poured into graphite molds to form ingots. The ingots were annealed at 569 $^oC$ for 6 hours and cooled to room temperature at a rate of 50 K per hour. Bulk glass composition was determined by spectrochemical analyses, based on $LiBO_2$ fusion techniques followed by analyte quantification using a Perkin-Elmer Optima 5300 inductively coupled plasma atomic emission spectroscopy (ICP-AES).

### 2.2 Bulk Glass Thermal Analysis

A 0.5cm x 0.5cm x 2cm bar was cut from a single ISG glass ingot for thermal expansion analysis on a NETZSCH PC 402 Dilatometer. A silicon standard was used for

calibration, a heating rate of 4 K/min was used, and data acquisition was automatically stopped after reaching the dilatometric softening point. Glass transition temperature was determined by a TA Instruments 2960 SDT differential thermal analysis (DTA). Ground ISG glass powder was heated in a Pt crucible from room temperature to 1450 $^{o}$C with flowing air at a heating rate of 10 K/min. High purity alumina powder was used as a reference.

**2.3 Glass Surface Preparation**

An ingot of ISG glass was cut with a 5 inch Buehler diamond saw blade to 1.0 cm x 1.0 cm x 0.2 cm. Samples were then ground with 120, 240, 400 and 600 grit silicon carbide grinding pads for planarization. Polishing of samples was carried out sequentially with 6μm (20 min), 3 μm (10 min), 1 μm (10 min), 0.25 μm (10 min), 0.1 μm (10 min) and 0.05 μm (15 min) oil-based diamond suspension sprays, using a Buehler manual polisher. Two separate polishing pads were used, Buehler Microcloth and Buehler Trident, which resulted in two different sets of polished samples. Between each grit/suspension change, the samples were carefully washed with acetone and dried by nitrogen gas flow. Final polished samples were then cleaned ultrasonically for 10 min in acetone. Selected samples from each of the two sets were then etched by soaking the samples in 1 N $NH_4OH$ at 80 $^{o}$C for 3 min, followed by rinsing with DI-water; the etched samples were then dried with nitrogen gas flow.

This resulted in 4 different polished surfaces (1) Microcloth polished unetched, (2) Microcloth polished etched, (3) Trident polished unetched, and (4) Trident polished

etched. Prior to any surface characterization such as AFM and XPS, the samples were nitrogen blown and ultraviolet ozone cleaned (UVOC) for 10 min for remove of residual hydrocarbons as well as ambient deposits/dust.

In addition to polished surfaces, freshly cut ISG glasses with a size of 1.0 cm x 1.0 cm x 0.2 cm were heat treated in a pre-heated oven at 675 $^{o}$C, 700 $^{o}$C and 725 $^{o}$C respectively for 1 hour to create 3 different sets of melt surfaces. Heat treated samples were annealed at 570 $^{o}$C for 3 hours followed by cooling in the furnace overnight (~12 hrs). Resultant samples were ultrasonically washed in acetone for 10 min and then kept in vacuum desiccator until the time of surface analyses.

**2.4 Glass Surface Composition**

The glass surface chemical composition (outermost ~8 nm) as well as local chemical environment was analyzed with a Kratos Analytical Axis Ultra X-ray photoelectron spectrometer (XPS). The XPS spectra were collected with Al Kα X-rays (non-monochromatic, beam size=100 μm) at 20 mA anode current, with an electron energy of 1486 eV and a step size of ~0.2 eV. Survey scans were performed with a pass energy of 80 eV to gain qualitative information such as peak identification and position. Peaks identified in all survey scans were used to adjust hi resolution scan binding energy range and dwell time. Pass energy for all hi resolution scans was 20 eV with a beam dwell time of ~2 s to yield a signal-to-noise ratio of >100:1 with exception of B1s peaks, which were adjusted to yield a signal-to-noise ratio of >50:1. The analyzed area was ~2-3

mm in diameter. Standard deviation of peak position and elemental concentration was evaluated by probing five different spots on a 725 $^{o}$C melt surface.

Quantitative surface chemical compositions were determined for all samples from hi-resolution scans of Si2p, Al2p, B1s, Zr3d, Na1s, Ca2p and O1s peaks. Relative sensitivity factors of all elements ($RSF_{Si}$=1, $RSF_{Al}$=0.60, $RSF_{B}$=0.57, $RSF_{Zr}$=8.62, $RSF_{Na}$=8.33, $RSF_{Ca}$=6.22 and $RSF_{O}$=2.77) were derived from hi-resolution XPS scans of fresh air-fractured pristine ISG glass surfaces, assuming that the ISG glass fracture surface was identical to the bulk ISG glass composition. XPS data, qualitative and quantitative analyses were performed with PHI MultiPak V8.0 software; peak positions were shifted/calibrated using C1s peak with the peak position at 284.60 eV. Area of each high-resolution scan XPS peak was fitted by the Shirley-model after automated background subtraction.

**2.5 Glass Surface Morphology**

Surface morphology was imaged and quantified using a Digital Instruments Nanoscope Dimension 3100 multimode atomic force microscope (AFM) equipped with Ar/$N_2$ gas floating table in Tapping Mode®. Antimony doped silicon probes (Bruker TESP, cantilever length of 125 μm) with a nominal tip radius of curvature of 8nm, nominal spring constant of 42 N/m and resonance frequency range of ~230-410 KHz were used for all measurements. Images were taken with a scanning rate of 1.0 Hz and resolution of 512 pixels X 512 pixels. Qualitative tip size and shape calibration was performed periodically during measurements using a commercially available standard

(Ted Pella Product No. TCI-BudgetSensor TipCheck). Multiple (ten 1 μm x 1 μm scans & two 10 μm x 10 μm scans) scans were taken of each sample at different locations on the surface to ensure a large-scale spatial averaging of roughness.

The root-mean-square roughness (RMS) was calculated and averaged from ten 1 μm x 1 μm images for each sample using Bruker Nanoscope Analysis software. Standard deviation was determined by dividing the standard deviation of the values by the square root of the number of scans performed on each sample. Line by line flattening and 3$^{rd}$ order plane fitting was performed on each image prior to analysis to remove any artifacts caused by the curvature of piezoelectric material, thermal drift, background vibration noise or lateral forces. Flattening removes vertical offsets between scan lines through calculation of a least-squared polynomial fit for a scan line followed by subtraction of the polynomial fit from the original scan line. Third order plane fitting calculates a third-order polynomial fit to the image in the *x*- and *y*-directions and subtracts the polynomial fit from the image, removing tilt and S-shaped bow [12]. Apparent root-mean-square roughness (RMS) is defined as the root-mean-square average of height deviations from the mean elevation plane, calculated from the relative height of each pixel in the captured image.

Surface morphology was also quantified using the power spectral density (PSD) analysis. PSD analysis evaluates surface roughness as the spread of height deviations from a mean plane, and the lateral distribution/distance over which the height variation occurs. The PSD function applied here is given as [30]:

$$S_2(f_x + f_y) = \frac{1}{L^2} * \left[\sum_{m=1}^{N}\sum_{n=1}^{N} Z_{mn} e^{-e\pi\ \Delta L(f_x m + f_y n)} (\Delta L)^2\right]^2 \quad (1)$$

where $S_2$ denotes the 2-D isotropic PSD, $L$ is the size of scanned surface, $N$ is the 1-D resolution for one direction ($x$, or $y$), $Z_{mn}$ is the profile height at location (m, n), $f_x$ & $f_y$ are the spatial frequencies in the $x$- and $y$- directions and $\Delta L = L/N$ is the distance between two adjacent sampling points [25].

This function is further translated into polar coordinates through spatial frequency and angular averaging (φ) as:

$$S_2(f) = \frac{1}{2\pi} * \int_0^{2\pi} S_2(f, \varphi)\, d\varphi \quad (2)$$

Therefore, the PSD function depends only on the frequency and can be plotted as a 2-D representation. PSD functions derived from a single AFM image are a function of scan length and sampling distance, and hold the possibility of being effected by spatial inhomogeneity across the glass surface. Any inhomogeneity, however, can be factored out by averaging PSD functions collected across a given samples surface. In this work PSD functions were averaged as:

$$PSD_{combined}(f) = [\sum_{i=1}^{M} PSD_i(f)]/M \quad (3)$$

where M is the number of scans performed on each sample. In this chapter, ten randomly distributed scanning areas (1 μm × 1 μm size) were chosen for each sample.

This PSD function was then modelled using two different approaches in order to quantify surface fractal dimension (*D*), Hurst exponent (*H*), and equivalent RMS roughness ($\sigma_{ABC}$). The fractal model was utilized to model the high frequency region (0.02 $nm^{-1}$ to 0.256 $nm^{-1}$) while the k-correlation model (or ABC model) was used to model the low-frequency region (0.001 $nm^{-1}$ to 0.02 $nm^{-1}$).

The fractal model allows the further translation of power spectral density function high frequency regions into fractal dimension and Hurst exponent, as thoroughly discussed elsewhere [31, 32]. The Hurst exponent is known as the scaling factor or roughness index, and describes the roughness spatial distribution homogeneity at a given wavelength [33, 34]. The fractal model does not allow direct comparison of roughness values at different wavelengths. However, the k-correlation model can be utilized to quantitatively describe surface topographies by fitting PSD profiles into equivalent RMS at different wavelengths [34]. Fitting of PSD profiles using the k-correlation model upon such approach (derivation of equivalent RMS, correlation length) has been discussed in detail in elsewhere[34].

## 3. Results and Discussion

### 3.1 Bulk Glass Composition

Table 2.1 shows the bulk ISG glass elemental composition measured from ICP-AES digestion. The atomic concentrations of Na, Ca, Zr, Al, B, Si and O in the bulk ISG glass are 8.0%, 1.6%, 0.4%, 2.4%, 9.4%, 18.0% and 60.1%, respectively. Minor deviations, below 0.4 %, compared to the ISG bulk glass composition (Na=7.6%,

Ca=1.7%, Zr=0.5%, Al=2.3%, B=9.6%, Si=18.0% and O=60.1%) as reported by Savannah River National Laboratory [29], were observed.

Table 2.1 Composition of Melt and Polished ISG Glass Surfaces

| Element (atm%) | Bulk Composition | Melt Surface at 675 °C | Melt Surface at 700 °C | Melt Surface at 725 °C | Micro-Cloth Polished | Micro-Cloth Polished & Etched | Trident Cloth Polished | Trident Cloth Polished & Etched | Standard Deviation of Conc. (atm%) |
|---|---|---|---|---|---|---|---|---|---|
| Na | 8 | 7.2 | 7 | 7 | 3.1 | 3.9 | 3.5 | 3.2 | ±0.3 |
| Ca | 1.7 | 1.2 | 1.2 | 1 | 1.8 | 2.8 | 2.6 | 4.5 | ±0.4 |
| Zr | 0.4 | 0.5 | 0.5 | 0.5 | 0.5 | 1.3 | 0.5 | 3.6 | ±0.0 |
| Al | 2.4 | 3.2 | 2.8 | 2.8 | 2.9 | 1.8 | 2.7 | 1.8 | ±0.1 |
| B | 9.4 | 2.9 | 4.5 | 4.2 | 5.3 | 4.4 | 5.4 | 3.4 | ±0.1 |
| Si | 17.9 | 21.7 | 21 | 21.1 | 19.4 | 18.8 | 18.8 | 17 | ±0.6 |
| O | 60.2 | 63.3 | 63 | 63.4 | 67 | 67 | 66.5 | 66.5 | ±0.4 |

### 3.2 Thermal analysis of bulk ISG glass

Figure II.1 shows the dilatometry/thermal expansion curve and the DTA curve (inset) of ISG glass. As shown in the DTA trace of Figure II.1, a "knee" between 500 °C and 600 °C were fitted by two tangent lines which intersect at 572 °C corresponding to the glass transition temperature (Tg). In addition, two broad exothermic peaks were indicated at 705 °C and 1000 °C, most likely corresponding to crystallization temperatures, as reported elsewhere [35, 36] for glasses of different compositions, but within the borosilicate glass family. The sudden drop observed on the thermal expansion curve at 594 °C denotes the dilatometric softening temperature (Td) while the glass transition temperature (Tg) is observed at 570 °C. The Tg values as determined by DTA and dilatometry (570 and 572 °C , respectively) agree well.

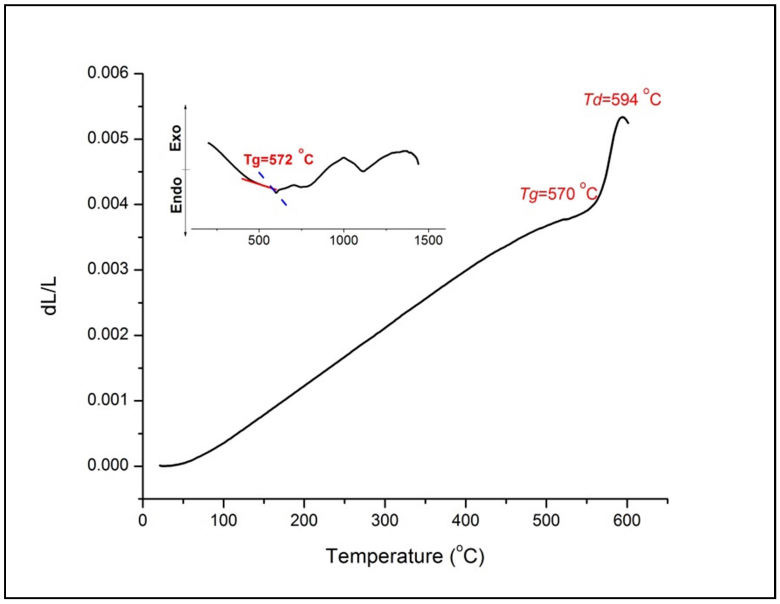


Figure II.1 Thermal expansion curve and differential thermal analysis curve for ISG glass.

Thermal analyses were utilized to guide our processing of melt surfaces. In particular, the dilatometric softening temperature can denote the transition from geometric expansion to deformation under surface strain with increasing temperature [15]. Therefore, the processing temperature to yield a smooth melt surfaces was chosen above Td at 675 °C, 700 °C, and 725 °C. In addition, the annealing temperature of melt surfaces was chosen near Tg (570 °C) to minimize the residual stress caused by heat treatment.

### 3.3 XPS analysis of ISG glass surfaces

All XPS survey scans (not shown) revealed expected elements on the surface of all samples. All peaks were identified, and the results are consistent with bulk chemical analysis. Minimal contamination, in only trace amounts, was observed on some polished samples. Table 2.1 shows the quantitative composition of melt and polished surfaces, as determined by high-resolution scans.

All melt surfaces showed Na ion concentration depletion of $\leq$ 1.0 % as compared to the bulk pristine ISG glass, while Ca ion concentration on the ISG glass melt surfaces were depleted $\leq$ 0.6% as compared to the bulk glass. Zr showed no measurable difference between the melt surfaces and the bulk composition. Melt surfaces showed a slight enrichment of Al, between 0.4 and 0.8%, and depletion of B, between 4.9 and 6.5%, when compared to the bulk composition. Finally, melt surfaces showed a slight enrichment in Si and O on the surface, between 3.1 and 3.8% and 2.9 and 3.3% respectively, as compared to the bulk. However, no clear trends were observed for melt surface composition as a function of heat treatment/processing temperature. The depletion of B and Na is assumed to be associated with the high vapor pressure of both elements as documented elsewhere [15]. Similar depletion of Ca and Al after heat treatment of aluminosilicate glasses has also been previously reported [11].

All polished and polished/etched surfaces showed Na ion concentration depletions of $\leq$ 4.9% as compared to the bulk pristine ISG glass, while Ca ion concentrations were enriched by $\leq$ 2.9%. Zr ion concentration showed no change in concentration with polishing, but enrichment of up to 3.2% with polishing and etching as compared to the bulk composition. Polished surfaces showed a slight enrichment of Al, while polished/etched surfaces showed a slight depletion in Al, as compared to the bulk composition. In all cases, both polished and polished/etched, surfaces were depleted in B (between 4 and 6%) as compared to the bulk composition, with polished/etched surfaces depleted more so than simply the polished surfaces. In all cases, polished and

polished/etched surfaces were enriched (≤ 1.5%) in Si with respect to the bulk composition, with exception of the Trident cloth polished/etched which was depleted by 0.9%. All polished and polished/etched surfaces were enriched by up to 6.9% in O. There is no clear trend in surface composition as a function of polishing cloth used. However, some general surface composition trends were observed between polished and polished/etched surfaces. In all cases, post-polishing etching of surfaces resulted in (1) a general increase in a concentration of surface Ca and Zr, (2) a decrease in Al, B, and Si concentration, (3) no observable trend in Na concentration, and (4) no change in O concentration.

Planarization of glass surfaces, which in this work consists of the grinding and polishing, is a chemo-mechanical process [37, 38, 39]. The chemical processes associated in the grinding and polishing are a complex function of the chemistry and concentration of the water used during grinding and the composition of the oils used during polishing. During these processes, it has been proposed that the surface composition is a function of hydrolysis reactions between the glass surface and the grinding/polishing media; in particular, protons in water replace modifier ions within the glass surface. Such ion exchange renders a leaching of modifiers, which is consistent with our findings of significant Na depletion after polishing.

Walter [38] and Spierings [39] proposed that the chemical etching of glasses are the result of 2 different mechanisms: 1) leaching of modifier ions (e.g. Na, Ca) through ion-exchange reactions with protons and 2) dissolution of network formers (e.g. Si, Al, B)

with anionic attack. Our XPS results, after etching in a basic solution ($NH_4OH$), showed observable decreases in the network former Al, B, Si concentrations, while the Na concentration remained relatively unchanged. Such results are consistent with the above mentioned theory; as we would expect anionic attack, in this case $OH^-$, to result in network former dissolution and not preferential modifier ion release. The increases in the concentration of Ca and O post etching are consistent with the results reported by Saito [37] in a similar borosilicate glass system.

Si2p peaks for all glass surfaces are located at peak positions of ~102.5 eV – 102.7 eV with a FWHM of ~1.7 eV – 1.8 eV; Al2p peaks are located at peak positions of ~74.0 eV – 74.3 eV with a FWHM of ~1.3 eV – 1.5 eV; B1s peaks are located at the peak positions of ~192.2 eV – 192.5 eV with a FWHM of ~1.4 eV – 1.6 eV; and $Zr3d_{3/2}$ and $Zr3d_{5/2}$ peaks are located at peak positions of ~183.9 eV – 185.2 eV and 181.1 eV – 182.7 eV respectively. The variations in peak positions and FWHMs are within experimental error (peak position standard deviation was measured as 0.08 eV) and no changes in FWHM as well as peak positions with processing of melt, polished, or polished/etched surface of Si, Al, B, or Zr can be observed from these results.

Si, B, Al and Zr are assumed to be network forming or intermediate ions within the glass structure [9, 40, 41]. It is of interest to examine whether the processing methods employed here have an effect on the short range order of the glass surface structure with respect to these elements. It has been shown previously that an element's peak position and FWHM are sensitive to changes in short range order of glasses [22]. Given the lack of

such changes observed in XPS analysis, it is thus speculated that chemical environments of the network forming or intermediate ions ISG glass surfaces did not significantly change with processing conditions.

### 3.4 AFM imaging & statistics of melt/polished ISG glass surfaces

Representative AFM images of all glass surfaces are shown in Figure II.2. All images have an x-y scale of 1 micron and a z-scale of 25 nanometers. All polished and polished/etched surfaces show relatively smooth surfaces with linear features/grooves. In addition, these grooves are clearly observed and pronounced on the polished/etched surfaces. It is assumed that these linear features are scratches associated with the polishing of the surfaces, and have been previously reported throughout the literature [11]. The observation that the scratches are more pronounced after etching suggests that preferential reaction of the etchant and glass surface is occurring along these scratches. Similar results were reported by L. Wong et. al. [42] where the authors observed growth of polishing induced scratches after exposure to chemical etchants. It was concluded by L. Wong and others that the growth of polishing scratches after etching is caused by the preferential etching of individual fracture sites within the polishing scratches [42, 43].

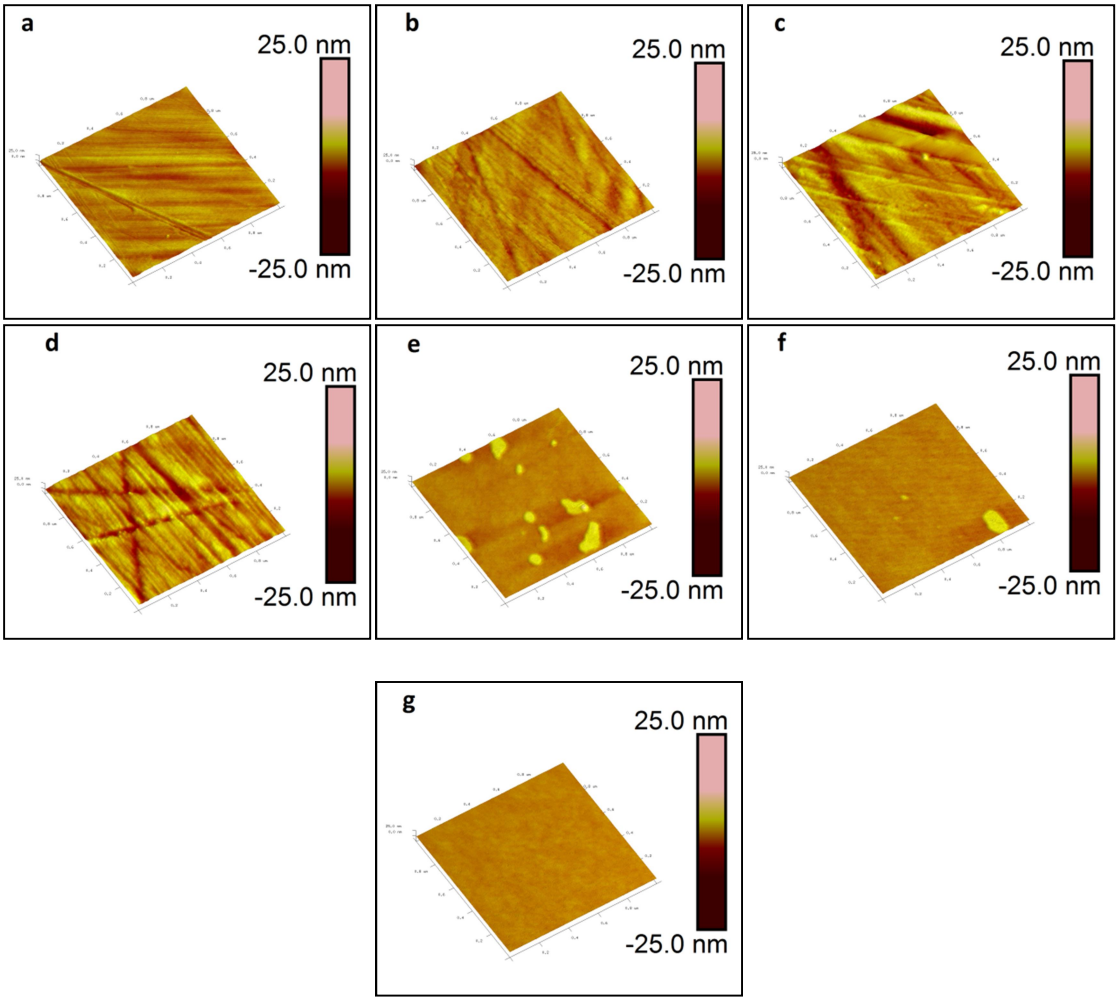


Figure II.2 3-D surface topography of ISG glasses; (a) micro cloth polished, (b) micro cloth polished & etched, (c) trident cloth polished, (d) trident cloth polished & etched, (e) 675 $^{o}$C melt process, (f) 700 $^{o}$C melt process and (g) 725 $^{o}$C melt process. Scan area of all images are 1µm × 1µm with a 25nm z-scale.

Images of the melt surfaces are significantly different to the polished surfaces. Melt surfaces processed at 675 and 700 $^{o}$C show smooth surfaces with randomly distributed positive relief features with a lateral resolution on the order of 10's to 200 nm. The positive relief features were captured in all ten 1 µm × 1 µm scans for 675 $^{o}$C and 700 $^{o}$C melt surfaces, and the number of features per scan as well as the height from mean plane is random. However, no positive relief features, but instead a smooth

featureless surface is observed on 725 °C melt surfaces. It is speculated that the presence of the positive relief features may be associated with the broad exothermic peak at 705 °C observed in the DTA scan in Figure II.1 at 705 °C as previously suggested by others for similar systems [44, 45]. Thus, we assume here the positive relief features are mostly likely to be a result of surface crystallization.

Table 2.2 shows the apparent RMS roughness (nm) of all melt surfaces. Two different apparent RMS roughnesses are reported for all melt surfaces; one calculated including all positive relief features and one calculated after manual removal of positive relief features. The removal of positive relief features allows the direct observation of glass surface apparent roughness after heat treatment. After removal of positive relief features apparent RMS does not change, within error of the measurement. In general, the apparent RMS roughness of the 675 and 700 °C melt surfaces, regardless of positive relief feature removal, is less than 1.5 nm while the apparent RMS roughness of the 725 °C melt surface is 0.3 nm. While it is not clear why the removal of the positive relief features does not cause a significant change in the apparent RMS roughness, one trend is clear, that is the apparent RMS roughness of the 725 °C melt surface is significantly less than that of the other temperatures. Such phenomenon was also reported in [43, 46] and it was concluded that the higher heat treatment temperature can lower the viscosity hurdle for glass surface expansion and further smooth the surface. The apparent RMS roughness of the 725 °C melt surface reported here is similar to RMS roughness value reported for other glass melt surfaces [e.g. [11]].

Table 2.2 Fitting Coefficients of PSD Spectra of Melt and Polished ISG Glass Surfaces

| Sample Description | Fractal | | | k-Correlation | | | | |
|---|---|---|---|---|---|---|---|---|
| | D | H | | A ($10^5$nm) | B (nm) | C | Equivalent RMS (nm) | Apparent RMS (nm) |
| Melt Surface at 675 °C | 2.75 | 0.25 | | 6.59 | 420.98 | 2.97 | 0.34 | 1.21±0.09 |
| Melt Surface at 675 °C with Feature Removal | 2.69 | 0.31 | | 5.45 | 169.21 | 5.33 | 0.53 | 1.18±0.07 |
| Melt Surface at 700 °C | 2.84 | 0.16 | | 4.17 | 345.39 | 3.96 | 0.27 | 1.02±0.08 |
| Melt Surface at 700 °C with Feature Removal | 2.81 | 0.19 | | 6.73 | 130.23 | 11.76 | 0.48 | 0.97±0.06 |
| Melt Surface at 725 °C | 2.93 | 0.07 | | 0.38 | 692.04 | 1.38 | 0.11 | 0.30±0.01 |
| Micro Cloth Polished | 2.42 | 0.58 | | 364 | 660.74 | 3.43 | 1.47 | 1.10±0.07 |
| Micro Cloth Polished & Etched | 2.6 | 0.4 | | 49.1 | 702.8 | 2.43 | 0.66 | 1.04±0.03 |
| Trident Cloth Polished | 2.18 | 0.82 | | 274 | 516.94 | 3.54 | 1.59 | 1.83±0.08 |
| Trident Cloth Polished & Etched | 2.09 | 0.91 | | 4.94 | 101.38 | 8.69 | 0.63 | 1.49±0.03 |

Table 2.2 shows the apparent RMS roughness (nm) of all polished and polished/etched surfaces. All apparent RMS values are between ~1.04 and 1.83 nm. The Tridentcloth results in a glass surface with lower apparent RMS roughness than that of the Microcloth. It is assumed the different in apparent RMS roughness is due to the difference in materials of the two polishing cloths; the Microcloth is a long-napped rayon cloth while the trident cloth is a nap-free woven cloth. In addition after etching, the

Microcloth polished surface shows no significant change in apparent RMS roughness, while the Tridentcloth polished surface shows a marked decrease after etching. While the overall mechanism responsible is not clear, the type of polishing cloth used certainly effects the apparent RMS roughness of the resultant glass surface. Polished surfaces in our study yield an apparent roughness value close to reported values (~ 0.8 nm to 2.3 nm) in other silicate glass systems [e.g. [43, 47]].

### 3.5 Power spectral density (PSD) analysis of ISG glass surfaces

Figure II.3 shows the PSD profiles of all processed ISG glass surfaces. Two clear regions are observed for all PSD profiles shown in Figure II.3: a "high frequency region", above 0.02 $nm^{-1}$ and a "low frequency region", below 0.02 $nm^{-1}$. It has been proposed that the high frequency region could be fit using the fractal model while the low frequency region could be fit using the k-correlation model [25].

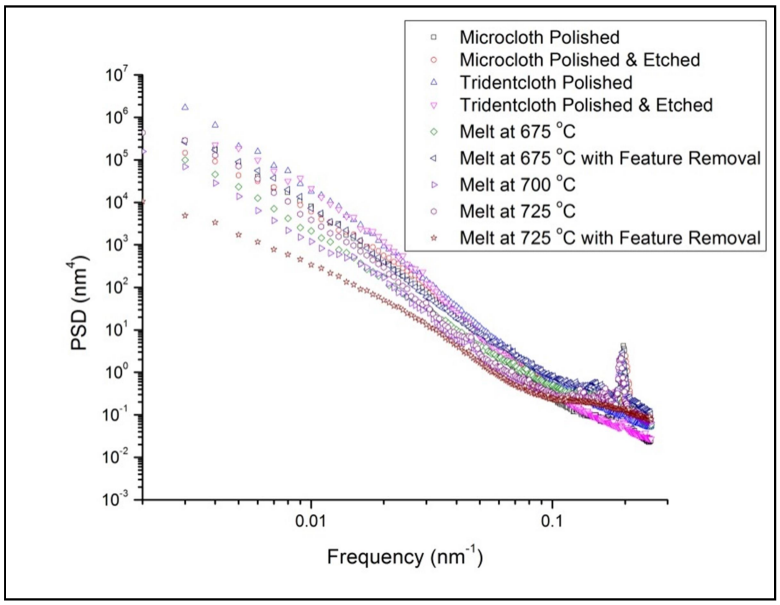


Figure II.3 The experimental PSD profiles of all ISG glass surfaces.

Figure II.4 shows the PSD profile fitting of the 725 °C melt surface using both the Fractal model and ABC (k-correlation) model. In Figure II.4 as well as other fittings in this work, the ABC model is presented by a dashed line; the solid line is the fitted Fractal model, and the raw data is displayed as scattered circles. The fractal model (as shown in Eq.4) was used to fit the PSD profile region beyond the spatial frequency of 0.02 $nm^{-1}$ to derive spatial parameters D & H from the slope of the linear fitted curve.

$$PSD_{fractal}(f; K, s) = \frac{K}{f^s} \tag{4}$$

Fractal dimension is used as a scaling index, which determines the fineness of a geometry/surface with measurement scale variation [48]. In particular, fractal dimension, reported as a value between 2 and 3, can provide information on roughness variation with a given scanning scale; with a value of 2 representing a Euclidean surface and a value of 3 representing an infinitely rough surface [33].

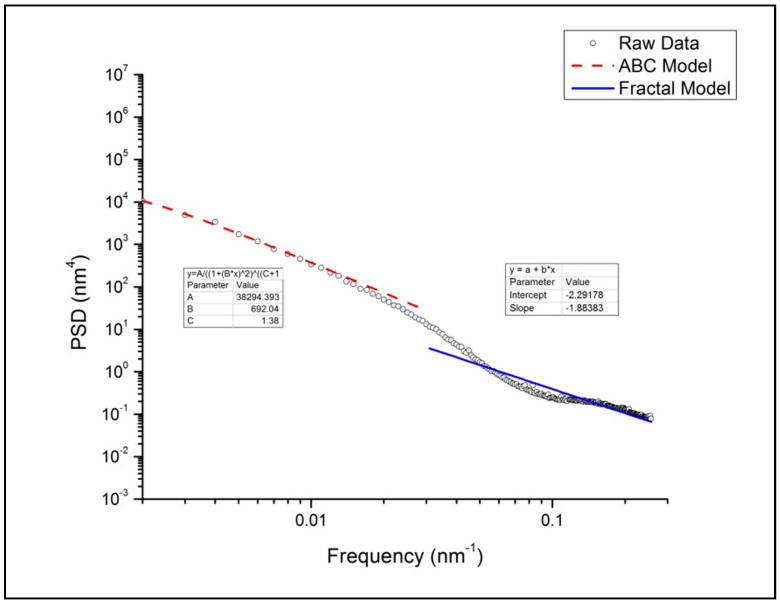


Figure II.4 Fitting of experimental PSD profile of 725 °C melt processed ISG glass surfaces using both the Fractal model and ABC (k-correlation) model.

The Hurst exponent is considered as a roughness index & roughness scaling factor [34]. A Hurst value within the range of 0~0.5 indicates a spatial frequency series with continuous alternating features of high and low values while a Hurst exponent value between 0.5 and 1 represents a spatial frequency series with positive autocorrelation, presenting abrupt value changes in a series of spatial frequencies. Thus, a Hurst exponent in the range of 0~0.5 indicates a rough surface with spatial homogenous distribution of roughness while a Hurst exponent between 0.5~1 suggests a non-homogeneous surface [49, 50]. However, while useful to provide spatial homogeneity information of a surface, the fractal model lacks the ability to present a physical roughness parameter that can be comparable to the apparent RMS.

This inherent disadvantage of the fractal model was overcome here by the use of the ABC-model in this study. Below the spatial frequency of 0.02 $nm^{-1}$, the PSD profile was fitted by the ABC model (as Eq.5) to extract parameter A, B, and C, which can be used to derive the equivalent RMS by Eq.6.

$$PSD_{ABC} = \frac{A}{(1+B^2f^2)^{\frac{C+1}{2}}} \quad (5)$$

$$\sigma_{ABC}^2 = \frac{2\pi A}{B^2(C-1)} \quad (6)$$

As shown by Figure II.4, the ABC model fits the “knee” region of the PSD profile below the spatial frequency of 0.02 $nm^{-1}$. The position of the “knee” is determined by parameter B and is an equivalent term to the correlation length. Beyond the “knee” region, the ABC model is mathematically equivalent to fractal model since parameter C is the only dominant factor to PSD values. Thus, in this study both models were adopted to complimentary characterize the surface morphology as well as spatial homogeneity. Morphological parameters, including fractal dimension, Hurst exponent, and equivalent

RMS roughness, resulting from the modelling of all individual PSD curves are shown in Table 2.2.

Figure II.4 shows the PSD profile fitting of the 725 $^{o}$C melt surface and Figure II.5a-d shows the fitting of experimental PSD profile of 675 $^{o}$C melt surface, 675 $^{o}$C melt surface with positive relief feature removal, 700 $^{o}$C melt surface, and 700 $^{o}$C melt surface with positive relief feature removal, respectively.

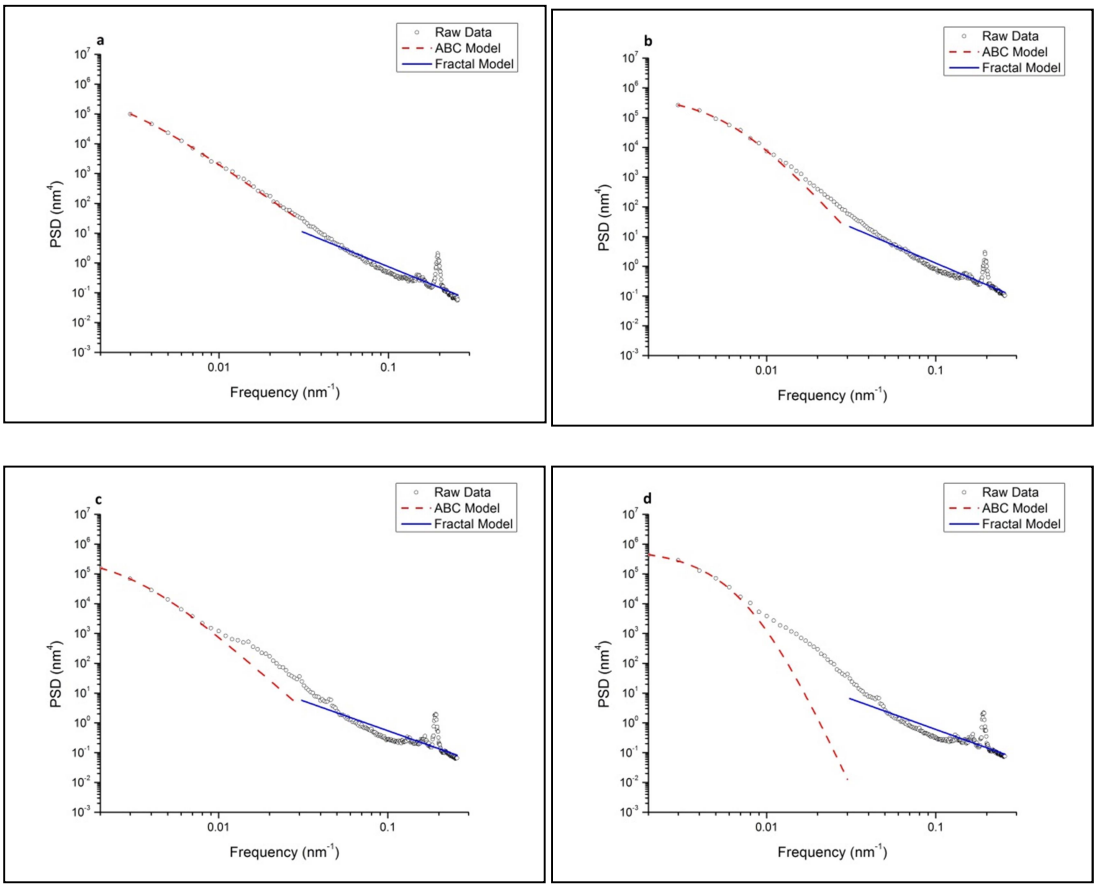


Figure II.5 Fitting of the experimental PSD profiles of (a) 675 $^{o}$C melt surface, (b) 675 $^{o}$C melt surface with feature removal, (c) 700 $^{o}$C melt surface and (d) 700 $^{o}$C melt surface with feature removal using the Fractal model and ABC (k-correlation) model.

The fractal dimension (D), Hurst exponent (H), correlation length (B) and equivalent RMS are 2.75, 0.25, 420.98 nm and 0.34 nm, respectively, for 675 $^{o}$C melt surface. After removing the positive relief features, the D, H, B and equivalent RMS were

reported as 2.69, 0.31, 169.21 nm and 0.53 nm, respectively. For the 700 $^{o}$C melt surface, the D, H, B and equivalent RMS is 2.84, 0.16, 345.39 nm and 0.27 nm, respectively. D, H, B and equivalent RMS of the 700 $^{o}$C melt surface were reported as 2.81, 0.19, 130.23 nm and 0.48 nm after positive feature removal.

In comparison, for the 725 $^{o}$C melt surface, the D, H, B and equivalent RMS is 2.93, 0.07, 692.04 nm and 0.11 nm respectively. All values are summarized in Table 2.2. A few trends are observable when comparing these values. In general, the fractal dimension decreases upon removal of positive relief features and increases with increasing processing temperature. The Hurst parameter increases with removal of positive relief features and decreases with an increase in processing temperature. The correlation length decreases with removal of positive relief features and no clear trend is observed with processing temperature. Finally, the equivalent RMS increases with the removal of positive relief features and decreases with increasing processing temperature.

After removing the positive relief features on 675 $^{o}$C and 700 $^{o}$C melt surfaces and comparing those results to the 725 $^{o}$C melt surface, it was found that the roughness (both apparent RMS and equivalent RMS) decreases with increasing heat treatment temperature. It is proposed here that the higher heat treatment temperature lowers the viscosity of the glass, and thus smoothing the surface by surface expansion. In addition, the spatial distribution of roughness became more homogeneous with increasing heat treatment temperature (increased D values, and decreased H values) as a result of heat induced surface smoothening.

Experimental and fitted PSD profiles of Microcloth polished, Microcloth polished/etched, Tridentcloth polished and Tridentcloth polished/etched surfaces are shown as Figure II.6a-d. The resultant fitted parameters D, H, B and equivalent RMS are listed in Table 2.2.

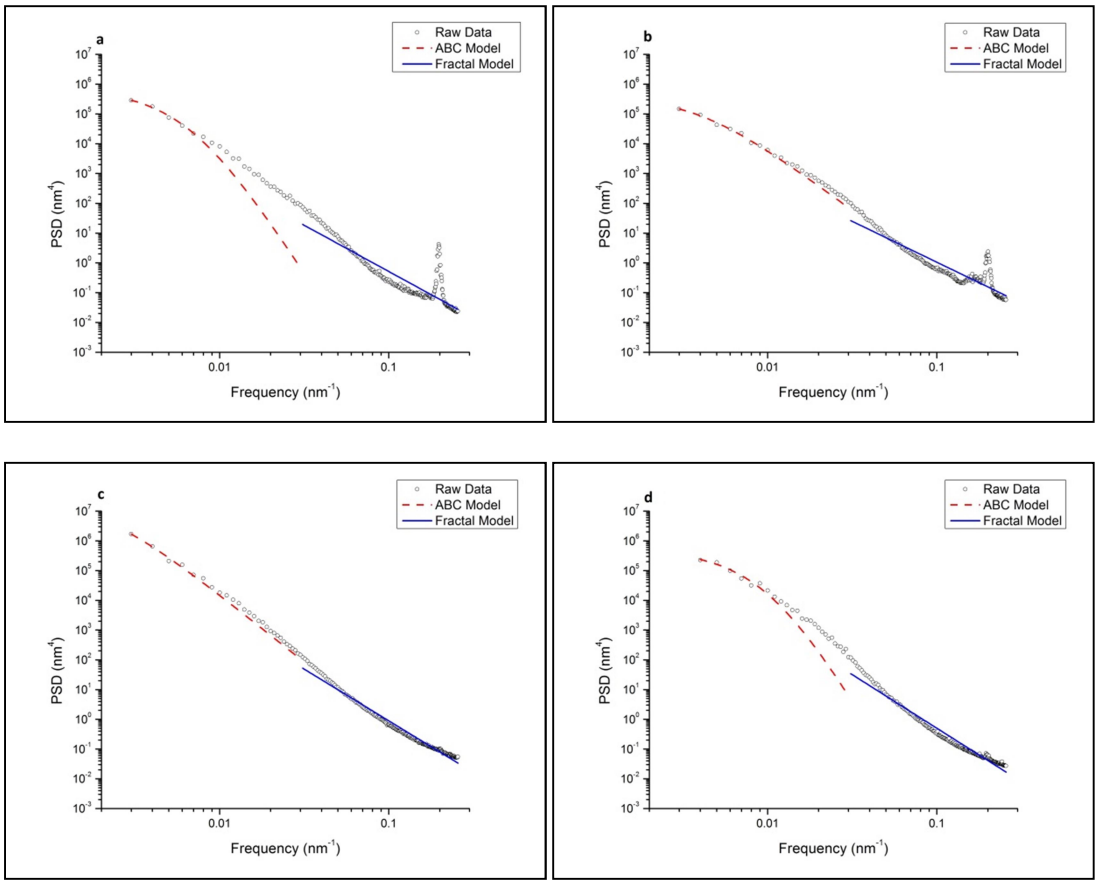


Figure II.6 Fitting of the experimental PSD profiles of (a) micro cloth polished, (b) micro cloth polished & etched, (c) trident cloth polished and (d) trident cloth polished & etched ISG glass surfaces using the Fractal model and ABC (k-correlation) model.

For the Microcloth polished surface, the D, H, B and equivalent RMS were reported as 2.42, 0.58, 660.74 nm and 1.47 nm, respectively. For the Microcloth polished/etched surface the D, H, B and equivalent RMS were reported as 2.60, 0.40, 702.80 nm and 0.66 nm, respectively. For the trident-cloth polished surface, the D, H, B

and equivalent RMS were reported as 2.18, 0.82, 516.94 nm and 1.59 nm respectively. For the trident-cloth polished/etched surface the D, H, B and equivalent RMS were reported as 2.09, 0.91, 101.38 nm and 0.63 nm, respectively.

The fractal dimension, Hurst parameter, and correlation length of polished and polished/etched surfaces vary with type of polishing cloth used; however, a trend with respect any changes with the etching of polished surfaces is not observed. However, the equivalent RMS roughnesses of polished and polished/etched surfaces are observed to be a function of polishing cloth, and equivalent RMS roughness decreases after etching of polished surfaces. Spierings [39] and L. Wong [42] both concluded that the decrease of RMS roughness post etching is due to the coalescence of intersecting scratches, and the results here follow such conclusions.

One of the purposes of this work was to develop a method to produce both melt and polished glass surfaces which are atomically smooth with good spatial homogeneity and have a similar composition to that of the bulk glass. The results show that 725 $^{o}$C melt surfaces have the lowest apparent/equivalent RMS roughness value (0.30±0.01 nm/ 0.11 nm), most homogeneous distribution of roughness (D=2.93, H=0.07) and the longest correlation length (B=692.04 nm). In addition, these surfaces show only minor deviations in composition with respect to the bulk, with the exception of boron. The Microcloth polished/etched surface is shown to be the smoothest and most spatially homogenous surface (apparent RMS=1.04±0.03 nm, equivalent RMS=0.66 nm, D=2.60 and H=0.40). In addition, it is also shown that this surface is closest to the bulk composition when compared to all other polished and polished/etched surfaces.

## Conclusions

In this chapter, ISG glass surfaces were prepared through both melting and polishing/etching and the surface composition and morphology were quantified as a function of processing method. In particular, for the first time glass surface morphology as a function of processing method was quantified using PSD analysis, followed by both fractal and ABC model fitting, resulting in a comprehensive description of the spatial distribution of roughness.

All melt surfaces showed a depletion in Na, Ca, and B with respect to the bulk composition. Polished/etched surfaces showed a depletion in Na, B, and Al with respect to the bulk composition. The chemical bonding environments of the surface elements were not affected by either processing method. It was found that increasing heat treatment temperature of melt surfaces lead to a decrease in equivalent roughness and an increased spatial homogeneity of roughness while etching of polished ISG glass surfaces decreases the roughness and spatial distribution homogeneity of roughness. It has also been shown that the roughest and most non-homogenous glass surface was found to be the most compositionally altered.

## References

1. P. Bocko, P. Fenn, L. Morse, and F. Okamoto, "Surface chemistry and microstructure of flat panel display substrates," *SID 91 Digest,* 675 (1991).
2. S. Tang, V. Y. Vassiliev, S. Mridha, and L. Chan, "Investigation of borophosphosilicate glass roughness and planarization with the atomic force microscope technique," *Thin Solid Films,* 352[1] 77-84 (1999).

3. M. Depas, M. Heynes, T. Nigam, K. Kenis, H. Sprey, R. Wilhelm, A. Crossley, C. Sofield, and D. Graf, "Electrochem. Soc." in. PV-96-1, 352, 1996.

4. M. Kimura, J. Mitsuhashi, and H. Koyama, "$Si/SiO_2$ interface states and neutral oxide traps induced by surface microroughness," *Journal of Applied Physics,* 77[4] 1569-75 (1995).

5. S. Dériano, T. Rouxel, S. Malherbe, J. Rocherullé, G. Duisit, and G. Jezequel, "Mechanical strength improvement of a soda-lime–silica glass by thermal treatment under flowing gas," *Journal of the European Ceramic Society,* 24[9] 2803-12 (2004).

6. A. Olofinjana and N. Voo, "The role of surface oxide composition on the fatigue strength of metallic glass wire," *Applied Surface Science,* 295 86-93 (2014).

7. V. Cannillo, F. Pierli, I. Ronchetti, C. Siligardi, and D. Zaffe, "Chemical durability and microstructural analysis of glasses soaked in water and in biological fluids," *Ceramics International,* 35[7] 2853-69 (2009).

8. J. Massera, K. Bourhis, L. Petit, M. Couzi, L. Hupa, M. Hupa, J.-J. Videau, and T. Cardinal, "Effect of the glass composition on the chemical durability of zinc-phosphate-based glasses in aqueous solutions," *Journal of Physics and Chemistry of Solids,* 74[1] 121-27 (2013).

9. N. Mellott, S. Brantley, J. Hamilton, and C. Pantano, "Evaluation of surface preparation methods for glass," *Surface and Interface Analysis,* 31[5] 362-68 (2001).

10. C. Cailleteau, F. Angeli, F. Devreux, S. Gin, J. Jestin, P. Jollivet, and O. Spalla, "Insight into silicate-glass corrosion mechanisms," *Nature Materials,* 7[12] 978-83 (2008).

11. N. Mellott, S. Brantley, and C. Pantano, "Topography of polished plates of albite crystal and glass during dissolution," *Water-Rock Interactions, Ore Deposits, and Environmental Geochemistry: A Tribute to David A. Crerar. The Geochemical Society, Special Publication,* 7 83-95 (2002).

12. N. Mellott, C. Durucan, C. Pantano, and M. Guglielmi, "Commercial and laboratory prepared titanium dioxide thin films for self-cleaning glasses: photocatalytic performance and chemical durability," *Thin Solid Films,* 502[1] 112-20 (2006).

13. Y. Namba, M. Abe, and A. Kobayashi, "Ultraprecision grinding of optical glasses to produce super-smooth surfaces," *CIRP Annals-Manufacturing Technology,* 42[1] 417-20 (1993).

14. R. H. M. Jafar, M. Papini, and J. Spelt, "Simulation of erosive smoothing in the abrasive jet micro-machining of glass," *Journal of Materials Processing Technology,* 213[12] 2254-61 (2013).

15. L. M. Cook, "Chemical processes in glass polishing," *Journal of Non-Crystalline solids,* 120[1] 152-71 (1990).

16. L. M. Cook and K.-H. Mader, "Leached antireflection surfaces. III: Chemical release data for leached BK-7 borosilicate glass," *Glastechnische Berichte,* 60 333-39 (1987).

17. L. M. Cook, A. Marker III, K.-H. Mader, H. Bach, and H. Müller, "Leached antireflection surfaces. II: Characterization of surfaces produced by the neutral solution process," *Glastechnische Berichte,* 60 302-11 (1987).

18. H. Dunken, "Surface chemistry of optical glasses," *Journal of Non-Crystalline Solids,* 129[1-3] 64-75 (1991).

19. E. Onyiriuka, "Zinc phosphate glass surfaces studied by XPS," *Journal of non-crystalline solids,* 163[3] 268-73 (1993).

20. D. Sprenger, H. Bach, W. Meisel, and P. Gütlich, "XPS study of leached glass surfaces," *Journal of Non-Crystalline Solids,* 126[1-2] 111-29 (1990).

21. C. D. Wagner and G. Muilenberg, "Handbook of X-ray photoelectron spectroscopy.″ Perkin-Elmer, Eden Prarie, Minnesota, (1979).

22. R. K. Brow, "An XPS study of oxygen bonding in zinc phosphate and zinc borophosphate glasses," *Journal of Non-Crystalline Solids,* 194[3] 267-73 (1996).

23. R. Brückner, H.-U. Chun, H. Goretzki, and M. Sammet, "XPS measurements and structural aspects of silicate and phosphate glasses," *Journal of Non-Crystalline Solids,* 42[1] 49-60 (1980).

24. S. Fang, S. Haplepete, W. Chen, C. Helms, and H. Edwards, "Analyzing atomic force microscopy images using spectral methods," *Journal of Applied Physics,* 82[12] 5891-98 (1997).

25. M. Senthilkumar, N. Sahoo, S. Thakur, and R. Tokas, "Characterization of microroughness parameters in gadolinium oxide thin films: A study based on extended power spectral density analyses," *Applied Surface Science,* 252[5] 1608-19 (2005).

26. S. D. Halepete, H. Lin, S. J. Fang, and C. Helms, "Analyzing Atomic Force Micrographs Using Spectral Methods." pp. 383 in MRS Proceedings. Vol. 386, 1995.

27. S. Fang, W. Chen, T. Yamanaka, and C. Helms, "Comparison of Si surface roughness measured by atomic force microscopy and ellipsometry," *Applied Physics Letters,* 68[20] 2837-39 (1996).

28. Y. Inagaki, T. Kikunaga, K. Idemitsu, and T. Arima, "Initial Dissolution Rate of the International Simple Glass as a Function of pH and Temperature Measured Using Microchannel Flow-Through Test Method," *International Journal of Applied Glass Science,* 4[4] 317-27 (2013).

29. S. R. N. Laboratory, "FCT Quality Assurance Program Document." in FCT Quality Assurance Program Document. Savannah River National Laboratory, 2012.

30. J. Ferré-Borrull, A. Duparré, and E. Quesnel, "Procedure to characterize microroughness of optical thin films: application to ion-beam-sputtered vacuum-ultraviolet coatings," *Applied Optics,* 40[13] 2190-99 (2001).

31. E. L. Church, "Fractal surface finish," *Applied Optics,* 27[8] 1518-26 (1988).

32. J. C. Russ, "Fractal surfaces." Springer Science & Business Media, (2013).

33. P. Dumas, B. Bouffakhreddine, C. Amra, O. Vatel, E. Andre, R. Galindo, and F. Salvan, "Quantitative microroughness analysis down to the nanometer scale," *EPL (Europhysics Letters),* 22[9] 717 (1993).

34. E. L. Church, P. Z. Takacs, and T. A. Leonard, "The prediction of BRDFs from surface profile measurements." pp. 136-50 in 33rd Annual Techincal Symposium, International Society for Optics and Photonics, 1990.

35. H. Guo, Y. Gong, and S. Gao, "Preparation of high strength foam glass–ceramics from waste cathode ray tube," *Materials Letters,* 64[8] 997-99 (2010).

36. P. K. Ojha, T. Chongdar, N. Gokhale, and A. Kulkarni, "Investigation of crystallization kinetic of $SrO–La_2O_3–Al_2O_3–B_2O_3–SiO_2$ glass and its suitability for SOFC sealant," *international Journal of Hydrogen Energy,* 36[22] 14996-5001 (2011).

37. Y. Saito, S. Okamoto, H. Inomata, and J. Kurachi, "Mechanism of the etching rate change of aluminosilicate glass in HF acid with micro-indentation," *Applied Surface Science,* 255[5] 2290-94 (2008).

38. H. Walters and P. Adams, "The chemical durability of optical glass," *Applied Optics,* 7[5] 845-48 (1968).

39. G. Spierings, "Compositional effects in the dissolution of multicomponent silicate glasses in aqueous HF solutions," *Journal of Materials Science,* 26[12] 3329-36 (1991).

40. L.-S. Du and J. F. Stebbins, "Network connectivity in aluminoborosilicate glasses: a high-resolution $^{11}B$, $^{27}Al$ and $^{17}O$ NMR study," *Journal of Non-Crystalline Solids,* 351[43] 3508-20 (2005).

41. K. A. Murphy, N. M. Washton, J. V. Ryan, C. G. Pantano, and K. T. Mueller, "Solid-state NMR examination of alteration layers on nuclear waste glasses," *Journal of Non-Crystalline Solids,* 369 44-54 (2013).

42. L. Wong, T. Suratwala, M. Feit, P. Miller, and R. Steele, "The effect of HF/NH 4 F etching on the morphology of surface fractures on fused silica," *Journal of Non-Crystalline Solids,* 355[13] 797-810 (2009).

43. P. K. Gupta, D. Inniss, C. R. Kurkjian, and Q. Zhong, "Nanoscale roughness of oxide glass surfaces," *Journal of Non-Crystalline Solids,* 262[1] 200-06 (2000).

44. A.-M. Hu, K.-M. Liang, M. Li, and D.-L. Mao, "Effect of nucleation temperatures and time on crystallization behavior and properties of $Li_2O$–$Al_2O_3$–$SiO_2$ glasses," *Materials Chemistry and Physics,* 98[2] 430-33 (2006).

45. N. Khan, D. Dollimore, K. Alexander, and F. Wilburn, "The origin of the exothermic peak in the thermal decomposition of basic magnesium carbonate," *Thermochimica Acta,* 367 321-33 (2001).

46. S.-B. Shim, D.-S. Kim, S. Hwang, and H. Kim, "Wetting and surface tension of bismate glass melt," *Thermochimica Acta,* 496[1] 93-96 (2009).

47. E. Rädlein and G. H. Frischat, "Atomic force microscopy as a tool to correlate nanostructure to properties of glasses," *Journal of Non-Crystalline Solids,* 222 69-82 (1997).

48. J. B. Bassingthwaighte and G. M. Raymond, "Evaluating rescaled range analysis for time series," *Annals of Biomedical Engineering,* 22[4] 432-44 (1994).

49. Y. Zhang and S. Sundararajan, "Generating random surfaces with desired autocorrelation length," *Applied Physics Letters,* 88[14] 141903 (2006).

50. A. Novak and V. Novak, "Roughness of amorphous, polycrystalline and hemispherical-grained silicon films," *Technical Physics Letters,* 39[10] 858-61 (2013).

# CHAPTER III. A LEAP TOWARDS THE UNDERSTANDING OF GLASS DISSOLUTION: A NOVEL ATOMIC FORCE MICROSCOPY APPROACH

## 1. Introduction

The corrosion of silicate minerals and glasses is of great interest given its critical role in environmental, geological [1], biomedical [2], and industrial processes [3, 4]. Mechanistic and kinetic understandings of glass corrosion are fundamental for predicting the long-term corrosion behavior of silicate glasses in contact with aqueous fluids [3], evaluating the performance of insulating glass fibers or composites under humidity [5], and protecting consumer product panel glasses exposed to atmospheric weathering [6]. Moreover, accurate measurement of dissolution rates of glasses is of great importance for the protection of optical glasses, historic glasses, and archaeological glasses from degradation when being exposed to the atmosphere. The geochemical community encounters the same challenge of measuring the dissolution rates of basaltic glass in seawater when calculating the balance of ocean chemistry or assessing the sequestration of carbon dioxides [7]. Given the fact that the oceanic crust has a significant amount of basaltic glass, the weathering of glass plays an important role in the global carbon cycle. Other than these aspects that glass dissolution behavior could impact, the measuring of nuclear waste glass dissolution is a prioritized task to ensure the confidence of using nuclear energy as a suitable energy alternative in the alleviation of global climate change, as well as relieving the ballooning demand for cleaner and sustainable energy [8].

Spent nuclear fuels or nuclear wastes are often vitrified in a chemically durable borosilicate glass matrix (e.g. SON68 glass, France; British Magnox, UK; and etc.), and the vitrified waste forms will eventually be encapsulated in stainless steel canisters at geological repositories [9, 10]. The primary interaction affecting the waste form lifetime and radionuclides release to the environment of this disposal strategy is the aqueous corrosion of the nuclear waste glass with groundwater. Thus, the kinetics of glass corrosion has attracted a great deal of attention from experimentalists and theorists. From both experimental and modeling perspectives, the dissolution rates of glasses of interest were studied as a function of temperature, pH, glass composition, Si saturation in solution, and many other experimental conditions [11, 12, 13, 14]. These experiments were often carried out in dilute solutions (non-saturated state of Si) to parameterize the rate equation, quantify the rate of forward reaction, and obtain the maximum dissolution rate. Often, dissolution rates were obtained by measuring the concentrations of ions in the leachate solution. One challenge of parameterizing dissolution rates through the release of ions is the measurement of certain elements (e.g. Si) at their saturation limit of solution. Through decades of study on the dissolution behavior of silicate glasses, it has been reported that an outer gel zone ($SiO_2$ enrich layer) forms on the reaction front of glass approximately when the Si concentration reaches saturation [15]. The formation of silica-rich gel zone limits the ability to measure dissolution rate using Si as a tracer since the Si tends to be incongruently retained in the alteration layer when compared to other more mobile species like B and Na. Recently, Hellmann and et. al. [16] reported that the formation of the gel layer obeys an interfacial dissolution-reprecipitation mechanism; under such a mechanism, the measurement of dissolved Si can be misleading since it has been

experimentally proposed that Si is dissolving and precipitating simultaneously. Thus, the measurement of dissolution rates of silicate glasses using Si as a tracer in various corrosion conditions remains a grand challenge. Boron has been extensively used as a surrogate tracer for quantifying the dissolution of glass given its role as a network former in borosilicate glass. However, the removal depth of boron is not equivalent to the actual thickness of dissolved glass. Thus, these factors accounted for in solution analysis of ion release can cause the discrepancy of dissolution rates between field and laboratory studies, which can easily be orders of magnitude [17]. Apart from the errors of solution analysis, such discrepancy of rates can also be a result of evolving surface area of glass when exposed to the aqueous solution as suggested by studies reported elsewhere [18, 19].

Dissolution rates determined by normalizing solution assays are associated with a series of assumptions including: 1) surface area remains unchanged during corrosion, i.e. normalization of ion concentration is achieved by dividing the $C_i$ (concentration of ion *i* in solution) over $x_i$ (mass ratio of element *i* in bulk glass) and SA/V (initial glass BET or geometric surface area to solution volume); 2) topographical and chemical characteristics between surfaces can be ignored, i.e. comfortable use of dissolution rates from corrosion of powder as compared to the morphological changes occurring on a monolithic surface; 3) corrosion of glass is homogeneous in spatial distribution, i.e. there is no preferred leaching or dissolution in spatial distribution. Given the fact that the kinetics and mechanisms of glass dissolution change over reaction time, these mechanistic assumptions can lead to a large uncertainty in the calculation of dissolution rates if they are based solely on solution analysis. Moreover, the formation of crystalline phases and gel zones complicates the experimentally measured dissolution rates. Thus, the error of

dissolution rate associated with solution assays can be ~ 60 % [15] of the reported value. As a result of all these factors combined, a legitimate question arises: how can the dissolution rate be measured while simultaneously obtaining mechanistic information with respect to the morphological evolution of glass surfaces?

Attempts have been made to best eliminate those assumptions and errors in the past decades [19, 20, 21]. Experimentalists have used the geometric surface area of glass powder to fit the dissolution data [19, 22], reducing the discrepancy of dissolution between laboratory and field study [19]. Glass fibers were used to avoid non-homogeneous corrosion in spatial distribution given their atomically smooth surface [23]. Different setups (e.g. single-pass flow cell) of corrosion experiments advanced the ability in probing long-term behavior or dissolution kinetics of glass [24, 25]. These advances and developments in our experimental techniques helped the glass corrosion community progress in the knowledge of glass dissolution kinetics, dissolution rate limiting factors, corrosion mechanisms, etc. More importantly, the link between dissolution rates, morphological evolution, and compositional evolution of glass surfaces is not clear. Needless to say, the dissolution of glass includes surface phenomena such as the morphological evolution of altered glass on the reaction front, gel zone formation [13], and surface roughening [23]. Pioneering works of Mellott and Pantano [23] tried to qualitatively and quantitatively relate the roughening of reacted glass surfaces to corrosion mechanisms (e.g. leaching of alkali, or dissolution of network former) using atomic force microscopy (AFM). Thus, those challenges [8, 9, 11, 12, 15, 21] and other studies [19, 23] in the glass corrosion community triggered the pursuit for a more substantial understanding of the relationship between kinetic factors in dissolution rate, compositional and morphological evolution of glass surfaces. However, a gap

remains unfilled in the measurement of dissolution rates from powder and in the mechanistic information on morphology from monoliths.

In this study, a novel method of measuring the dissolution rate that correlates the kinetic and mechanistic factors, compositional evolution, and morphological evolution of an aluminoborosilicate glass was developed using nanometer resolution AFM. In order to morphologically measure the dissolution rates of glass, a non-surface-destructive mask and exfoliation strategy was developed to artificially create a surface retreat between the corroded and masked glass melt surface. The developed polymeric composite mask highlights a superhydrophobicity and an easy exfoliation upon immersion in acetone. The non-surface-destructive feature of this strategy was validated by measuring the chemical composition, carbon bonding environment and equivalent RMS roughness of masked glass surface after exfoliation as a function of corrosion using X-ray photoelectron spectroscopy (XPS) and AFM, respectively. It was found that the masked glass surface remains identical to its pristine melt surface (both morphologically and compositionally) regardless of reaction time or pH. Clear and sharp surface retreats were observed among most of the AFM measurements performed on the interface between corroded and masked glass surfaces. The measured surface retreats at pH2, pH7, and pH10 were analyzed/fitted kinetically as a function of reaction time to obtain the dissolution rates, which provided insight into the corrosion mechanism as a function of pH and time. The methodology of measuring glass dissolution rates presented in this study is extensively discussed with respect to the validation of the mask-exfoliation technique developed and the comparability of morphological dissolution rates to dissolution rates from solution analysis. The kinetic and mechanistic information obtained from the surface retreat

measurement in combination with XPS studies on the corroded glass surfaces revealed the dissolution mechanism of the studied glass at three different pHs. The morphological evolution of corroded glass surfaces at nanometer resolution was visualized and quantified using AFM (both imaging and spectral analysis) as a function of reaction progress. It was found that the roughening behavior as well as the distribution of roughness is strongly connected to the dissolution of the glass surface. This study provides a novel method of measuring the dissolution rates of minerals, glasses and other types of materials. Most importantly, this study presented a preliminary investigation of the relationships between the kinetics/mechanisms of glass corrosion, and the compositional and morphological evolution of glass surfaces.

## 2. Materials and Methods

### 2.1 Characterization of bulk glass and preparation of melt surface

The glass used in this study was re-melted from commercially available fiber insulation aluminoborosilicate glass (courtesy of Johns Manville) in cullet form. The density of the glass (~ 2.54 ± 0.08 g/cm$^3$) was measured by triplicating Archimedes method on remelted glass coupons. The chemical composition of the bulk glass was determined by ICP-AES digestion (Optima 5300, Perkin-Elma) and was reported to be 17.1$Na_2O$-0.8$K_2O_3$-3.7MgO-8.6CaO-3.2$Al_2O_3$-7.3$B_2O_3$-59.3$SiO_2$ (mol%). The melting temperature ($T_m$~ 1250 $^oC$) and glass transition temperature ($T_g$~ 530 $^oC$) of the aluminoborosilicate glass cullet were determined by differential thermal analysis (SDT 2960, TA Instruments). For DTA measurement, glass cullet in the size of ~ 2 mm was heated in a Pt crucible from room temperature to 1300 °C under a nitrogen flow with a

heating rate of 10 °C/min. High purity alumina powder (trace-metal grade, Fisher Scientific) of equivalent mass was used as a reference in DTA measurement.

Aluminoborosilicate glass cullet was remelted in an alumina crucible at 1250 $^{o}$C in a resistance-heated furnace in order to make coupons of glass melt surface. The glass melt was kept at the melting temperature for 1 hour to allow homogenization and release of trapped air. Molten glass was poured onto a gridded stainless steel plate, cooled to room temperature, then annealed (530 $^{o}$C for 1 hour) and cooled overnight. The annealed glass was cut into approximately ~ 10 mm × 10 mm × 6 mm coupons. The resultant glass coupons are homogenous in physical appearance and show no sign of devitrification after annealing. All as-prepared glass melt surfaces are X-ray amorphous as characterized using an X-ray diffractometer (D2 Phaser, Bruker Inc., USA). All glass coupons were ultrasonicated in isopropanol for 15 mins, dried under a nitrogen gas flow and stored in vacuum desiccator prior to any test or characterization.

**2.2 Corrosion experiment**

Corrosion experiments were carried out under a static condition using HDPE wide mouth bottles (Nalgene®) at room temperature (~25 $^{o}$C). The surface area of the glass melt surfaces used in the corrosion experiment was calibrated using CAD SA database with an estimated error < 1%, and all the analytical work of surface area quantification was performed with ImageJ. To evaluate the ability to measure dissolution rates using AFM with mechanistically different conditions of corrosion, static corrosion experiments were carried out at a glass surface-area-to-solution volume (SA/V) ratio of 20 $m^{-1}$ in three imposed buffer solutions (pH2, pH7, and pH7). The pH 2 solutions were made by mixing KCl solution (0.2M) with HCl solution (0.2 M). The pH 7 solutions were made by slowly

adding THAM (*tris-hydroxymethyl aminomethane*) buffer (0.05 M) to dilute $HNO_3$ (0.0041 M) solution. The pH 10 solutions were made by slowly adding THAM (tris-hydroxymethyl aminomethane) buffer (0.05 M) to dilute LiOH (0.003 M) solution. Final adjustments of pH to the desired values were achieved by the addition of 1M HCl or 1 M LiOH solution with the assistance of a digital pH meter (Accumet AB15, Fisher Scientific). Glass coupons were placed in the bottom of HDPE bottles (filled with solutions) with the melt surface facing upward. The bottles were kept static, i.e. no stirring or flow. During corrosion experiments, the bottle caps were sealed with Parafilm®. The estimated retreat rate of the glass used in this study was: 1) 0.1 to 10 nm/hour at pH2; 2) 0.1 to 2 nm/hour at pH7, 90 $^{o}$C; 3) 1 to 10 nm/hr at pH10, 25 $^{o}$C. A measurable surface retreat would be on the order of nm to μm depending on the capabilities of the AFM used as well as the influence of surface roughness. Since the objective of this study was to develop a novel method of determining the dissolution rate of glasses, the surface retreat should be on the order of hundreds of nanometers within the given time of reaction. Thus, the time of reaction and sampling interval is as follows: 1) pH=2, 0 hours, 24 hours, 48 hours, 72 hours, 96 hours, 120 hours, 144 hours and 168 hours; 2) pH=7 (90 $^{o}$C), 0 hour, 24 hours, 36 hours, 48 hours, 60 hours, 72 hours, 84 hours and 96 hours; 3) pH=10, 0 hour, 2 hours, 4 hours, 8 hours, 12 hours, 16 hours, 20 hours, 24 hours, 120 hours, 168 hours, 216 hours, 240 hours and 360 hours. As an addition to the measurement of dissolution rate at longer terms of corrosion, glass coupons reacted for 480 hours, 720 hours and 960 hours were introduced into each pH test group.

## 2.3 Materials of masking and strategy of post-reaction exfoliation

In order to measure the dissolution rate, a strategy of mask and exfoliation was deployed. Figure III.1 illustrates the experimental strategy.

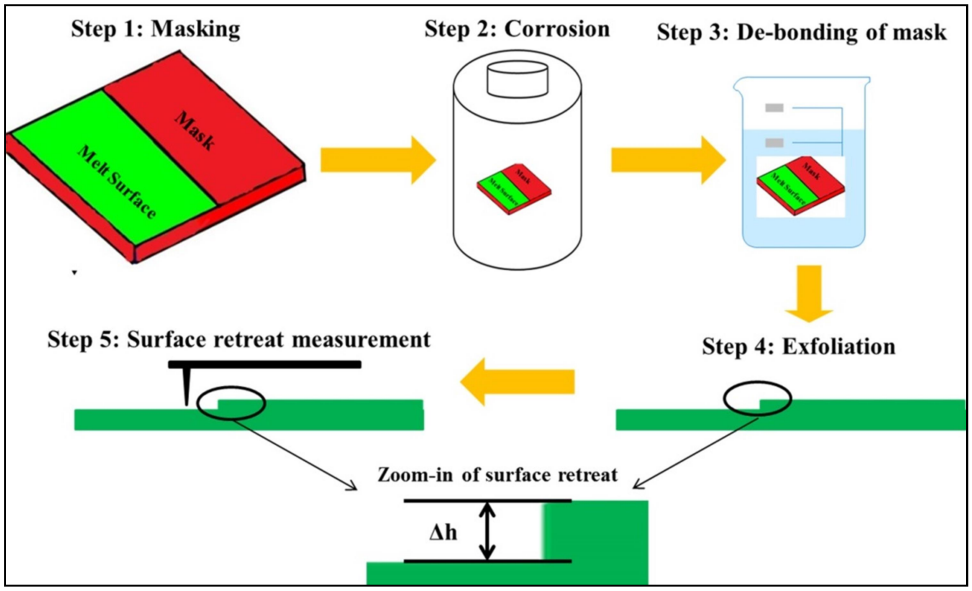


Figure III.1 Schematic of experimental strategy upon morphological measurement of corrosion rate.

A mask is applied to the melt surface of the glass coupon, and the mask prevents the reactions between masked glass melt surface and solution. The mask is removed after reaction in order to measure the surface retreat between the reacted surface and the masked surface. In order to successfully apply this strategy, the material of masking has to be: a) hydrophobic to avoid corrosion at the mask-glass interface; b) sufficiently dense to prevent the diffusion of aqueous species through the mask material; c) fully removable from glass surface without mechanical or chemical modification of pristine glass surface. However, no proven materials have been reported to be suitable for strategy used in this study. Thus, a novel polymeric composite mask was developed in this study to meet these requirements.

The polymeric composite mask is a mixture of uncured silicone and liquid cyanoacrylate with a volume ratio of ($V_{silicone}/V_{acrylate}$ = 10:1). Prior to application to the glass melt surface, the composite was synthesized by slowly stirring cyanoacrylate into uncured silicone in a 40 $^{o}$C water bath. The typical incorporation rate of cyanoacrylate was 1 mL/min. The mixture of polymer composite was then cooled to room temperature before being applied onto the melt surface of the glass coupons. The mask was cured for 24 hours in a vacuum dessiccator to fully develop the chemical resistance prior to applying the mask onto the glass melt surface. After reaction, the glass coupon was washed in isopropanol, and soaked in acetone for 10 mins. The mask could then be peeled off using a Teflon tweezer after immersion in acetone. The exfoliated glass coupon was washed in isopropanol/DI-water, dried in nitrogen flow, and stored in vacuum desiccator prior to any characterization.

Cyanoacrylate was desirable to silicone for several reasons. While silicone is dense in structure and has often been used as a water-proof sealant in numerous applications, the full removal of silicone cannot be achieved with mechanical method (e.g., scratching) or chemical methods (e.g., silicone softener) alone. This is because cured silicone is not fully dissolvable in any solvent, and only can be softened with an aromatic hydrocarbon or mineral oil. However, those types of chemicals only partially remove silicone from a surface, and in the process, introduce large amount of carbon and silicon contamination to surfaces of interest. Cyanoacrylate is hydrophilic and can be easily dissolved with acetone, ketone or -other organic solvents. An illustration of the exfoliation mechanism of this polymer composite is shown in Figure III.2

.

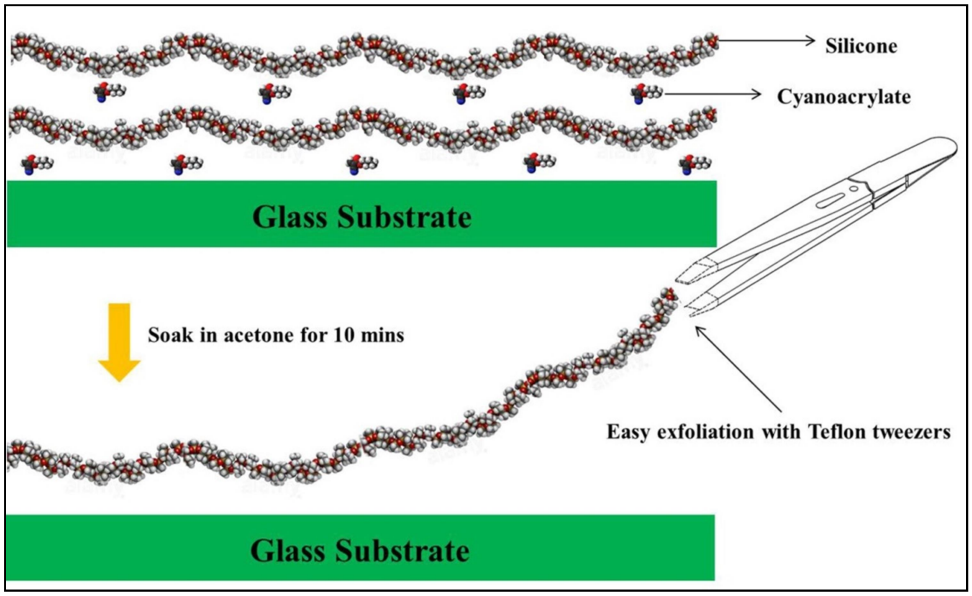


Figure III.2 Animation of exfoliating the polymeric composite mask from the glass substrate.

To prove that the composite mask can be fully removed by this method, quantitative X-ray photoelectron spectroscopy (XPS) was performed on the masked area of glass coupon (reacted & non-reacted) after exfoliation. A comparison group of cured polymeric composite mask was characterized using XPS to understand the bonding environment of the polymeric mask. AFM was performed on post-exfoliation samples (reacted or non-reacted) to confirm the hydrophobicity of the polymeric composite mask (e.g. no change in surface morphology of masked area). Exfoliated samples were stored and transported by a vacuum desiccator in order to avoid any effect of humidity or contamination from the atmosphere.

### 2.4 X-ray photoelectron spectroscopy

The chemical composition (outermost ~ 6 to 8 nm) as well as the local chemical environment of corroded glass surfaces and masked glass surfaces after exfoliation was analyzed with a PHI Quantera scanning X-ray microprobe (XPS). Prior to XPS analysis,

the samples were cleaned in ultra-violet ozone cleaner for 20 mins and transferred to introduction chamber right away. Samples were placed in introduction chamber for ~24 hours to avoid pressure fluctuation upon transfer to analysis chamber (pressure of analysis chamber is below ~ $1e^{-9}$ torr). The XPS data sets were collected with Al Kα X-rays (non-monochromatic, beam size=100 μm) at 20 mA anode current, with an electron energy of 1486 eV and a step size of ~0.1 eV. Survey scans were performed with a pass energy of 140 eV to gain qualitative information such as peak identification and peak position. Peaks identified in all survey scans were used to adjust high-resolution scan binding energy range, pass energy (26 eV) and dwell time. The beam dwell time for each high-resolution scan peak was adjusted (~500 ms/step) to yield a signal-to-noise ratio of >100:1 with the exception of B1s & Mg2s peaks, which were adjusted to yield a signal-to-noise ratio of >50:1. The analyzed area was ~1 to 2 mm in diameter. Adventitious alkyl C1s peak located at ~ 284.6 eV was used to calibrate the position of other acquired XPS spectrum.

Quantification of surface chemical compositions was performed for all samples from high-resolution scans including Si2p, Al2p, B1s, Mg2s, Ca2p, Na1s, K2p and O1s peaks. Relative sensitivity factors of all elements ($RSF_{Si2p}$=1, $RSF_{Al2p}$=0.5, $RSF_{B1s}$=0.4, $RSF_{Mg2s}$=0.5, $RSF_{Ca2p}$=5.3, $RSF_{Na1s}$=3.0, $RSF_{K2p}$=3.2 and $RSF_{O1s}$=1.8) were derived from high-resolution XPS scans of fresh air-fractured pristine aluminoborosilicate glass surface, assuming that the ISG glass fracture surface was identical to the bulk glass composition obtained from ICP-AES.

## 2.5 Atomic force microscopy

Surface retreat between the corroded glass surfaces and masked glass surfaces was imaged and quantified using a Bruker Dimension Icon® multimode atomic force microscope (AFM) equipped with $Ar/N_2$ gas floating table in Tapping Mode®.

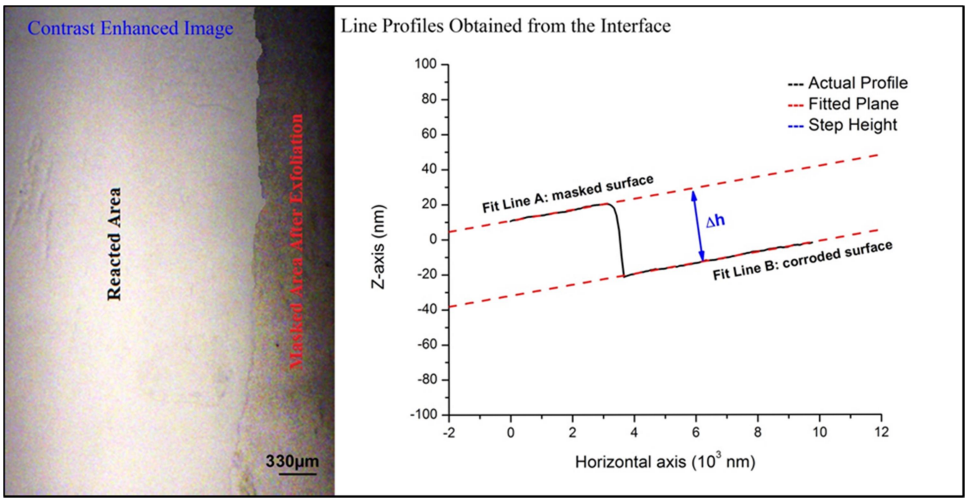


Figure III.3 Image (left) of the interface between reacted area and masked area (post-exfoliation) as obtained from optics attached to AFM, the contrast of image was enhanced by PhotoShop®; plot (right) of the line profile of the reacted/masked glass interface subtracted from AFM image and its corresponding fitting.

Antimony doped silicon probes (Bruker TESP, cantilever length of 125 μm) with a nominal tip radius of curvature of 8nm, the nominal spring constant of 42 N/m and resonance frequency range of ~230-410 KHz was used for all measurements. Images were taken with a scanning rate of 1.0 Hz and resolution of 256 pixels × 256 pixels. Qualitative tip size and shape calibration was performed periodically during measurements using a commercially available standard (Ted Pella Product No. TCI-BudgetSensor TipCheck). Five 20 μm X 20 μm scans were taken of each sample at different locations at the interface between corroded and masked glass surface to ensure a large-scale spatial homogeneity of surface morphology and surface retreat. The interface between corroded and masked glass surface can be identified under the optics attached to

Bruker Icon AFM (e.g. shown in Figure III.3 as a contrast-enhanced image). To accurately measure the surface retreat, a wafer standard with 20 nm high pillars (Ted Pella Product No. TCI-BudgetSensor HS-20MG) was used to quantify the error of the height measurement (~ 0.2 nm) as a function of number of scans performed (e.g. usually, a new AFM tip is used for only 10 scans). All analyses on the collected AFM images were performed on Nanoscope Analysis platform (version 1.50 build R1Sr3.96576). Line-by-line flattening and 1$^{st}$ order plane fitting was performed on each image prior to analysis to remove any artifacts caused by the curvature of the piezoelectric material, misalignment of sample, thermal drift, background vibration noise or lateral forces. Flattening removed vertical offsets between scan lines through calculation of a least-squared polynomial fit for a scan line followed by subtraction of the polynomial fit from the original scan line. First order plane fitting calculates a first-order fit to the image in the *x*- and *y*-directions and subtracts the linear fit from the image, removing tilt and misalignment of the sample. Ten line profiles were selected from each image to obtain an average surface retreat value, and a standard deviation (STD) of the surface retreat was calculated for each sample (~ 50 line profiles) as root-mean-square height deviation from the mean value.

In order to monitor the morphological evolution of the glass surfaces as a function of corrosion, five 8 μm X 8 μm scans were performed on different spots of the reacted glass surfaces (using the same imaging parameters as the imaging of surface retreat). Two-dimensional isotropic power spectral density (PSD) profiles were obtained from each image using a fast Fourier transform, as discussed in [26]. For each sample, the representative PSD profile was a mathematical average of five images on different spots.

The PSD profiles were fitted using the k-correlation model (in the frequency region from 0.125 to 6.125 $\mu m^{-1}$) and the fractal model (6.25 to 16 $\mu m^{-1}$) to obtain equivalent RMS roughness, correlation length and Hurst exponent. All algorithms associated with PSD analysis were reported and discussed in detail in Gong, et. al [26]. The equivalent RMS, correlation length and Hurst exponent was measured as a function of corrosion in order to: a) quantitatively investigate the morphological evolution of glass surfaces as a function of corrosion; b) investigate the spatial distribution homogeneity of roughness at its corresponding spatial wavelength; c) make sure the masked glass surface (post exfoliation) was not reacting with the solution environment, i.e. make sure the surface roughness of masked glass surface remain unchanged with reaction time.

**2.6 Recession rate measurement and error analysis**

As shown in Figure III.2, a polymeric mask was applied to half of the glass melt surface to prevent the reaction between the masked glass surface and solution environment. The portion of glass exposed to solution dissolves, and the surface retreats over the designated time of reaction. To obtain the surface retreat $\Delta h$ from line profiles, two linear fits was performed separately on the portions of line profile from both masked and corroded glass surface (e.g. shown in Figure III.3). $\Delta h$ is the distance between the two linear fits A and B.

In order to mathematically calculate the distance between two linear fits, the two fitted linear lines have to be perfectly parallel. Thus, a strategy of imposing slope values has been utilized: line A/B was fitted to have a slope value, and this slope value was used as the constraint/slope of fitting line B/A. In both linear fits, a requirement of $R^2 > 0.99$ was followed to minimize the statistical errors associated with the fitting process. As

shown in Figure 3, linear fits of the line profile of both masked and corroded glass surfaces yielded $R^2 > 0.99$ (Line A: 0.99341; Line B: 0.99893). The line with the higher fitted $R^2$ value, in this case line B, was used as the slope constraints for the fitting of line A. Eventually, Δh can be calculated as the difference between intercept values of both linear fits. The errors of Δh were measured as a root-mean-square surface retreat (or standard deviation of surface retreat) as:

$$STD = \sqrt{\left(\frac{(\Delta h_1 - \Delta h_{avg})^2 + (\Delta h_2 - \Delta h_{avg})^2 + \cdots + (\Delta h_{50} - \Delta h_{avg})^2}{50}\right)} \quad (1)$$

where 50 is the number of line fittings performed on each sample in this study. Surface retreat Δh can be converted to a dissolution rate by [19]:

$$r = \frac{\rho * \Delta h}{\Delta t} \quad (2)$$

where r [g/(m$^2$d)] is the dissolution rate, ρ (g/m$^3$) is the density of the glass, Δh (nm) is the surface retreat, and Δt (days) is the time of reaction. This conversion of the recession rate (Δh/Δt, nm/day) allows comparisons between the dissolution rates measured in this study and the dissolution rate of other glasses reported in literature. To quantify the error of the dissolution rate obtained from AFM, rules for product and quotient terms were used:

$$error\ of\ rate\ =\ rate * \sqrt{\left(\frac{x}{\rho_{avg}}\right)^2 + \left(\frac{y}{\Delta h_{final}}\right)^2 + \left(\frac{z}{\Delta t_{final}}\right)^2} \quad (3)$$

where x, y, and z is the uncertainty of $\rho_{avg}$ (density of bulk glass), $\Delta h_{final}$ (final value of surface retreat), and $\Delta t_{final}$ (final value of reaction time), respectively. Uncertainty x is the error of the density measurement 0.08 g/cm$^3$, uncertainty y is equivalent to the RMS roughness of corroded glass surface and uncertainty z is estimated as 120 seconds. It is

worth noting that the timing uncertainty is composed of: a) retrieving the sample from HDPE bottles after corrosion experiment; b) rinsing the sample surface with isopropanol/DI-water; c) transferring the sample to vacuum desiccator. To correlate the dissolution rate obtained from solution analysis with the recession rate, the following equation is given [27]:

$$r = \frac{\rho * \Delta h}{\Delta t} = \frac{NL_i}{\Delta t} = \frac{C_i}{x_i * \left(\frac{SA}{V}\right)} \quad (4)$$

where $NL_i$ is the normalized loss ($g/m^2$) of element *i*, $C_i$ is the concentration of element *i* in solution ($g/m^3$), $x_i$ is the weight percent of element *i* in the bulk glass and SA/V is the ratio of the glass surface area to solution volume ($m^{-1}$). Rearrangement of equation (4) allows the conversion between concentration $C_i$ and surface retreat $\Delta h$ [19]:

$$C_i = \rho \Delta h x_i \left(\frac{SA}{V}\right) \quad (5)$$

## 3. Results

### 3.1 Evaluation of experimental methods, strategies and hypotheses

Differential thermal analysis was used to determine the glass transition temperature of the bulk glass. The glass transition temperature $T_g$ was determined to be ~ 530 $^oC$. A broad peak occurred at ~ 1050 $^oC$, which most likely corresponded to the crystallization peak reported for different glass compositions, within the aluminoborosilicate glass family [28]. Cullets of this aluminoborosilicate were remelted at ~1250 $^oC$ for better homogenization. The glass melts were then poured onto a stainless steel plate, and cooled in air prior to annealing at 530 $^oC$ for 1 hour. The annealing of glass at its transition temperature reduces the thermal stress caused by rapid air quench.

The as-prepared glass melt surface (coupon) was transparent by visual inspection and was confirmed to be X-ray amorphous.

The chemical composition of the outermost surface (~ 8 nm) of glass melt surface was determined as 6.6Na, 2.1K, 2.1Mg, 4.1Ca, 2.4Al, 1.5B, 17.2Si, 64.0O (atm%) using XPS. Compared to the composition of bulk glass, a depletion of ~ 4.6 atm% in Na and ~ 3.3 atm% in B concentration was observed. The Ca, Mg and K concentration of pristine glass melt surface show an increment < 1.6 atm% comparing to the bulk glass composition. Concentrations of other elements within the glass remains the same (as-measured error of XPS quantification: Na ± 0.5 atm%, K ± 0.1 atm%, Mg ± 0.2 atm%, Ca ± 0.3 atm%, Al ± 0.2 atm%, B ± 0.4 atm%, Si ± 0.7 atm% and O ± 0.7 atm%). Only minor deviations were observed between the composition of glass melt surfaces and the bulk glass composition. The equivalent RMS of pristine glass melt surface is 1.8 nm as obtained from fittings of PSD profiles (2D-FFT of AFM image) using the k-correlation model.

To evaluate the ability to fully remove, as well as the inertness of the polymeric composite mask, C1s XPS spectra of the cured polymeric mask, masked (post-exfoliation) and reacted glass surfaces were studied (e.g. Figure III.4a & b). Figure III.4a is the representative C1s XPS spectra of the polymeric mask, and the masked glass surfaces (post exfoliation), which have been reacted in pH=2, pH=7 and pH=10 for up to 960 hours. The C1s peak of the polymeric mask was resolved with three possible characteristic peaks at 284.6 eV, 285.3 eV and 287.2 eV (standard deviation of peak position is 0.1 eV).

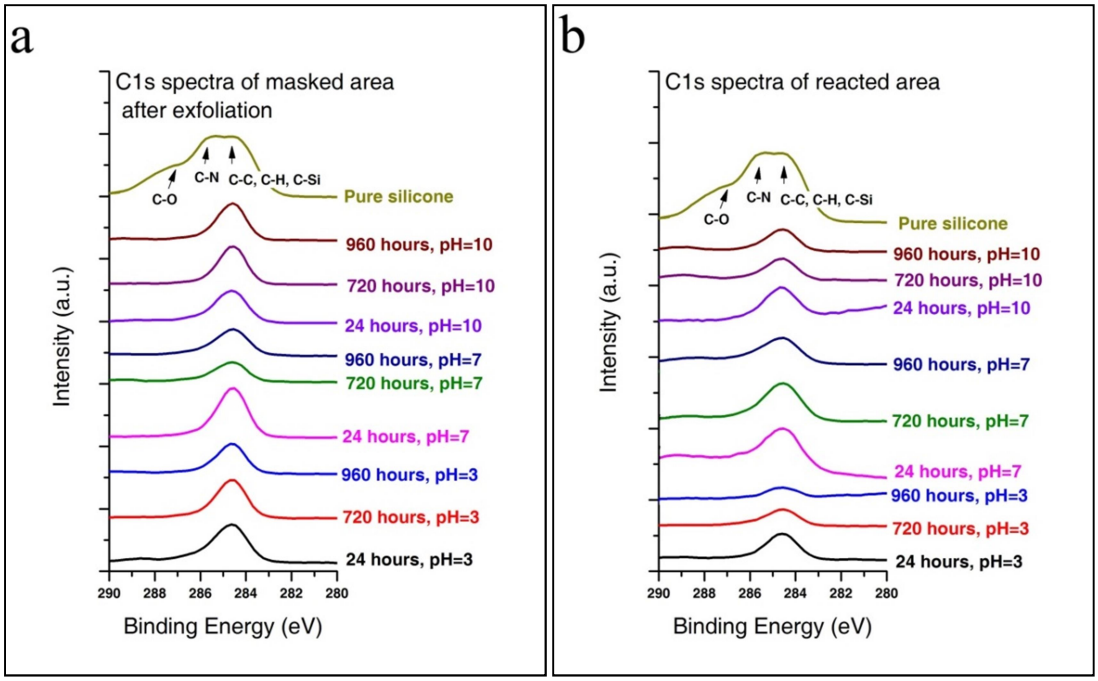


Figure III.4 C1s spectra of a) masked glass surface (post exfoliation) and b) reacted glass surface.

Of all the measured surfaces (only selected C1s peaks were shown), the C1s spectra of masked glass surfaces (post exfoliation) are symmetric C1s peaks located at 284.6 eV. Figure III.4b shows the selected C1s spectra of glass surfaces reacted at pH2, pH7 and pH10. Similarly, the C1s spectra are symmetric and correspond to alkyl carbon species regardless of pH and reaction time. The C1s spectra on reacted glass surfaces are collected to investigate the possible dissolution or leaching of the polymeric mask and its re-deposition onto reacted areas.

In order to evaluate the stoichiometric evolution of masked glass surface (post exfoliation), XPS high resolution scans were used to quantitatively characterize the chemical environment and composition. The composition of masked glass surface reacted in pH2, pH7 and pH10 solution (for up to 960 hours) shows minor variations $\leq$ 1.0 atm% compared to the pristine melt surface, and the variations in concentration are within the

standard error of quantification for each element measured. Regardless of reaction time, the peak position and FWHM of each measured spectrum are shown in Table 4.1.

Table 4.1 Summary of the Peak Positions and FWHMs of the Masked Glass Surface (after exfoliation), No Variation of Values were Observed as a Function of Reaction Time

| Peak | Position (eV) | FWHM (eV) |
|---|---|---|
| O1s | ~531.6 to 531.8 | ~2.1 to 2.2 |
| $Ca2p_{1/2}$ | ~350.8 to 350.9 | ~1.7 |
| $Cap2p_{3/2}$ | ~347.1 to 347.2 | ~1.7 |
| Na1s | ~1071.2 to 1071.4 | ~1.9 to 2.1 |
| $K2p_{1/2}$ | ~296.1 | ~1.4 |
| $K2p_{3/2}$ | ~296.3 | ~1.6 |
| Mg2s | ~89.1 to 89.3 | ~2.0 to 2.3 |
| Al2p | ~74.3 to 74.4 | ~1.7 |
| B1s | ~192.3 | ~1.7 |
| Si2p | ~102.1 to 102.5 | ~2.0 |

For XPS quantification, all the measured peaks are symmetric in peak shape including split peaks (e.g. $Ca2p_{1/2}$ & $Ca2p_{3/2}$ peaks). All results of peak position were within the error of standardization (0.1 eV for FWHM and peak position), and no changes in peak position and FWHM as a function of reaction time were concluded from these results. The equivalent RMS roughness of the masked melt surface (post exfoliation) as a function of reaction time was also measured. The equivalent RMS roughness of the glass surfaces reacted at pH2, pH7 and pH10 is approximately 1.7 nm to 1.9 nm, and remains within the error of $\leq$ 0.2 nm (as the standard error of fittings of every 5 PSD profiles) throughout the experiment.

### 3.2 Surface retreat rates and dissolution rates

In order to accurately quantify the surface retreat as a function of reaction time, the effect of wearing on the AFM tip with respect to the accuracy of a height measurement must be taken into account. Thus, a height-standard wafer with 20 nm high pillars (deposited by soft lithography) was measured as a function of scanning cycle, and same scanning parameters which were used in the surface retreat measured were also applied to the measurement of the height standard.

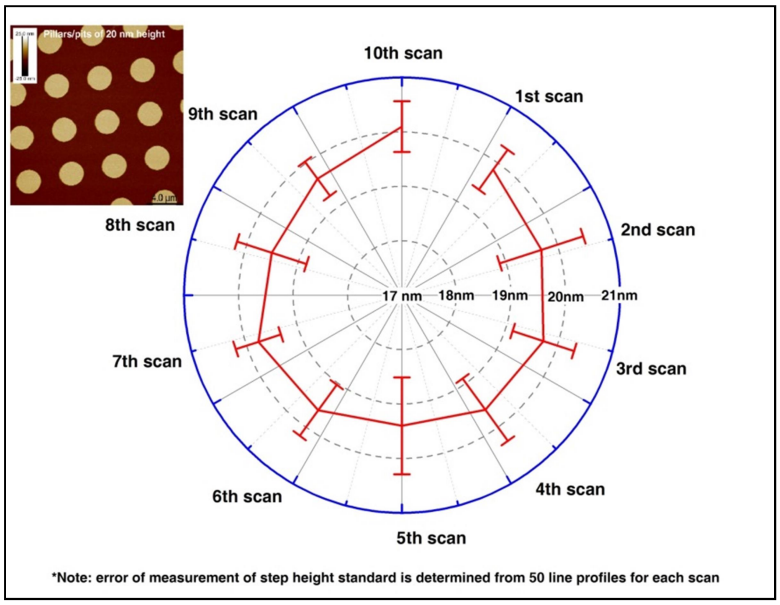


Figure III.5 Measured value of height standard as a function of scanning cycle; inset is the 20 μm X 20 μm AFM image of the height standard in the shape of cylindrical pillar (colored vertical scale: -25 to 25 nm).

Scanning parameters were kept the same given the fact that sampling interval, scanning rate, drive frequency and amplitude have an effect on the quantification of topography [26, 29]. Figure III.5 shows the measured height value of the pillars as a function of scanning cycle performed, and the inset is the 20 μm × 20 μm AFM image of the

height standard. For the quantification, the height value is defined as the distance between the fitted planes of the top surface of the pillar and the wafer substrate. Each height value for a particular scanning cycle was obtained from sets of linear fits of line profiles subtracted from 20 different spots on the AFM image. The average height of the pillars and the standard error (measured from 20 different spots for each scanning cycle, 200 spots in total) was plotted against the scanning cycle in a clockwise fashion. As shown in the inset of Figure III.5, the topography of the standard features a series of cylindrical pillars with a similar geometry (by visual inspection). Within 10 cycles of scan performed, the height value remains stable in the range of 19.4 to 20.1 nm with an error $\leq$ 1.0% in each cycle. The measured height values were comparable to the manufacturer's stated value of 19.6 nm (error is ± 2.0%). It needs to be pointed out that the interface between the substrate and the pillar was sharp during the 10 performed scanning cycles. An AFM artifact of worn or dull tip often is reflected by a blunt interface [29] when measuring the height of features. Thus, the measurement of surface retreat did not affect the sharpness of the AFM tip.

Figure III.6a , b and c show the representative AFM images and corresponding fit of surface retreat from glass coupons reacted in pH2 (120 hours, 25 $^{o}$C), pH7 (96 hours, 90 $^{o}$C) and pH10 (24 hours, 25 $^{o}$C) , respectively. As shown in Figure 6a, the masked glass surface (post exfoliation) appears to be smooth and featureless after being reacted in pH2. Throughout the experiment and regardless of pH or reaction time (e.g. Figure III.6), the masked glass surface appears to be smooth as previously quantified by the equivalent RMS (~ 1.7 to 1.9 nm).

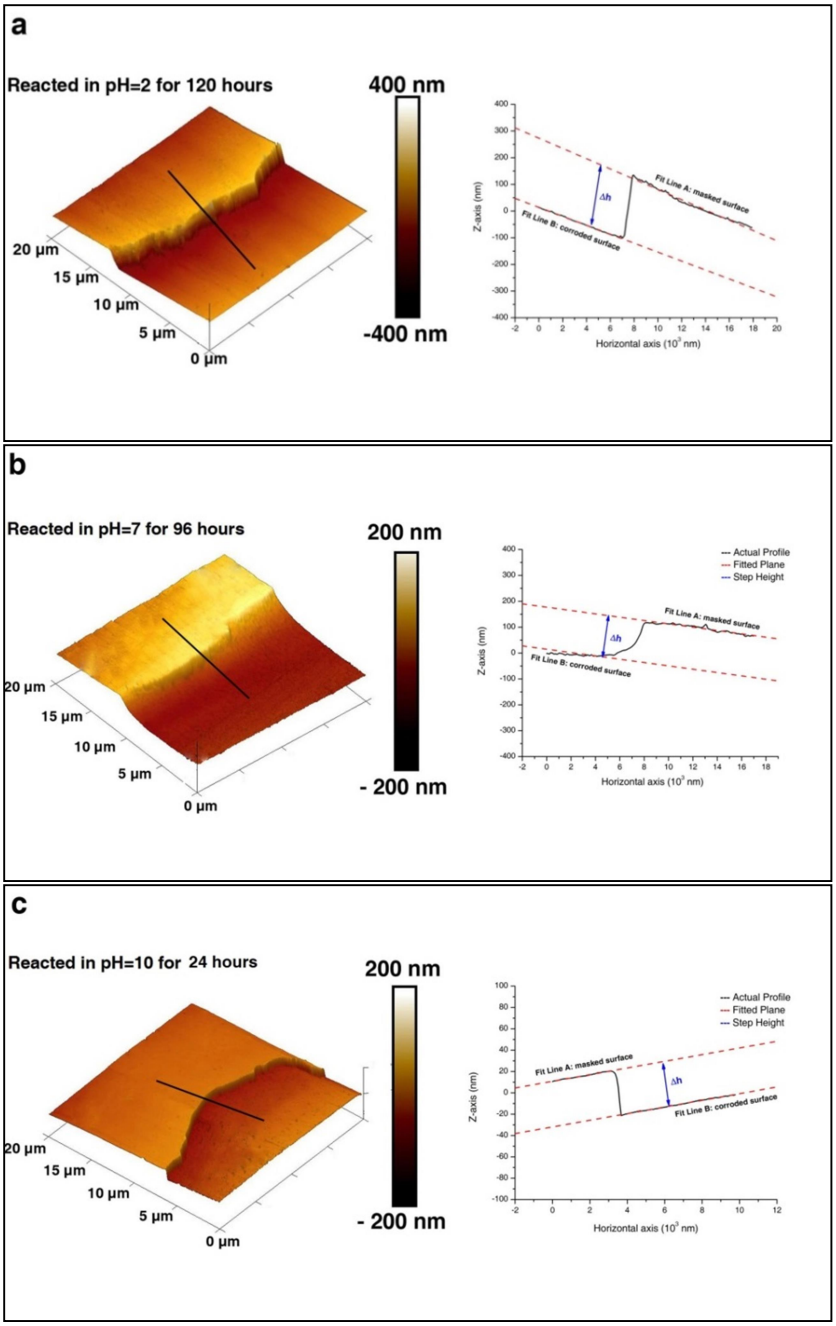


Figure III.6 Representative AFM image and corresponding fitting of surface retreat of glass coupon reacted at a) pH=2, 25 $^{o}$C for 120 hours, b) pH=7, 90 $^{o}$C for 96 hours and c) pH=10, 25 $^{o}$C for 24 hours.

The horizontal interface between the masked and reacted glass surface was rough in microscale. The fitting of corresponding line profile was achieved by two parallel linear fits on masked and reacted glass surfaces, and the distance between the two parallel

lines was the surface retreat Δh ≈ 135.5 nm (e.g. Figure III.6a). Similarly, the masked glass surface shown in Figure III.6b was featureless and smooth. The surface retreat of glass coupon reacted in pH7 for 96 hours was determined as ~ 130.7 nm. However, the vertical feature of the surface retreat was not sharp for this particular AFM image (e.g. Figure III.6b), and appears to be a curved surface instead of being flat. In this study, most of the measured surface retreats were sharp and flat in the vertical direction. For the glass surface reacted in pH10 for 24 hours (e.g. Figure III.6c), the surface retreat was determined to be ~ 41.1 nm in the particularly shown image.

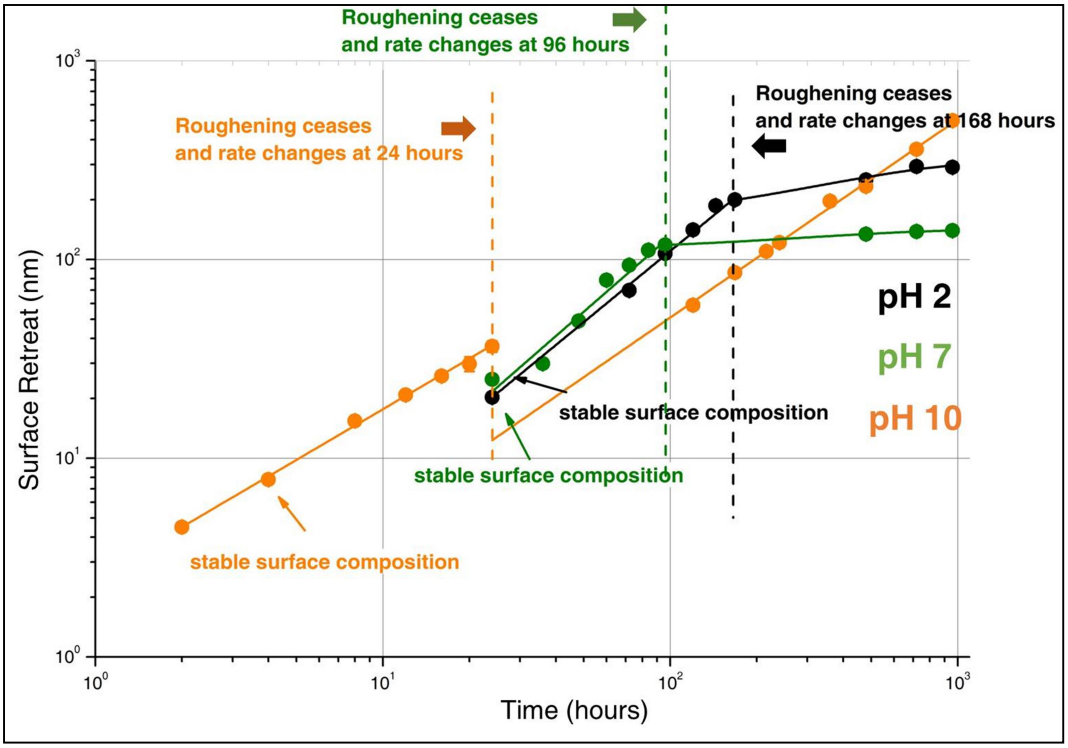


Figure III.7 Surface retreat of glass coupon reacted in pH=2, pH=7, and pH=10 as a function of reaction time.

The surface retreats of all reacted glass coupons were successfully imaged and quantified throughout the experimental, and were plotted against the reaction time as shown in Figure III.7. The standard error of surface retreats was reduced by spatially

averaging the measurement from 5 distinct spots over the glass coupon. Additionally, the bias in sampling was avoided by the spatially averaged measurement. The center and radius of the spheres in Figure III.7 was the value of surface retreat and standard error, respectively; lines were the fits of all measured data points with the allowance of standard error. As shown in Figure III.7, the standard error associated with each surface retreat value was negligible. The negligible error of the measured values of surface retreat represents a homogeneous spatial distribution of the surface retreat on the glass coupons. In order to select a proper fitting method of the curves shown in Figure III.7, the kinetics of surface retreat rate was evaluated using log(Δh) vs log(t) plot [30]. It was found that: a) the surface retreat showed a kinetic change after 168 hours, 96 hours and 24 hours for pH2, pH7 and pH10, respectively; b) the surface retreat was best fitted using linear regression prior to the change of kinetic and was appropriately fitted using non-linear regressions (Fick's rate law or solution chemistry law) after the change of kinetic occurs. Generally, the fittings of surface retreat rate applied in this study satisfied $R^2$>0.97. The standard error of obtained surface retreat rates was better than 10%.

The obtained surface retreat rates as well as their corresponding rate laws were shown in Table 4.2. Under the linear regression, the surface retreat rate of glass coupon as a function of pH showed a trend that recession rate of pH10 > pH7 > pH2. A similar trend of surface retreat rate versus pH was observed when the reaction was controlled by the non-linear regressions. Using the calculation described by equation (2) and (3), the dissolution rates of the studied glass were presented in Table 4.3.

Table 4.2 Summary of Surface Retreat Rates and their Corresponding Fitting Rate Laws at Different pHs

| Solution environment | Short Term | | Long Term | |
|---|---|---|---|---|
| | Reccession Rate | Duration (hours)/ Fit | Recession Rate | End of reaction (hours)/ Fit |
| pH=2, buffered | 29.5 nm/day | 168/ Linear | 1.0 nm/day | 960/ Diffusion |
| pH=7, buffered | 33.2 nm/day | 96/ Linear | 2.3 nm/day | 960/ Back-forward |
| pH=10, buffered | 38.0 nm/day | 24/ Linear | 12.1 nm/day | 960/ Linear |

Table 4.3 Summary of Dissolution Rates and their Corresponding Fitting Rate Law at Different pHs

| Solution environment | Region 1 | | Region 2 | |
|---|---|---|---|---|
| | Dissolution rate [g/($m_2$d)] | Duration (hours)/ Fit | Dissolution rate [g/($m_2$d)] | End of reaction (hours)/ Fit |
| pH=2, buffered | $7.49\pm0.44*10^{-2}$ | 168/ Linear | $2.54\pm0.12*10^{-3}$ | 960/ Diffusion |
| pH=7, buffered | $8.43\pm1.08*10^{-2}$ | 96/ Linear | $5.84\pm0.72*10^{-3}$ | 960/ Back-forward |
| pH=10, buffered | $9.65\pm2.83*10^{-2}$ | 24/ Linear | $3.07\pm0.55*10^{-2}$ | 960/ Linear |

To compare the obtained initial dissolution rates (surface controlled rate of pH=2, pH=7, and pH=10) with the initial dissolution rates reported by various literature resources [5, 6, 25, 31, 32, 33, 34, 35, 36, 37, 38, 39, 40, 41, 42, 43, 44, 45, 46, 47, 48, 49, 50, 51, 52, 53, 54, 55, 56, 57, 58, 59, 60, 61, 62, 63, 64, 65, 66, 67], the dissolution rates (either from this study or literature) were plotted as a function of pH in scattered points as shown in Figure III.8. The black and blue data points represent dissolution rates from experiment at 25 $^{o}$C and 90 $^{o}$C, respectively; red stars are the dissolution rates from this study; and, the open star colored in blue is from the interferometry work of Icenhower on SON68 glass (French nuclear waste form reference glass) [19]. Overall, the dissolution rates obtained from this study fitted into the range of the reported dissolution rates in literature. The initial dissolution rates obtained from this study (as red stars) were either slower (pH2 and 7) or close (pH7 and 10) to the

literature values at the corresponding pH. With respect to the pH effect on dissolution rate, the dissolution rate decreases from pH~-1 to pH~6, and increases from pH ~6 to pH~14 as reported by the literature. Particularly, the initial dissolution rate of pH2, pH7 and pH10 experiment was slower compared to the results reported by Icenhower [19] (pH=7.57, Si concentration is 0 ppm, 90 $^{o}$C), who used the interferometry to measure the surface retreat on SON 68 glass (Figure III.8, open blue star).

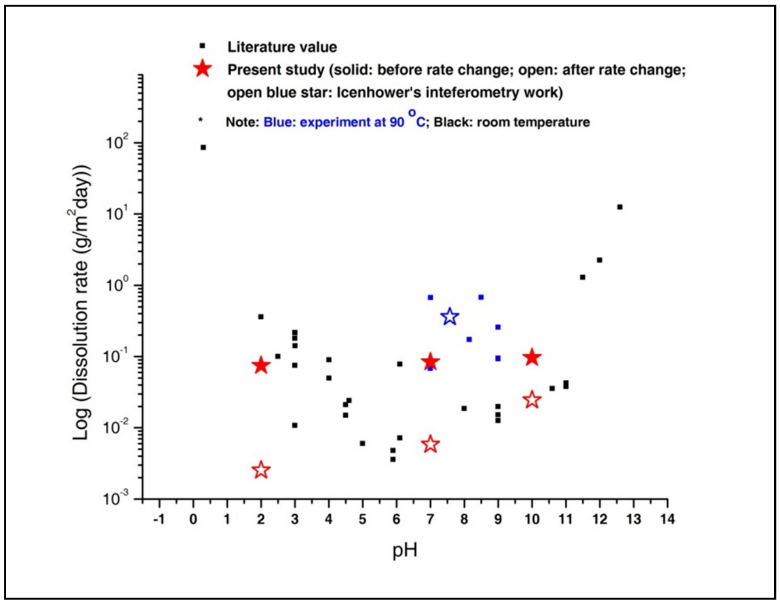


Figure III.8 Comparison of dissolution rates (star) obtained in this study comparing to literature values (solid cube) obtained from glasses of similar composition; dissolution rates were plotted as a function of pH.

### 3.3 Compositional and topographical evolution of reacted glass surfaces

Figure III.9 shows the composition of reacted glass surfaces as a function of reaction time. For glass coupons reacted in pH2, the composition (upper row in Figure III.9) shows a trend of Si enrichment (standard error of each element is Na ± 0.5 atm%, K ± 0.1 atm%, Mg ± 0.2 atm%, Ca ± 0.3 atm%, Al ± 0.2 atm%, B ± 0.4 atm%, Si ± 0.7

atm% and O ± 0.7 atm%). After 24 hours of reaction in pH2 solution, the Si concentration increased from 17.2 (pristine melt surface) to 27.2 atm%.

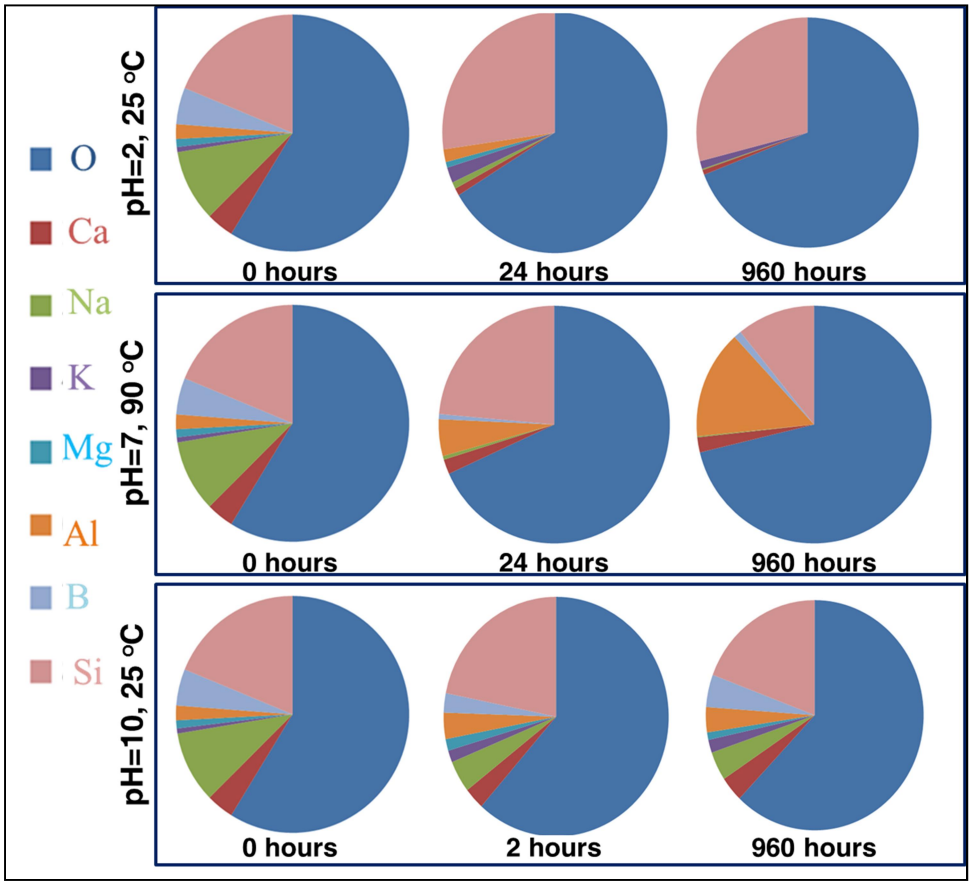


Figure III.9 Composition of reacted glass surface as a function of reaction time; upper row is from the glass coupon reacted at pH=2, 25 °C; middle row is from the glass reacted at pH=7, 90 °C; bottom row is from the glass coupon reacted at pH=10, 25 °C.

The Si concentration remains ~27.0 atm% from 24 hours to 144 hours of reaction. The Si concentration on the surface of pH2 experiment reached 29.6 atm% after 168 hours of reaction, and remained at 29.0 ± 0.3 atm% till the end of the experiment. With respect to the concentration of modifier ions such as Na, Mg and Ca, they were depleted from the surface (concentration < 1.0 atm%). The concentration of K did not reach ~1.0 atm % after 120 hours of reaction. Boron was completely depleted from the

outermost surface (~ 8 nm in depth) after 24 hours of reaction in pH2 solution. However, the depletion of Al was not observed until the glass coupon has been reacted for 960 hours, and the concentration of Al reaches < 1.0 atm% after 120 hours of reaction. After the glass has been reacted in pH2 for 24 hours, the measured surface retreat was ~ 20 nm; and the surface retreat value of ~ 100 nm was reached after 96 hours. As shown in Figure III.9 (upper row), the most significant compositional evolution occurred on the glass surface (reacted at pH=2, 25 $^{o}$C) was the depletion of Na and enrichment of Si. There was no observable change in network former concentration until 168 hours. The glass coupons reacted at pH7 showed that K and Mg were depleted from the outmost glass surface after 24 hours of reaction. Leaching of Na modifier ion was observed, and the Na concentration decreased to ~0.5 atm% after 24 hours of reaction. The Na concentration remained at ~ 0.5 atm% till the end of the experiment. Throughout the experiment the concentration of Ca on the surface remained ~ 2.0 ± 0.3 atm % , which was close to the concentration of Ca in the bulk glass (2.8 atm%). The B was not completely depleted from the surface until 84 hours of reaction. The network former Si was dissolved from the surface as indicated by Figure III.9 (middle row), and the decrease of Si concentration occurred after 96 hours of reaction (24.7 atm% at 96 hours, 24.4 atm% at 480 hours, 16.5 atm% at 720 hours and 10.8 atm% at 960 hours). The enrichment of Al was accompanied by the decrease of Si concentration, which also occurred after 96 hours of reaction. The Al concentration increased from 5.1 atm% at 96 hours to 7.4 atm% at 480 hours, and eventually increased to 14.8 atm% after 960 hours of reaction. As shown in Figure III.9, the most distinguishable event occurs on the glass surface (reacted at pH7, 90 $^{o}$C) was the depletion of K, Mg and Na, leaching of Si, and enrichment of Al. The surface retreat

increased from ~ 20 nm at 24 hours to ~ 100 nm at 84 hours. There was no drastic change in the concentration of network former from 24 hours to 96 hours. The compositional evolution of glass surfaces reacted at pH10 was not noticeable throughout the reaction (from 2 hours to 980 hours) as representatively shown in Figure III.9 (lower row). The composition of the surface (after 2 hours of reaction) showed a minor leaching of Ca, Na (< 1.5 atm% for Na, and < 1.7 atm% for Ca), and a small enrichment of B (< 1.5 atm%) compared to the pristine glass melt surface. The measured quantification error (using XPS) of the concentration of Na was ~±0.5 atm%, Ca was ~±0.3 atm% and B was ~±0.4 atm%. After 2 hours of reaction, the composition of reacted glass surface was stable as ~4.7 atm% Na, ~1.7 atm% K, ~1.6 atm% Mg, ~ 3.0 atm% Ca, ~ 2.8 atm% B, ~3.0 atm% Al, 20.8 atm% Si and 62.5 atm% O. To reach a surface retreat of ~ 20 nm, the glass surface was reacted in pH10 for 12 hours; after 216 hours of reaction in pH10, a surface retreat of ~ 100 nm was observed.

Figure III.10 shows the topography of glass surface reacted at pH2 (upper row), pH7 (middle row) and pH10 (lower row). Regardless of pH, the visual inspection on the topography suggested that the reacted glass surface roughened along with the progression of reaction. The valleys (pixels in dark color) and peaks (pixels in light color) indicated the level of roughness since roughness is defined as the variations of height over a given spatial range. All captured images (representatively shown in Figure III.10) were relatively featureless with the exception of glass surfaces reacted at pH7 for 960 hours. The glass surface reacted at pH7 for 960 hours showed a minor spatial inhomogeneity of distribution of peaks and valleys. By visual inspection, the roughness of glass surfaces

reacted at different pH showed a trend that pH10 > pH7 > pH2 at their corresponding value of surface retreat (e.g. Figure III.10).

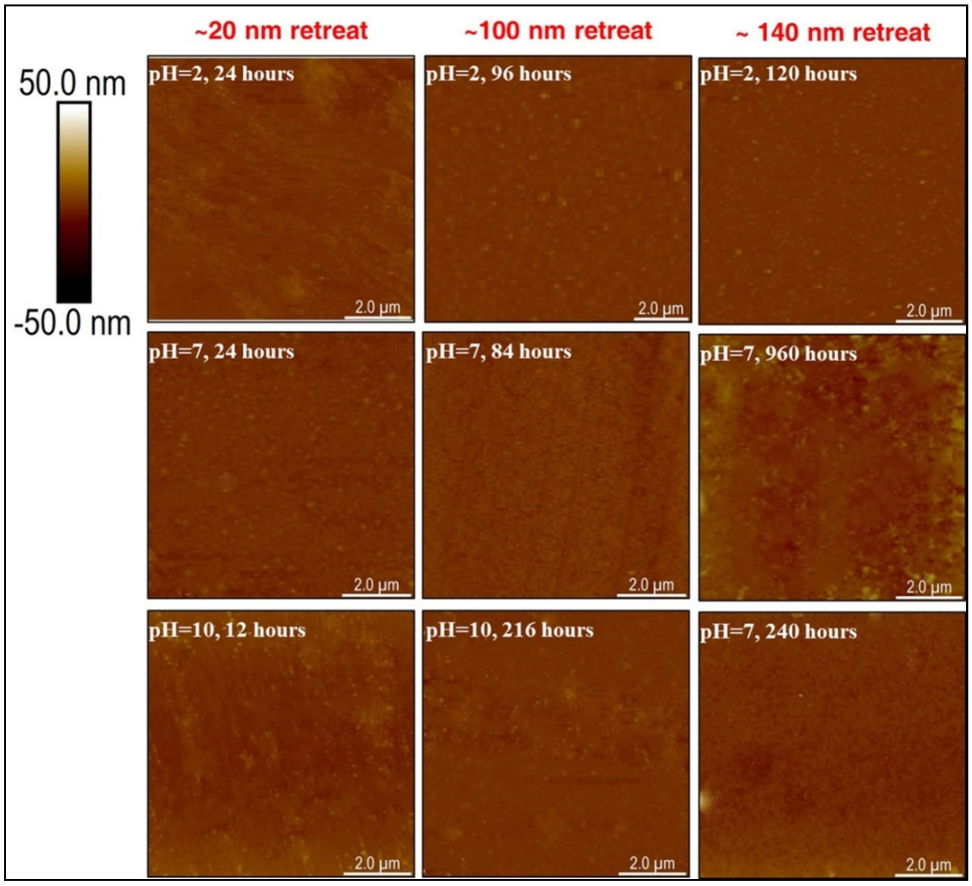


Figure III.10 Topography of reacted glass surface; upper row is the topographies of reacted glass coupon at pH=2, middle row is the topographies of reacted glass coupon at pH=7, and lower row is the topographies of reacted glass coupon at pH=10; each column of topography represents a close value of surface retreat from each image.

Given the relatively featureless topography of the glass surfaces, the roughness of the glass surfaces (pH2, pH7, and pH10) was studied using PSD analysis and was plotted as a function of reaction time (shown in Figure III.11). The equivalent RMS was obtained from PSD analysis using the k-correlation model with an average $R^2$ >98 %. For all three pH experiments, the equivalent RMS vs time was best fitted using a sigmoidal logistic

function, which parameterized the maximum roughening rate, the initial and final roughness. The obtained maximum roughening rate for pH2, pH7 and pH10 was 1.5, 5.5 and 28.5 nm/day. The fitted initial roughness was 1.8 nm, as in close agreement with the measured equivalent RMS value. The final equivalent RMS of was ~10.4 nm (pH2), ~15.3 nm (pH7) and ~30.3 nm (pH10). It was found that the cease of roughening was closely related to the change of surface retreat rate given the simultaneous phenomenological observation (e.g. cease of roughening occurred when the dissolution rate changed, as shown in Figure III.7 and Figure III.11).

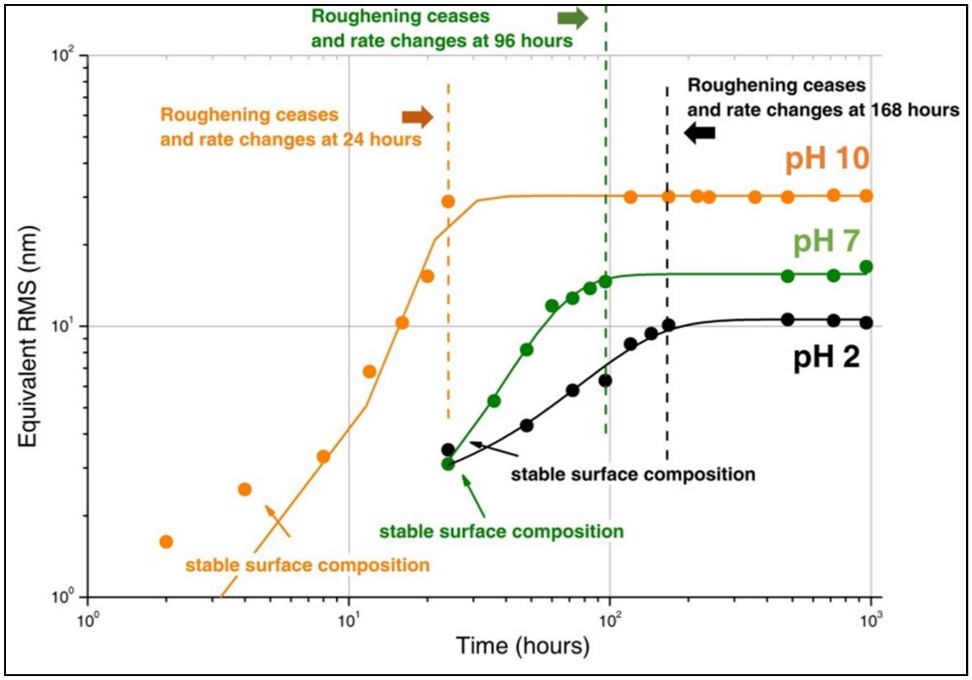


Figure III.11 Equivalent RMS roughness vs reaction time of reacted area of glass coupon reacted at pH=2 (black), pH=7 (olive), and pH=10 (orange); lines are the simulated curve using the sigmoidal logistic function, the simulation can model the maximum roughening rate, initial and final surface roughness value.

In addition to the investigation on the equivalent RMS as a function of reaction time, the spatial distribution homogeneity of roughness (as indicated by Hurst exponent) was studied as well. The fractal model was used to extract the Hurst exponent from the

PSD profiles (Figure III.12a, b and c). The Hurst exponent of glass surface reacted at pH10 was higher than pH7, and the lowest value of Hurst exponent (~ 0.45) was observed for glass surface in pH2 experiment. For the Hurst exponents obtained from PSD profiles of pH2 and pH7 experiment, the value showed a slight increase over time but remained well below 0.5.

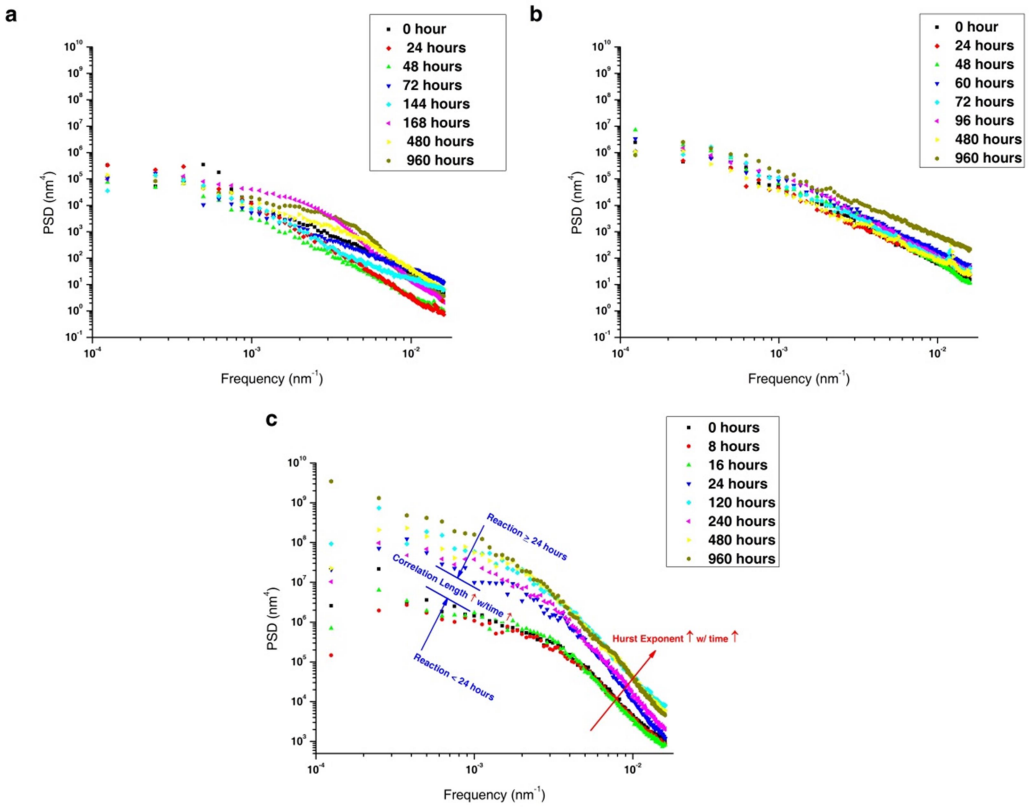


Figure III.12 Plots of PSD profiles obtained from the AFM image of glass coupons reacted at a) pH2, b) pH7 and c) pH10.

In addition to the stable correlation length and Hurst exponent values in pH2 and pH7 experiment, there was no noticeable change in terms of the features of PSD profiles as a function of time (e.g. Figure III.12a and b). The Hurst exponent of glass surface reacted at pH10 showed a sudden increase from 0.43 (< 20 hours) to 0.69 after being

reacted for 24 hours, after which point the correlation length of glass surface reacted at pH10 decreased significantly (> 50% of reduction). In order to visualize such transitional change of correlation length and Hurst exponent in PSD profiles, the PSD profiles of glass surfaces (reacted in pH10) were plotted as Figure III.12c. The sudden decrease of correlation length after 24 hours of reaction (pH10) was reflected in Figure III.12c as a gap of power in low frequency regions (< $10^{-3}$ $nm^{-1}$). The gap between surfaces reacted less, and more than 24 hours was on the order of $10^6$s $nm^4$. The abrupt increase of Hurst exponent after 24 hours of reaction in pH10 was indicated by the increase of slope in the quasi-linear region of PSD profiles (at high frequency region, $6.25*10^{-3}$ to $1.6*10^{-2}$ $nm^{-1}$).

## 4. Discussion

### 4.1 Validation of experimental method

The annealing of glass melt surfaces at elevated temperature reduced the thermal stress, and allowed the structural relaxation on glass surfaces. However, the annealing introduced the compositional change of the outermost glass surfaces such as depletion of modifier ion Na and volatile B. The depletion in Na and B concentration and enrichment of Ca, Mg and K are related to the thermal processes that glass has experienced, most likely annealing process; such effect of thermal history on the composition of aluminoborosilicate glass surfaces has been reported elsewhere [26], and thus is not discussed here. In this study, the extent of depletion in Na and B concentration on the glass melt surface was similar to the level of depletion (~ 4.0 atm%) reported by previous studies [26]. Given the minor deviation between the composition of glass melt surfaces and bulk glass composition, it was believed that the as-prepared glass melt surface can be a suitable surrogate for the bulk composition when studying the corrosion behavior of this

particular glass. The glass melt surfaces provided an atomically smooth topography (equivalent RMS of pristine glass melt surface was 1.8 nm), which reduced the error of rates (both surface retreat rate and dissolution rate) associated with surface roughness as shown in equation (3).

The successful measurement of surface retreat relies on: a) the full removal of the polymeric mask; b) the inertness of the polymeric mask against the attacks of aqueous solution; c) the impermeable network of the polymeric mask that does not allow the aqueous species ($H^+$, $H_3O^+$, $OH^-$) to diffuse through. Thus, C1s XPS spectra of the cured polymeric mask, masked (post-exfoliation) and reacted glass surfaces were evaluated and compared (e.g. Figure III.4a &b). The understanding of the bonding environment of the polymeric mask is crucial to the evaluation of its inertness and exfoliation mechanism. As shown in Figure III.4a & b, the three resolved peaks under the C1s spectrum of the polymeric mask corresponded to C-C/-H/-Si (284.6 eV), C-N (285.3 eV) and C-O (287.2 eV) bonds as reported by Senshu and et. al [68]. The C-N component in the polymeric mask had an equivalent peak intensity compared to C-C/-H/-Si, and the C-N component in C1s peak was much more prominent than C-N component in C1s peak of pure silicone [68]. Such increment of C-N bonds was contributed from the addition of cyanoacrylate into silicone given the chemical formula of cyanoacrylate is $C_6H_7NO_2$, where nitrogen atom is only bonded to carbon atoms. Other than the peak intensity of C-N bond in C1s spectra, there was no other characteristic difference in C1s spectra of the polymeric mask and the pure silicone. The addition of cyanoacrylate does not change the chemical environment of silicone as suggested by the comparison of C1s spectra of the polymeric mask and the pure silicone. Also, to the author's best knowledge, there was no literature suggesting

reaction between pure silicone and cyanoacrylate at 40 $^{o}$C (temperature of mixing) and 90 $^{o}$C (temperature of reaction). Cyanoacrylate has been proven to be a suitable part of developing an interpenetrating network without compromising the water-proof, mechanical strength, and chemical-resistance of other polymer matrixs (e.g. polyamide) [68, 69]. Thus, the polymeric mask developed in this study was believed to be a polymeric composite of pure silicone and cyanoacrylate, whose exfoliation mechanism was the dissolving of cyanoacrylate in polar solvent like acetone.

The C1s peaks of masked or reacted glass surface were symmetric adventitious alkyl C1s peak located at 284.6 eV, regardless of the corrosion conditions (e.g. Figure III.4a & b). The C-N and C-O bonds were not found on the masked glass surfaces (post exfoliation) regardless of pH and reaction time as shown in Figure III.4a. As shown in Figure III.4b, the C1s spectra of reacted glass surface were symmetric, and the characteristic C-N or C-O bond of the polymeric mask was absent from the spectra. The symmetric C1s peaks observed are from hydrocarbon species of the air. Therefore, there was no dissolving & redepositing phenomenon of the polymeric mask onto the reacted glass surfaces occurred. This conclusion was supported by the AFM image of reacted glass surfaces (e.g. Figure III.10) as well. There was no variation in composition or chemical environment of masked glass surfaces as a function of corrosion (time, pH, and temperature). The aqueous corrosion occurs on the glass surface is often accompanied by the topographical evolution of glass surfaces, most eminently the roughening of glass surface due to the structural change of network (e.g. removal of network former) of glass surface. The roughening of glass surfaces under aqueous corrosion have been reported by Mellott and Pantano [23], and were referred here as a criterion to evaluate the

protectiveness of the polymeric composite as a mask for the glass surface. Throughout the experiments, the equivalent RMS of masked glass surface remained ~ 1.7 to 1.9 nm regardless of the solution environment. Hence, the polymeric mask developed in this study met the pre-requisite for the proposed experiment as schematically shown in Figure III.1.

**4.2 Kinetics and mechanisms of glass corrosion at pH2, 7 and 10**

The statistically sound measurement of dissolution rate relies on the estimation of errors associated with surface roughness (shown in equation (3)), wearing of the AFM tip, and the error of rate analysis. However, the wearing effect of AFM tip on the accuracy of the height quantification was negligible at least in the working load of 10 scanning cycles (error is $\leq$ 1.0%) as shown in Figure III.5. The imaging of the height standard featured a sharp interface between the substrate and the top surface of the pillars, and such sharp interface was observed in most AFM images of surface retreat as well (e.g. Figure III.6a & c). However, though not common, the curved shape of surface retreat was observed as shown in Figure III.6b. There was no relation found between the curved interface and the corrosion conditions (time, temperature, solution). Figure III.6b showed an example of how the fitting method of obtaining surface retreat values in this study can particularly be useful when the surface retreat was in a curved shape. The method proposed by Icenhower [19], which measures the distance between the lowest valley and the highest peak of the surface retreat, could introduce significant errors to the measurement. The curved shape of the surface retreat can be caused by image flattening, plane fit of both included planes, other image processing related problems [70], and a worn tip [71]. As shown by the evaluation of tip wearing effect (e.g. Figure III.5), a worn tip was

less probable given the fact that the geometry of each tip was regularly checked during the image acquisition with a TipCheck® standard. Regardless of the shape of the surface retreat, the processing of AFM images related to the leveling of surface generally does not change the scale or size of measured features as more informatively discussed elsewhere [72, 73]. It needs to be pointed out that the use of surface retreat rate as a parameter of glass corrosion was based on the assumption that glass was being dissolved homogenously in spatial distribution, i.e. no difference in retreat value per reacting area. During the acquisition of AFM images, the irregular-shaped horizontal interface was caused by the manual application of polymeric mask onto the pristine glass melt surface [19]. Such rough feature was retained until the end of the experiment.

The plot of surface retreat vs reaction time revealed the relationship between pH and corrosion. The pH2 and pH7 showed a linear rate law (pH2, <168 hours; pH7,<96 hours) followed by a non-linear rate law; throughout the experiment, pH10 experiment was controlled by linear rate law but in two different rates. Linear rate law represents a geochemical process of dissolution happening in low degree of saturation of the solution [30, 74], and is often reflected by the stoichiometrical release of the element from bulk glass (or termed as congruent dissolution); the non-linear rate law often represents a complex diffusion process controlled by the solution chemistry, saturation state and morphological change of the surfaces [30, 74].

In this study, the dissolution rates were compared to literature values. The surface retreat rate showed a trend that pH10 > pH7 > pH2. It is worth noting that the surface retreat rate of the pH7 experiment was obtained by reacting the glass coupons at 90 $^{o}$C,

while pH2 and pH10 experiments were conducted at 25 $^{o}$C. The effect of temperature on the dissolution rate was reported to be an Arrhenius relationship, and resulted in the difference of dissolution rate by several orders of magnitude [11, 12]. Therefore, the 90 $^{o}$C reaction temperature of the pH7 group was responsible for the higher surface retreat rate compared to the rate of pH2. The obtained surface retreat rates were then inputted into equation (2) and (3) to generate dissolution rates with propagated errors. The relationship between pH and dissolution rates (e.g. Figure III.8) followed the findings of other studies [11, 25, 31, 32]. The dissolution rate of pH2, pH7 and pH10 experiment was on a order of magnitude slower compared to the dissolution rate of SON 68 glass ~ 0.9 g/($m^2$d) (pH7, 90 $^{o}$C) as reported by Gin [31]. However, the glass composition of SON68 consisted of 68 oxides and was reported to be more chemically durable than a simple aluminoborosilicate glass [49, 66, 75]. Thus, the dissolution rates of this study was compared to the studies of dissolution rate on similar glasses such as E-glass, basaltic glass, rhyolitic glass, aluminosilicate glass and etc.

The dissolution rate from the study on basaltic glass at pH2, 30 $^{o}$C [11] was ~ 4.86 to 20.38*$10^{-2}$ g/($m^2$d), which was quite comparable to the rate in this study ~ 7.49±0.44*$10^{-2}$ g/($m^2$d) (pH2, 25 $^{o}$C). At pH2 the dissolution rate of this study was higher than albite (~ 0.05 g/($m^2$d)) and jadeite glass (~0.76 g/($m^2$d)) [76], close to the rate of E-glass (~ 8.01*$10^{-2}$ g/($m^2$d)) [33, 34, 35, 36, 38], and slightly slower than the rate of nepheline glass (~17.77*$10^{-2}$ g/($m^2$d)) [76] and rhyolitic glass (~ 25.36*$10^{-2}$ g/($m^2$d) [32]. With respect to the dissolution rate of jadeite and albite reported by Hamilton and Pantano [76], the concentration of Al/Si in jadeite (Al/Si=0.51) and albite glass (Al/Si=0.34) was higher than the aluminoborosilicate glass (Al/Si=0.11) used in this study. Hamilton and Pantano

reported that the dissolution rate increased with increasing Al/Si ratio in the bulk glass [76], and a similar study of the effect of network former ratios on the dissolution rate has been reported by Strachan and Croak as well [77]. Thus, the difference in dissolution rates found in albite glass, jadeite glass compared to this study was most likely to be a result of variations in Al/Si ratio. Also, the dissolution rates in this study were compared to E-glass, which has an identical element component compare to the aluminoborosilicate glass used in this work. Note that the dissolution rate or corrosion rate studied with E-glass were often reported as mass loss versus reaction time [33, 34, 35, 36, 38], and thus the rates of E-glass was converted into the unit of g/($m^2$d). For pH7 reacted at 90 $^{o}$C, the dissolution rate (~ 8.43±1.08*$10^{-2}$ g/($m^2$d)) was compared to the reported rate of E-glass (~ 8.01 to 20.31 g/($m^2$d)) [5, 33, 34, 35, 36, 38]. Similarly, the obtained dissolution rate of this study at pH10 (3.07±0.55*$10^{-2}$ g/($m^2$d)) was close to the reported study on rhyolitic glass [40]. Overall, the dissolution rates on similar glass composition (with minor variations of modifier ion) were within the same orders of magnitude compared to the dissolution rates in this study.

### 4.3 Correlations between glass dissolution and roughening

The composition of reacted glass surfaces were studied as a function of corrosion, as shown in Figure III.9 (chemical compositions of the reacted glass surfaces were detailed in Appendix C). It was found that the surface composition was relatively unchanged after 24 hours of reaction for pH2 and pH7 experiments, and after 2 hours of reaction for pH7 experiments. The stable chemical composition of reacted glass surfaces suggested that the elements within the glass network were dissolved stoichiometrically, or also known as congruent dissolution. This observation was reflected by the linear law

controlled surface retreat rate prior to the rate change as shown in Figure III.7. The congruent dissolution process depletes modifier ions and B from the glass network, and consequently leads to the dissolving of network formers into the bulk solution [8, 12, 15, 16]. Moreover, the glass surface roughened at this regime of reaction as shown in Figure III.11, and stopped roughening when the dissolution showed a non-linear relationship with time. As shown in Figure III.7 and 4.11, the glass stopped roughening while the surface retreated with corrosion. In order to understand such phenomenon, the geometrical relationship between surface retreat rate and maximum roughening rate (as vertical vectors) were studied. Figure III.13 shows a schematic of the roughening process occurred on glass surfaces.

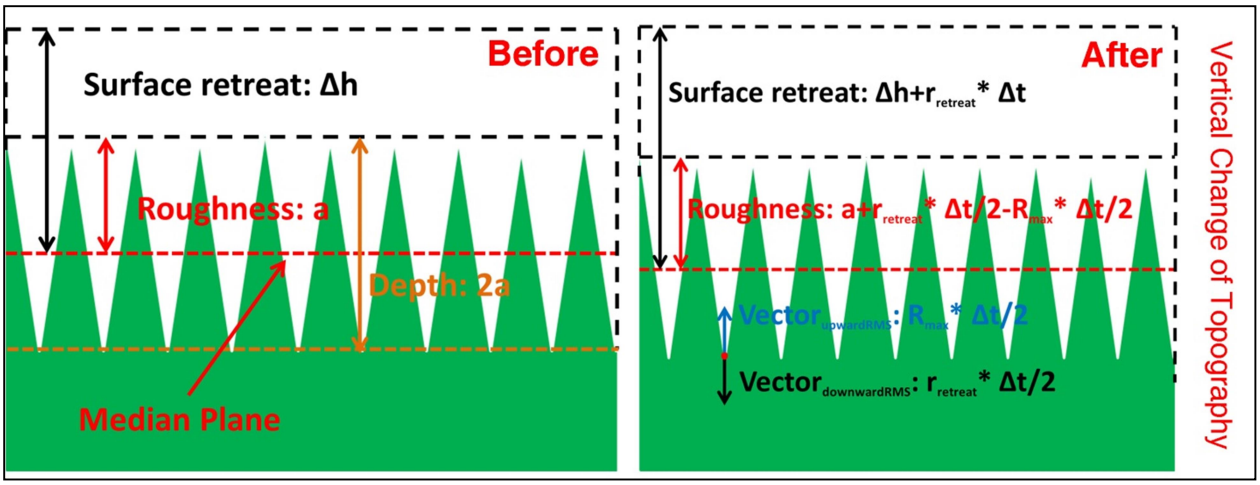


Figure III.13 Schematic showing the surface roughness after a certain period of time of reaction Δt. Surface profile before Δt is the left schematic, and surface profile after Δt is the right schematic.

As shown in Figure III.13, the initial roughness and the surface retreat (as compared to an imaginary reference surface) is a and Δh, respectively. After Δt, the roughness increases due to the corrosion of the glass surface. The surface retreat after Δt

is increased to $\Delta h + \Delta t * r_{retreat}$, where $r_{retreat}$ is the surface retreat rate. Since the roughness is the root-mean-square variation of amplitude to the mean plane, the vector of reaction contributed to roughness is $\Delta t * r_{retreat}/2$ (as half of the increment of the surface retreat). Assuming that the roughening also has vectors related to maximum roughening rate, the roughening vector in the opposite direction of reaction should be deduced from the roughness value after $\Delta t$ (the roughening vector in the direction of reaction was included in the vector of reaction given how the roughness and surface retreat was being measured). Thus, the roughness after $\Delta t$ is $a + \Delta t * r_{retreat}/2 - \Delta t * R_{max}/2$, where $R_{max}$ is the maximum roughening rate. Therefore, the roughening occurs when $a + \Delta t * r_{retreat}/2 - \Delta t * R_{max}/2$ (before) > a. By rearranging this inequality, it was found that $r_{retreat}$ must be larger than $R_{max}$ to introduce roughening. The surface retreat rates in the linear rate law regime was larger than its corresponding $R_{max}$, while the surface retreat rates in the non-linear rate law regime was smaller than the $R_{max}$s. It is reasonable that the glass will not roughen when the dissolution rate is too small to create any topographical change, especially for pH2 ($R_{max}$ is 1.5 nm/day) and pH7 ($R_{max}$ is 5.5 nm/day). Thus, it was concluded that the surface roughens only when the surface retreat rate was faster than the maximum roughening rate. Additionally, it was suggested that the maximum roughening rate $R_{max}$ might be related to the glass composition and reaction conditions that can be used to evaluate the chemical durability of glasses.

However, the $r_{retreat}$ of the pH10 experiment was 12.1 nm/day in the non-linear rate law regime. It was hard to conceptualize that the relative large retreat rate will not cause surface roughening. In order to investigate the stop of roughening observed in pH10 experiments, the correlation length and Hurst exponent were studied as a function

of time using PSD profiles (eg. Figure III.12c). After 24 hours of reaction, the correlation length significantly decreased (from ~330 nm to ~ 169 nm). The decrease of correlation length was reflected by the power gap between PSD profiles of < 24 hours and PSD profiles of > 24 hours as shown in Figure III.12c, and the gap was on the order of ~$10^6$s $nm^4$ power. The increase of power at low frequency region ($1.25*10^{-4}$ to $6.125*10^{-3}$ $nm^{-1}$) is related to the horizontal increase of the structural size [29]. Often the horizontal increase of structural size can be reflected by the non-homogeneous distribution of roughness at a given spatial wavelength. Such hypothesis has been confirmed by the study of Hurst exponent as a function of time, i.e. Hurst exponent is larger than 0.5 after 24 hours of reaction. A Hurst exponent larger than 0.5 indicates a non-homogenous distribution of roughness, and the physical meaning of the values of Hurst exponent was more informatively discussed in [26]. The sudden increase of Hurst exponent after 24 hours of reaction is shown in Figure III.12c as the change of the slopes at high frequency region ($6.25*10^{-3}$ to $1.6*10^{-2}$ $nm^{-1}$). Thus, the cease of roughening observed in the pH10 experiment was associated with the horizontal increase of roughness feature. However, the effect of $R_{max}$ on the horizontal increase of roughness feature was beyond the scope of this work. In conclusion, the corrosion of glass surface introduced the roughening, which occurred when the dissolution rate was higher than the rate of topographical change (e.g. roughness). However, the quantitative relationship between glass composition, glass dissolution, and glass roughening still remains inconclusive.

## Conclusions

In this study, a novel method of measuring dissolution rate of aluminoborosilicate glasses was developed using atomic force microscopy. The method artificially created a surface retreat by masking the glass surface using a superhydrophobic polymeric composite mask. The masking and exfoliation strategy (non-destructive) proposed in this study was validated using advanced surface analysis tools such as AFM and XPS. The surface retreat rates were obtained by fitting the surface retreat as a function of time using geochemical models such as linear rate law and non-linear rate law. Surface retreat rates were then converted into dissolution rates, which were comparable with literature values; however, minor differences in dissolution rates as a function of glass composition were observed when comparing to jadeite and nepheline glass.

It was found that the roughening of glass surface can be introduced by corrosion. The parameter representing the maximum rate of roughness change, $R_{max}$, was used to geometrically show that the dissolution rate must be higher than the $R_{max}$ in order to introduce surface roughening. Also, the relationship between glass dissolution and roughening was briefly discussed.

**References**


1. M. Jercinovic, K. Keil, M. Smith, and R. Schmitt, "Alteration of basaltic glasses from north-central British Columbia, Canada," *Geochimica et Cosmochimica Acta,* 54[10] 2679-96 (1990).

2. P. Valerio, M. M. Pereira, A. M. Goes, and M. F. Leite, "The effect of ionic products from bioactive glass dissolution on osteoblast proliferation and collagen production," *Biomaterials,* 25[15] 2941-48 (2004).

3. B. Grambow, "Nuclear waste glasses-How durable?," *Elements,* 2[6] 357-64 (2006).

4. H. Staudigel, H. Furnes, N. McLoughlin, N. R. Banerjee, L. B. Connell, and A. Templeton, "3.5 billion years of glass bioalteration: Volcanic rocks as a basis for microbial life?," *Earth-Science Reviews,* 89[3] 156-76 (2008).

5. Q. Qiu and M. Kumosa, "Corrosion of E-glass fibers in acidic environments," *Composites Science and Technology,* 57[5] 497-507 (1997).

6. H. Walters and P. Adams, "Effects of humidity on the weathering of glass," *Journal of Non-Crystalline Solids,* 19 183-99 (1975).

7. T. K. Flaathen, S. R. Gislason, E. H. Oelkers, and Á. E. Sveinbjörnsdóttir, "Chemical evolution of the Mt. Hekla, Iceland, groundwaters: a natural analogue for CO 2 sequestration in basaltic rocks," *Applied Geochemistry,* 24[3] 463-74 (2009).

8. S. Gin, A. Abdelouas, L. J. Criscenti, W. L. Ebert, K. Ferrand, T. Geisler, M. T. Harrison, Y. Inagaki, S. Mitsui, and K. T. Mueller, "An international initiative on long-term behavior of high-level nuclear waste glass," *Materials Today,* 16[6] 243-48 (2013).

9. C. Cailleteau, F. Angeli, F. Devreux, S. Gin, J. Jestin, P. Jollivet, and O. Spalla, "Insight into silicate-glass corrosion mechanisms," *Nature Materials,* 7[12] 978-83 (2008).

10. L. Werme, I. K. Björner, G. Bart, H. U. Zwicky, B. Grambow, W. Lutze, R. C. Ewing, and C. Magrabi, "Chemical corrosion of highly radioactive borosilicate nuclear waste glass under simulated repository conditions," *Journal of Materials Research,* 5[05] 1130-46 (1990).

11. S. R. Gislason and E. H. Oelkers, "Mechanism, rates, and consequences of basaltic glass dissolution: II. An experimental study of the dissolution rates of basaltic glass as a function of pH and temperature," *Geochimica et Cosmochimica Acta,* 67[20] 3817-32 (2003).

12. E. H. Oelkers and S. R. Gislason, "The mechanism, rates and consequences of basaltic glass dissolution: I. An experimental study of the dissolution rates of basaltic glass as a function of aqueous Al, Si and oxalic acid concentration at 25 C and pH= 3 and 11," *Geochimica et Cosmochimica Acta,* 65[21] 3671-81 (2001).

13. V. Daux, C. Guy, T. Advocat, J.-L. Crovisier, and P. Stille, "Kinetic aspects of basaltic glass dissolution at 90 C: role of aqueous silicon and aluminium," *Chemical Geology,* 142[1] 109-26 (1997).

14. G. Berger, C. Claparols, C. Guy, and V. Daux, "Dissolution rate of a basalt glass in silica-rich solutions: implications for long-term alteration," *Geochimica et Cosmochimica Acta,* 58[22] 4875-86 (1994).

15. P. Frugier, S. Gin, Y. Minet, T. Chave, B. Bonin, N. Godon, J.-E. Lartigue, P. Jollivet, A. Ayral, and L. De Windt, "SON68 nuclear glass dissolution kinetics:

Current state of knowledge and basis of the new GRAAL model," *Journal of Nuclear Materials,* 380[1] 8-21 (2008).

16. R. Hellmann, S. Cotte, E. Cadel, S. Malladi, L. S. Karlsson, S. Lozano-Perez, M. Cabié, and A. Seyeux, "Nanometre-scale evidence for interfacial dissolution–reprecipitation control of silicate glass corrosion," *Nature Materials,* 14[3] 307-11 (2015).
17. S. J. Gordon and P. V. Brady, "In situ determination of long-term basaltic glass dissolution in the unsaturated zone," *Chemical Geology,* 190[1] 113-22 (2002).
18. A. F. White and S. L. Brantley, "The effect of time on the weathering of silicate minerals: why do weathering rates differ in the laboratory and field?," *Chemical Geology,* 202[3] 479-506 (2003).
19. J. P. Icenhower and C. I. Steefel, "Dissolution rate of borosilicate glass SON68: A method of quantification based upon interferometry and implications for experimental and natural weathering rates of glass," *Geochimica et Cosmochimica Acta,* 157 147-63 (2015).
20. S. A. Parry, M. E. Hodson, S. J. Kemp, and E. H. Oelkers, "The surface area and reactivity of granitic soils: I. Dissolution rates of primary minerals as a function of depth and age deduced from field observations," *Geoderma,* 237 21-35 (2015).
21. W. L. Ebert, C. L. Crawford, and C. M. Jantzen, "Uncertainty in the Surface Area of Crushed Glass in Rate Calculations," *MRS Proceedings*, Vol. 1744 145-152 (2015), Cambrige University Press.

22. B. Parruzot, P. Jollivet, D. Rébiscoul, and S. Gin, "Long-term alteration of basaltic glass: Mechanisms and rates," *Geochimica et Cosmochimica Acta,* 154 28-48 (2015).

23. N. P. Mellott and C. G. Pantano, "A Mechanism of Corrosion-Induced Roughening of Glass Surfaces," *International Journal of Applied Glass Science,* 4[3] 274-79 (2013).

24. F. Delage and J. Dussossoy, "R7T7 glass initial dissolution rate measurements using a high-temperature Soxhlet device," *MRS Proceedings*. Vol. 212 41 (1990), Cambridge University Press.

25. Y. Inagaki, T. Kikunaga, K. Idemitsu, and T. Arima, "Initial Dissolution Rate of the International Simple Glass as a Function of pH and Temperature Measured Using Microchannel Flow-Through Test Method," *International Journal of Applied Glass Science,* 4[4] 317-27 (2013).

26. Y. Gong, A. W. Wren, and N. P. Mellott, "Quantitative morphological and compositional evaluation of laboratory prepared aluminoborosilicate glass surfaces," *Applied Surface Science,* 324 594-604 (2015).

27. D. Rebiscoul, A. Van der Lee, F. Rieutord, F. Né, O. Spalla, A. El-Mansouri, P. Frugier, A. Ayral, and S. Gin, "Morphological evolution of alteration layers formed during nuclear glass alteration: new evidence of a gel as a diffusive barrier," *Journal of Nuclear Materials,* 326[1] 9-18 (2004).

28. P. K. Ojha, T. Chongdar, N. Gokhale, and A. Kulkarni, "Investigation of crystallization kinetic of $SrO–La_2O_3–Al_2O_3–B_2O_3–SiO_2$ glass and its suitability

for SOFC sealant," *international Journal of Hydrogen Energy,* 36[22] 14996-5001 (2011).

29. S. Fang, S. Haplepete, W. Chen, C. Helms, and H. Edwards, "Analyzing atomic force microscopy images using spectral methods," *Journal of Applied Physics,* 82[12] 5891-98 (1997).
30. S. L. Brantley, "Kinetics of mineral dissolution," pp. 151-210. in Kinetics of water-rock interaction**.** Springer, 2008.
31. S. Gin and J. P. Mestre, "SON 68 nuclear glass alteration kinetics between pH 7 and pH 11.5," *Journal of Nuclear Materials,* 295[1] 83-96 (2001).
32. J. Declercq, T. Diedrich, M. Perrot, S. R. Gislason, and E. H. Oelkers, "Experimental determination of rhyolitic glass dissolution rates at 40–200 C and 2< pH< 10.1," *Geochimica et Cosmochimica Acta,* 100 251-63 (2013).
33. H. Li, P. Gu, J. Watson, and J. Meng, "Acid corrosion resistance and mechanism of E-glass fibers: boron factor," *Journal of Materials Science,* 48[8] 3075-87 (2013).
34. L. MIŠÍKOVÁ, M. LIŠKA, and D. Galuskova, "Corrosion of E-glass fibers in distilled water," *Ceramics− Silikáty,* 51[3] 131-35 (2007).
35. B. Das, B. Tucker, and J. Watson, "Acid corrosion analysis of fibre glass," *Journal of Materials Science,* 26[24] 6606-12 (1991).
36. A. Al Cheikh and M. Murat, "Kinetics of non-congruent dissolution of E-glass fiber in saturated calcium hydroxide solution," *Cement and Concrete Research,* 18[6] 943-50 (1988).

37. A. Czymai and G. H. Frischat, "A method to determine concentration-distance profiles of corroded glass fibers," *Journal of Non-Crystalline solids,* 191[1] 138-45 (1995).

38. B. Wei, H. Cao, and S. Song, "Tensile behavior contrast of basalt and glass fibers after chemical treatment," *Materials & Design,* 31[9] 4244-50 (2010).

39. C. F. Windisch, E. M. Pierce, S. D. Burton, and C. C. Bovaird, "Deep-UV Raman spectroscopic analysis of structure and dissolution rates of silica-rich sodium borosilicate glasses," *Journal of Non-Crystalline Solids,* 357[10] 2170-77 (2011).

40. D. Wolff-Boenisch, S. R. Gislason, E. H. Oelkers, and C. V. Putnis, "The dissolution rates of natural glasses as a function of their composition at pH 4 and 10.6, and temperatures from 25 to 74 C," *Geochimica et Cosmochimica Acta,* 68[23] 4843-58 (2004).

41. E. M. Pierce, E. A. Rodriguez, L. J. Calligan, W. J. Shaw, and B. P. McGrail, "An experimental study of the dissolution rates of simulated aluminoborosilicate waste glasses as a function of pH and temperature under dilute conditions," *Applied Geochemistry,* 23[9] 2559-73 (2008).

42. R. Doremus, "Time dependence of the reaction of water with glass," *Nuclear and Chemical Waste Management,* 2[2] 119-23 (1981).

43. G. Leturcq, G. Berger, T. Advocat, and E. Vernaz, "Initial and long-term dissolution rates of aluminosilicate glasses enriched with Ti, Zr and Nd," *Chemical Geology,* 160[1] 39-62 (1999).

44. J. P. Icenhower, B. P. McGrail, W. J. Shaw, E. M. Pierce, P. Nachimuthu, D. K. Shuh, E. A. Rodriguez, and J. L. Steele, "Experimentally determined dissolution

kinetics of Na-rich borosilicate glass at far from equilibrium conditions: implications for transition state theory," *Geochimica et Cosmochimica Acta,* 72[12] 2767-88 (2008).

45. B. P. McGrail, J. P. Icenhower, D. Shuh, P. Liu, J. G. Darab, D. R. Baer, S. Thevuthasen, V. Shutthanandan, M. H. Engelhard, and C. Booth, "The structure of Na 2 O–Al 2 O 3–SiO 2 glass: impact on sodium ion exchange in H 2 O and D 2 O," *Journal of Non-Crystalline Solids,* 296[1] 10-26 (2001).
46. M. Bengisu, R. K. Brow, E. Yilmaz, A. Moguš-Milanković, and S. Reis, "Aluminoborate and aluminoborosilicate glasses with high chemical durability and the effect of P 2 O 5 additions on the properties," *Journal of Non-Crystalline Solids,* 352[32] 3668-76 (2006).
47. C. Cailleteau, C. Weigel, A. Ledieu, P. Barboux, and F. Devreux, "On the effect of glass composition in the dissolution of glasses by water," *Journal of Non-Crystalline Solids,* 354[2] 117-23 (2008).
48. B. Bergeron, L. Galoisy, P. Jollivet, F. Angeli, T. Charpentier, G. Calas, and S. Gin, "First investigations of the influence of IVB elements (Ti, Zr, and Hf) on the chemical durability of soda-lime borosilicate glasses," *Journal of Non-Crystalline Solids,* 356[44] 2315-22 (2010).
49. C. Jégou, S. Gin, and F. Larché, "Alteration kinetics of a simplified nuclear glass in an aqueous medium: effects of solution chemistry and of protective gel properties on diminishing the alteration rate," *Journal of Nuclear Materials,* 280[2] 216-29 (2000).

50. B. Grambow and R. Müller, "First-order dissolution rate law and the role of surface layers in glass performance assessment," *Journal of Nuclear Materials,* 298[1] 112-24 (2001).

51. M. I. Ojovan, R. J. Hand, N. V. Ojovan, and W. E. Lee, "Corrosion of alkali–borosilicate waste glass K-26 in non-saturated conditions," *Journal of Nuclear Materials,* 340[1] 12-24 (2005).

52. H. Zhang, C. L. Corkhill, P. G. Heath, R. J. Hand, M. C. Stennett, and N. C. Hyatt, "Effect of Zn-and Ca-oxides on the structure and chemical durability of simulant alkali borosilicate glasses for immobilisation of UK high level wastes," *Journal of Nuclear Materials,* 462 321-28 (2015).

53. M. H. Krohn, J. R. Hellmann, B. Mahieu, and C. G. Pantano, "Effect of tin-oxide on the physical properties of soda-lime–silica glass," *Journal of Non-Crystalline Solids,* 351[6] 455-65 (2005).

54. J. Shelby, J. Vitko, and C. Pantano, "Weathering of glasses for solar applications," *Solar Energy Materials,* 3[1] 97-110 (1980).

55. N. J. Smith and C. G. Pantano, "Leached layer formation on float glass surfaces in the presence of acid interleave coatings," *Journal of the American Ceramic Society,* 91[3] 736-44 (2008).

56. H. Tanaka, K. Kuraoka, H. Yamanaka, and T. Yazawa, "Development and disappearance of microporous structure in acid treated E-glass fiber," *Journal of Non-Crystalline Solids,* 215[2] 262-70 (1997).

57. T. H. ELMER, "Leaching of E-Glass," *Journal of the American Ceramic Society,* 67[12] 778-82 (1984).

58. H. Chandler and R. Jones, "Strength loss in ″E ″glass fibres treated in strong solutions of mineral acids," *Journal of Materials Science,* 19[12] 3849-54 (1984).

59. R. Jones and D. Betz, "The kinetics of corrosion of E-glass fibres in hydrochloric acid," *Journal of Materials Science,* 39[18] 5633-37 (2004).

60. R. L. Jones, "Chemical Corrosion of E-Glass Fibers in Oxalic and Other Organic Acids," *Journal of the American Ceramic Society,* 89[1] 20-23 (2006).

61. S. Nagae and Y. Otsuka, "Effect of sizing agent on corrosion of glass fibres in water," *Journal of Materials Science Letters,* 13[20] 1482-83 (1994).

62. B. Ramachandran, B. Pai, and N. Balasubramanian, "Electrical resistivity studies on acid-treated E-glass fabric," *Journal of Materials Science,* 14[7] 1572-78 (1979).

63. B. Ramachandran, B. Pai, and N. Balasubramanian, "Studies on the acid resistance of E Glass," *Journal of the American Ceramic Society,* 63[1-2] 1-3 (1980).

64. E. L. Rodriguez, "Corrosion of glass fibres," *J Journal of Materials Science Letters,* 6[6] 718-20 (1987).

65. C. Tian, W. Zhou, K. He, Z. Zhang, L. Zhang, Z. Liu, Z. Zhang, X. Li, and J. Zhang, "Study of the high purity and ultrafine silica fibre," *Journal of Materials Science,* 27[3] 767-70 (1992).

66. S. Gin, X. Beaudoux, F. Angéli, C. Jégou, and N. Godon, "Effect of composition on the short-term and long-term dissolution rates of ten borosilicate glasses of increasing complexity from 3 to 30 oxides," *Journal of Non-Crystalline Solids,* 358[18] 2559-70 (2012).

67. A. F. White, "Surface chemistry and dissolution kinetics of glassy rocks at 25 C," *Geochimica et Cosmochimica Acta,* 47[4] 805-15 (1983).

68. K. Senshu, T. Furuzono, N. Koshizaki, S. Yamashita, T. Matsumoto, A. Kishida, and M. Akashi, "Novel Functional Polymers: Poly (dimethylsiloxane)-Polyamide Multiblock Copolymer. 8. 1 Surface Studies of Aramid-Silicone Resin by Means of XPS, Static SIMS, and TEM," *Macromolecules,* 30[15] 4421-28 (1997).

69. A. Attanasio, I. S. Bayer, R. Ruffilli, F. Ayadi, and A. Athanassiou, "Surprising High Hydrophobicity of Polymer Networks from Hydrophilic Components," *ACS Applied Materials & Interfaces,* 5[12] 5717-26 (2013).

70. E. Meyer, "Atomic force microscopy," *Progress in Surface Science,* 41[1] 3-49 (1992).

71. W. Maw, F. Stevens, S. Langford, and J. Dickinson, "Single asperity tribochemical wear of silicon nitride studied by atomic force microscopy," *Journal of Applied Physics,* 92[9] 5103-09 (2002).

72. G. Bar, Y. Thomann, R. Brandsch, H.-J. Cantow, and M.-H. Whangbo, "Factors affecting the height and phase images in tapping mode atomic force microscopy. Study of phase-separated polymer blends of poly (ethene-co-styrene) and poly (2, 6-dimethyl-1, 4-phenylene oxide)," *Langmuir,* 13[14] 3807-12 (1997).

73. J. L. Hutter and J. Bechhoefer, "Calibration of atomic-force microscope tips," *Review of Scientific Instruments,* 64[7] 1868-73 (1993).

74. W. Stumm and R. Wollast, "Coordination chemistry of weathering: Kinetics of the surface-controlled dissolution of oxide minerals," *Reviews of Geophysics,* 28[1] 53-69 (1990).

75. N. Rajmohan, P. Frugier, and S. Gin, "Composition effects on synthetic glass alteration mechanisms: Part 1. Experiments," *Chemical Geology,* 279[3–4] 106-19 (2010).

76. J. P. Hamilton, S. L. Brantley, C. G. Pantano, L. J. Criscenti, and J. D. Kubicki, "Dissolution of nepheline, jadeite and albite glasses: toward better models for aluminosilicate dissolution," *Geochimica et Cosmochimica Acta,* 65[21] 3683-702 (2001).

77. D. M. Strachan and T. L. Croak, "Compositional effects on long-term dissolution of borosilicate glass," *Journal of Non-Crystalline Solids,* 272[1] 22-33 (2000).

# CHAPTER IV. NEW EVIDENCE OF THE INTERFACIAL DISSOLUTION REPRECIPITATION MECHANISM OF SILICA LAYER FORMATION DURING GLASS CORROSION: INSIGHT FROM SYNCHROTRON RADIATED X-RAY REFLECTIVITY AND DIFFUSE SCATTERING

## 1. Introduction

The glass corrosion mechanisms are of particular interest to the evaluation of the chemical durability of glasses in biomedical applications, natural glass in balancing global carbon dioxide sequestration, and nuclear waste glass in disposal conditions [1]. The estimation of corrosion behavior of nuclear waste glass is a prioritized task before the wide application of nuclear energy as an alternative/renewable energy source in the age of energy crisis [2]. Glasses dedicated to the vitrification of nuclear wastes develop a silica-rich gel at the glass/solution interface when exposed to the aqueous solution for certain periods of time [3]. The silica-rich gel is reported to be constituted with the cross-linking species such as Si and Al [3, 4]. The existence of such gel, which often occurs when the solution is saturated with respect to Si, is arguably acting as a diffusion barrier that leads to a decrease in the dissolution rate by four orders of magnitude compared to the initial dissolution rate [5]. The textural properties (e.g. density and morphology) of the gel are dependent on the glass composition as well as the solution environment (pH, temperature, and ion species) [4, 5]. It has been reported that the formation of the gel is a direct result of the recondensation of the cross-linking species in de-alkalized glass [4]. Rebiscoul et. al. [4] reported that the altered glass features an interdiffusion zone with graded density (de-

alkalized glass with chemical gradients) in between the pristine glass (inner rim) and the gel (outer rim). However, this particular experimental result on XRR does not account for the highly texturized (so-called porosity between layers) alteration zone observed in historical glasses and glasses corroded in laboratory conditions as reported by Geisler et. al. [5, 6]. Recent studies by Hellmann et. al., with the use of advanced analytical tools such as atom probe tomography (APT), found that the structural and chemical interface between the pristine glass and alteration zone was atomically sharp [1]. The responsible mechanism was reported as an interfacial dissolution and reprecipitation process [5], which differs from the long-standing diffusion coupled-hydration and cation leaching mechanism previously used. The interfacial dissolution and reprecipitation mechanism in glass corrosion, as originally proposed by Geisler et. al. [5], was followed by a study concluding that the diffusion coupled mechanism was proposed with observations based on poorly resoluted instruments [7]. However, the interfacial dissolution and reprecipitation mechanism lacks parameterized variables (such as gel density, interface roughness, and other derivative properties) to quantify or at least model the glass dissolution behavior in the long term (millions of years).

In this study, two commercially available flat panel silicate glasses were corroded in acidic solution at an elevated temperature to study the textural properties of the altered glass as a function of time. For the first time, the textural properties were measured by coupling the simulation of synchrotron radiated X-ray reflectivity and diffuse scattering. In addition, the chemical composition and environment of the outermost altered glass surface were studied using X-ray photoelectron spectroscopy. It was found that the interface roughness and non-gradient density of the de-alkalized glass were in support of

the interfacial dissolution and reprecipitation mechanism. Moreover, the recondensation of de-alkalized glass to form the dense silica gel was not observed throughout the experiment. The calculation of the de-alkalized glass thickness, especially after forming the dense silica gel, suggested that the dense silica layer was probably formed by the interfacial dissolution and reprecipitation of the de-alkalized glass instead of the reported structural recondensation or bulk solution Si precipitation mechanism. Modeling of the surface composition and density based on XPS and XRR/XDS data also favored such a mechanism. More importantly, this work provides a preliminary parameterized set of variables that can be further used in the modeling of the long-term behavior of glass corrosion.

## 2. Materials and methods

### 2.1 Sample preparation

The D263 glass and soda-lime-silicate glass, whose compositions are detailed in Table 4.1 (measured using Perkin-Elmer Optima 5300, an inductively coupled plasma atomic emission spectrometer), were used to conduct the corrosion experiment.

Table 4.1 Composition (wt%) of the SLS and D263 Bulk Glass using Spectrochemical Analysis

| Sample | $Al_2O_3$ (wt%) | $B_2O_3$ (wt%) | CaO (wt%) | $Fe_2O_3$(wt%) | $K_2O$ (wt%) | MgO (wt%) | $Na_2O$ (wt%) | $SiO_2$ (wt%) | $TiO_2$ (wt%) | ZnO (wt%) | Total |
|---|---|---|---|---|---|---|---|---|---|---|---|
| D263 | 4.34 | 9.67 | Trace | Trace | 6.43 | 0.03 | 6.37 | 63.84 | 4.23 | 5.09 | 100.0 |
| SLS | 0.45 | Trace | 10.76 | Trace | Trace | 3.54 | 13.78 | 71.47 | Trace | Trace | 100.0 |

*Trace: measured value is smaller than the standard deviation

Particularly, the composition of the D263 glass is close to the molar ratios of nuclear waste glasses (e.g. SON68, a French nuclear waste form glass). Both glasses were purchased from vendors (S.I. Howard Glass, Massachusetts, MA), and were checked with

a diffractometer (Bruker Phaser D2, California, USA) to be X-ray amorphous. The panel glasses were cut into monoliths with a size of 50 mm X 20 mm using a low-speed diamond saw cooled by polishing oil. The cut glass panels were ultrasonicated in acetone and isopropanol alcohol for 10 mins each, rinsed in deionized water, dried under a nitrogen gas flow (~100 mL/min), and then stored in vacuum desiccator prior to any experiments or characterization. For soda-lime-silicate glass, which is a float glass produced in the molten tin bath, the tin side was avoided for analysis using a high-intensity UV lamp to distinguish the air side from the tin side. The corrosion test was performed with dilute HCl solution (pH3) in an oven heated at 90 $^{o}$C. The pH of the solution was measured before and after the corrosion test at 90 $^{o}$C, the measured pH is detailed in Table 4.2. The D263 and SLS glass monoliths were corroded in the pH3 solution for up to 250 hours with a glass-surface-area-to-solution-volume ratio (SA/V) of 10 $m^{-1}$.

Table 4.2 Variations of Solution pH (as measured at 90 $^{o}$C) as a Function of Reaction Time for SLS and D263 Experiments

| SLS | | D263 | |
|---|---|---|---|
| **Time** | **pH** | **Time** | **pH** |
| 0 hour | 3.0±0.2 | 0 hour | 3.0±0.2 |
| 1 hours | 3.0±0.3 | 1 hours | 3.0±0.1 |
| 5 hours | 3.2±0.3 | 5 hours | 3.0±0.3 |
| 50 hours | 3.3±0.4 | 50 hours | 3.1±0.4 |
| 100 hours | 3.3±0.1 | 100 hours | 3.1±0.3 |
| 150 hours | 3.5±0.3 | 150 hours | 3.2±0.4 |
| 200 hours | 3.8±0.2 | 200 hours | 3.2±0.1 |
| 250 hours | 4.0±0.1 | 250 hours | 3.2±0.1 |

All corrosion tests were performed in a pre-cleaned high density polyethylene (HDPE) bottle. The HDPE bottles were cleaned by soaking them in a dilute $HNO_3$/HCl

solution for two days, and followed by soaking in deionized water for one week. The HDPE bottles, the pH3 solution, and the glass samples were placed in an regulated oven at 90 $^{o}$C for two hours, prior to placing the monoliths in the bottles. After experiments, the monoliths were rinsed with deionized water followed by isopropanol alcohol to avoid any possible effect of sample drying on the characterization. All collected and rinsed samples were dried under a nitrogen gas flow and stored in vacuum desiccator prior to any analysis.

**2.2 Synchrotron radiated X-ray reflectivity and X-ray diffuse scattering**

The X-ray reflectivity (XRR) and diffuse scattering (XDS) curves of the corroded SLS and D263 glass were collected at the beamline G2 at Cornell High Energy Synchrotron Source (CHESS). The experiments were performed at the ambient condition with a photon energy of 13.6 keV (wavelength of ~ 0.10688 nm). The shape of the direct beam was measured and adjusted to be a Gaussian distribution via changing the size of the beam slits. The detector used in beamline G2 was a 2D ring detector with 2D imaging capabilities of the actual beam. Thus, the 2D images of the direct beam were collected simultaneously to identify any diffraction events (eg. formation of secondary crystalline phase on top of glass surface). The XRR curve was collected from 0.02 to 4.95 (two theta) with a step size of 0.1 using six different attenuation settings at different range of angle. The XDS was collected at two angles of 0.8 and 1.4 $^{o}$ with a unanimous step size of 0.01 (low angle: from 0.02 to 0.78 $^{o}$; high angle: from 0.04 to 1.36 $^{o}$) at a given attenuation. The refinement of the XRR and XDS data was achieved using Bruker Leptos® (7.7). XRR data from 0.20 to 4.95 $^{o}$ was analyzed in Leptos® to obtain a better fit of the critical angle and thus density values. To constrain the density values fitted in XRR and XDS,

the bulk density (or substrate density in XRR/XDS modeling) of D263 and SLS glass was determined to be 2.51±0.04 and 2.48±0.05 g/cm$^3$ by triplicating Archimedes experiment using a high sensitivity balance (Mettler Toledo MS Digital Balance, Ohio, USA).

In a typical process, the raw XRR data at six different attenuation settings was concatenated by calculating the attenuation factors. The concatenated XRR curve was then inputted into Leptos®, and the bulk density along with the composition of the D263 and SLS glass was added to the materials database in Leptos®. A simulating curve was created by constructing a model with different layers, densities, and thicknesses. The residual between the simulating curve and XRR curve was simulated until it reached a value less than 0.01. During the simulation process, a graded interface instead of sharp interface was allowed but was never found throughout this study. Simulated layers and their densities were obtained using the embedded algorithms in Leptos® [8]:

$$\theta_c = (2\delta)^{1/2} \quad (1)$$

$$\delta = \rho\lambda^2 r_0/2 \quad (2)$$

where $\theta_c$ is the critical angle (incidence angle, where the total reflection of the beam occurs), and $\delta$ is a constant used to describe the refractive index. In equation (2), $\rho$ is the effective electron density, $r_0$ is the Thompson scattering length, and $\lambda$ is the wavelength of the incident X-ray beam. Thus, equation (1) and (2) was primarily used to obtain the density values in XRR simulation. To model the thickness and roughness of the layers and the substrate, following equation was utilized in Leptos® to model the intensity of reflection [9, 10]:

$$R(\theta) = R_f \left| \int \frac{\partial\rho}{\partial z} \exp(i4\pi(\theta/\lambda)z)dz \right|^2 \quad (3)$$

where $R_f$ is the Fresnel reflectivity, θ is the incident angle, and ∂p/∂z is the normal derivative of density. The ∂p/∂z is dependent on the number of layers, thickness of each layer and the corresponding interface roughness between layers. The Kiesig fringes, or so-called oscillations, were used to define the thickness of a certain layer. The roughness values obtained from the modeling of XRR were complimentarily characterized with XDS. Parameters obtained from XRR simulation was used to help constrain the simulation of XDS curves. XDS simulation fits the roughness and its distribution using distorted wave born approximation (DWBA) [9, 10]:

$$g(\boldsymbol{r}, \boldsymbol{r}') = g(R) = < [z(r) - z(r + R)]^2 >= 2\sigma^2 - 2C(R) \quad (4)$$

where g(**r, r**') is the mean-square surface fluctuation between ***r***' and ***r***, z is the surface profile amplitude in the vertical direction, δ is the roughness, and C(R) is the heigh-height correlation [9, 10]. The C(R) is modeled in XDS simulation to obtain Hurst exponent and correlation length for a complimentary description of roughness and its spatial distribution. Simulated parameters from XDS were then used to remodel the XRR data until both XRR and XDS simulations reached to close agreement. Basically, the XDS data was particularly useful in determining the roughness (e.g. equation (4)), its spatial distribution, and identifying the correctness of the model used to simulate XRR curves.

**2.3 X-ray photoelectron spectroscopy**

Chemical composition as well as local chemical environment of the pristine or corroded flat panel glasses (SLS as float glass, and D263 as down draw glass) was analyzed with a PHI Quantera Scanning X-ray photoelectron Microprobe (XPS). The XPS data sets were collected with Al Kα X-rays (monochromatic, beam size=100 μm) at an output power of 26.2 watts and a take-off angle of 45°, with an electron energy of

1486.6 eV. Survey scans were performed with a pass energy of 140 eV and a step size of 0.5 eV to gain qualitative information such as peak identification and peak position. A beam dwelling time of ~100 ms/step was applied to all survey scans. Peaks identified in all survey scans were used to adjust high resolution scan binding energy range, pass energy (26 eV) and dwell time (~ 1 s/step). The beam dwell time as well as number of sweeps (3 sweeps for $Zn_{2p3/2}$, $Ti_{2p}$ and $Mg_{2s}$; 1 sweep for all the other acquired peaks) for each scanning range was adjusted to yield a signal-to-noise ratio (S/N) of >100:1 with exception of $Zn_{2p3/2}$, $Ti_{2p}$ and $Mg_{2s}$ (S/N is > 50:1). The analyzed area for each spectrum was ~1-2 mm in diameter. The depth of analysis of XPS is dependent on the inelastic free mean path of a given element in the solid and the take-off angle. The inelastic free mean path of elements in a similar glass was used [11] to calculate the depth analysis using the following relationship [12]:

$$d_{analysis} = 3\lambda \sin\theta \quad (5)$$

where λ is the inelastic free mean path of a given element, θ is the take-off angle. Thus, the depth of analysis in this study is approximately 6.8 nm (the take-off was set to $45^{o}$ due to the geometrical limitation of PHI Quantera, where $50^{o}$ is the maximum take-off angle). It needs to be noted that the depth of analysis represents the averaged depth of outermost surface (roughness features included).

The standard deviation (STD) of peak position was measured by acquiring O1s spectra from five different spots on an identical sample. The STD is assigned to be 0.1 eV since calculated value is less than the step size of ~ 0.1 eV. All acquired spectra were corrected using adventitious alkyl carbon peak located at 284.6 eV. To quantify the

chemical composition of the corroded glass surface, high-resolution scans were performed at three different locations on the sample surface. Relative sensitivity factors of all elements ($RSF_{Si}$ = 1, $RSF_{Al}$ = 0.5, $RSF_{B}$ = 0.4, $RSF_{Zn}$ = 6.5, $RSF_{Mg}$ = 0.5, $RSF_{K}$ = 3.2, $RSF_{Ti}$ = 2.7, $RSF_{Na}$ = 3.0, $RSF_{Ca}$ = 5.3 and $RSF_{O}$ = 1.8) were derived from hi-resolution XPS scans of fresh air-fractured surface of an aluminoborosilicate glass surface, assuming that the glass fracture surface was identical to the bulk glass composition measured using spectrochemical analysis (ICP-AES digestion). The RSF of Ti and Zn is obtained from measurement of high purity zinc and titanium bearing oxides. XPS data qualitative and quantitative analyses were performed on CasaXPS® software. Area of each hi-resolution scan XPS peaks was fitted by the Shirley-model after automated background subtraction.

## 3. Results and discussion

### 3.1 Identification of a textured, dense silica gel and a de-alkalized glass without density-gradient

Figure IV.1a, b, and c shows the XRR, XDS at low angle, and XDS at high angle of pristine SLS and D263 glass, respectively. The low residual (less than $1e^{-2}$) fittings of the XRR curve and two XDS curves was achieved assuming there was no layer (with a different density) on top of the bulk glass. Similarly, the same simple substrate (bulk glass) model was used to fit the XRR curve and XDS curves of pristine D263 glass as shown in Figure IV.1d, e, and f.

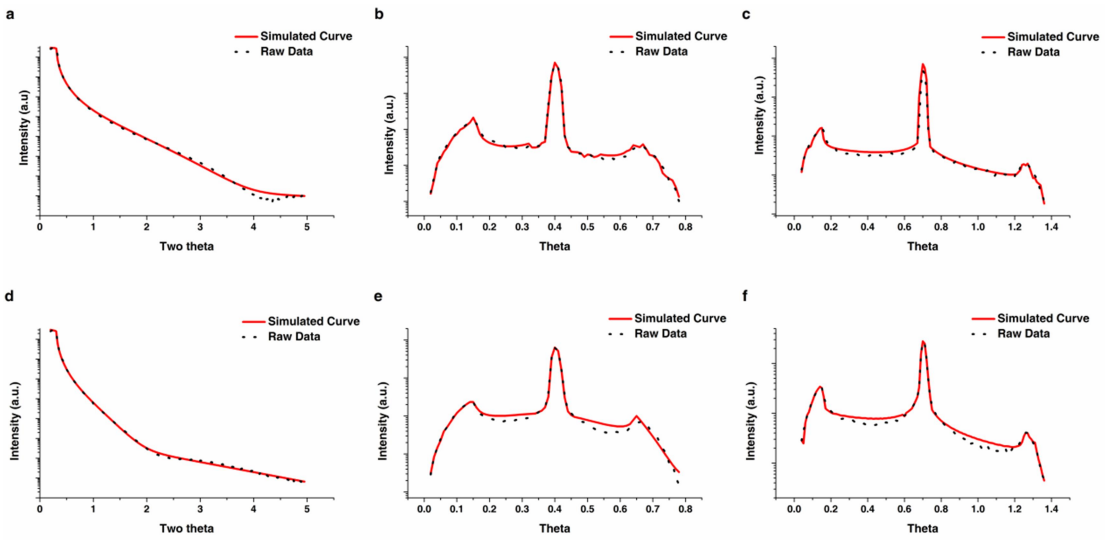


Figure IV.1 (a) XRR curve, (b) XDS curve at low angle, (c) XDS curve at high angle of pristine SLS glass; (d) XRR curve, (e) XDS curve at low angle, and (f) XDS curve at high angle of pristine D263 glass.

The roughness of the SLS and D263 glass substrate was 0.89±0.05 nm and 1.50±0.04 nm, respectively. The roughness values of both pristine glass surface was close to the reported values of glass melt surfaces varying from 0.1 nm to 1.4 nm, as measured using surface profilometry techniques such as AFM [13]. The differences in roughness values of glass surfaces from various manufacturers or vendors could well be a result of production variabilities, different packaging, and storing strategies [13]. XDS is particularly sensitive to the surface roughness, and thus the roughness values generated from the simulation of XRR and XDS was convincing. In addition, the simulated density values of pristine SLS and D263 glass substrate was 2.43±0.01 and 2.53±0.00 g/cm$^3$, respectively. The density values were in close agreement with the densities measured by triplicating the Archimedes experiment (SLS: 2.48±0.05 g/cm$^3$; D263: 2.51±0.04 g/cm$^3$). Thus, it was believed that the simple substrate model for simulating the XRR and XDS curve of pristine SLS and D263 glass was appropriate. For SLS samples reacted for 1 to 100 hours

and D263 samples reacted for 1 to 200 hours, a two layer (altered glass and pristine glass substrate) construction was used to model the XRR and XDS data (see Appendix D). However, the fittings were either invalid (exceeding error limit) or had a large residual (more than 3e-1) when a diffusion zone or density-gradient was allowed between the altered glass and glass substrate. Also, a density gradient often features variations on the width of the Kiesig fringes [14]. Throughout this study, no evidence of density-gradient was found through direct observation or simulation. Under the two-layer construction, the density of the altered glass layer remained stable at 2.28±0.04 and 2.02±0.03 g/cm$^3$ for SLS and D263 sample, respectively. The density values of the altered glass layer were smaller compared to their bulk glass counterparts, close to the values reported for de-alkalized glasses [4, 15]. Further evidence of XPS data (see Table 4.3) suggested that its composition was depleted in modifier ions compared to the bulk glass. Thus, the altered glass layer (layer#1 in simulation) was referred as the de-alkalized glass in this study.

Table 4.3 Composition of the Outermost Surface of SLS and D263 Glass Samples after Different Reaction Times. Errors are Generated by Probing Five Different Spots on an Identical Glass Sample

| Chemical Composition (SLS) | | | | | | |
|---|---|---|---|---|---|---|
| **Sample** | **Na** | **Ca** | **Mg** | **Si** | **O** | **Total** |
| 0 hour | 7.7 | 1.8 | 0.9 | 22.6 | 66.9 | 100.0 |
| 1 hour | 6.5 | 1.7 | 0.2 | 23.5 | 68.1 | 100.0 |
| 5 hours | 4.8 | 1.7 | 0.0 | 24.7 | 68.8 | 100.0 |
| 10 hours | 3.8 | 1.5 | 0.0 | 24.9 | 69.8 | 100.0 |
| 50 hours | 3.1 | 1.3 | 0.0 | 24.1 | 71.5 | 100.0 |
| 100 hours | 2.6 | 1.1 | 0.0 | 27.8 | 68.5 | 100.0 |
| 150 hours | 0.1 | 0.1 | 0.0 | 28.4 | 71.4 | 100.0 |
| 200 hours | 0.1 | 0.1 | 0.0 | 29.6 | 70.2 | 100.0 |
| 250 hours | 0.1 | 0.1 | 0.0 | 32.8 | 67.0 | 100.0 |
| **Error** | **0.5** | **0.3** | **0.2** | **0.8** | **1.5** | |

| Chemical Composition (D263) | | | | | | | | | | |
|---|---|---|---|---|---|---|---|---|---|---|
| **Sample** | **Na** | **K** | **Mg** | **Zn** | **Ti** | **Al** | **B** | **Si** | **O** | **Total** |
| 0 hour | 5.6 | 5.7 | 0.2 | 1.1 | 0.7 | 3.6 | 4.4 | 16.4 | 62.2 | 100.0 |
| 1 hour | 4.6 | 4.8 | 0.0 | 1.0 | 0.6 | 4.0 | 2.3 | 17.8 | 64.9 | 100.0 |
| 5 hours | 3.6 | 4.0 | 0.0 | 1.0 | 0.5 | 3.7 | 0.0 | 18.4 | 68.9 | 100.0 |
| 10 hours | 3.0 | 3.6 | 0.0 | 0.8 | 0.2 | 4.1 | 0.0 | 19.7 | 68.6 | 100.0 |
| 50 hours | 0.9 | 1.5 | 0.0 | 0.4 | 0.1 | 3.7 | 0.0 | 21.0 | 72.4 | 100.0 |
| 100 hours | 0.7 | 0.6 | 0.0 | 0.2 | 0.0 | 3.2 | 0.0 | 19.4 | 75.9 | 100.0 |
| 150 hours | 0.0 | 0.3 | 0.0 | 0.0 | 0.0 | 0.4 | 0.0 | 29.6 | 69.7 | 100.0 |
| 200 hours | 0.0 | 0.3 | 0.0 | 0.0 | 0.0 | 0.5 | 0.0 | 30.0 | 69.2 | 100.0 |
| 250 hours | 0.0 | 0.2 | 0.0 | 0.0 | 0.0 | 0.3 | 0.0 | 30.5 | 69.0 | 100.0 |
| **Error** | **0.5** | **0.3** | **0.3** | **0.5** | **0.3** | **0.2** | **0.6** | **1.2** | **1.7** | |

The roughness of the de-alkalized glass layer increased with time for SLS and D263 sample under the two layer construction. However, the interface roughness between the pristine glass substrate and the de-alkalized glass remained at 0.74±0.08 and 1.47±0.14 nm for SLS and D263 sample, respectively. The interface roughness was identical to the roughness of pristine glass surface within the measured error. Given the linearity of the ionic exchange process (or termed as interdiffusion) as a function of time, it was reasonable that the roughness of pristine glass surface was retained at the interface with the progression of the experiment (linear progression of de-alkalization towards the pristine substrate). The linearity of ionic exchange, as in conventional solution analysis of leachates [16], is reflected by the linear relationship between the concentration of released modifier ions and time [16, 17].

After being reacted for 150 and 250 hours, a dense layer was observed for SLS and D263 sample, respectively. The fittings of XRR and XDS curves for SLS and D263 samples are shown in Figure IV.2a-c and Figure IV.2d-f, respectively. As shown through Figure IV.2a to f, the fittings based on the three layer construction (dense layer, de-alkalized glass and pristine substrate), which also rendered low fitting residuals. The density of the dense layer was 2.65±0.04 and 2.78±0.05 g/cm$^3$ for SLS and D263 samples, and the density values of these two dense layers were close to the theoretical density of

amorphous silica ~2.65 g/cm$^3$. The XPS data (eg. Table 4.3) also agreed that the dense layer was a dense silica layer (depletion of modifier ions and enrichment of Si comparing to bulk composition). However, the XPS data (150 hours for SLS, and 250 hours for D263) showed a low concentration of modifier ions (~ 0.1 atm% of Na and Ca for SLS; ~0.2 atm% of K for D263), which can be a result of the fact that layer thickness (1.49±0.37 nm for SLS; 1.48±0.13 nm for D263) is shallower than the depth of analysis of XPS (~6.8 nm). Thus, the modifier ions observed in XPS data were contributed from the signals picked up from the de-alkalized glass layer.

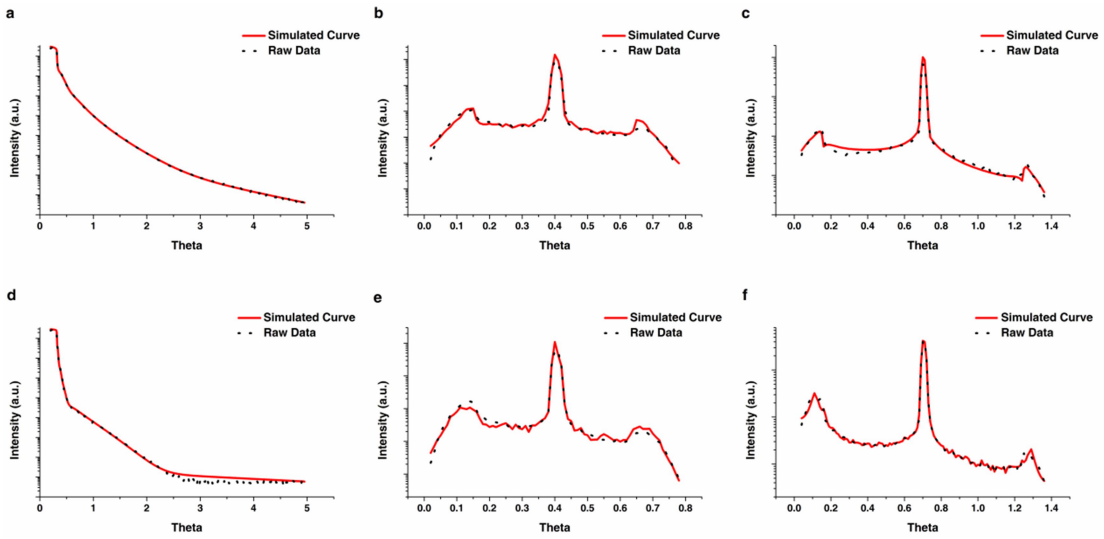


Figure IV.2 (a) XRR curve, (b) XDS curve at low angle, (c) XDS curve at high angle of SLS glass reacted in dilute HCl for 150 hours; (d) XRR curve, (e) XDS curve at low angle, and (f) XDS curve at high angle of D263 glass reacted in dilute HCl for 250 hours. Both sets of curves were the first observation of a dense silica layer.

In order to conceptualize the corrosion mechanism underlying the SLS and D263 test, the roughness (RMS), density, and thickness of layers (de-alkalized glass as layer#1; dense silica layer as layer#2) as a function of time was plotted in Figure IV.3 a-d (fitted parameters are detailed in Appendix D). As shown in Figure IV.3a and IV.3c, the

roughness of the de-alkalized glass (layer#1) showed a non-linear relationship with time and stopped roughening when the dense silica layer was formed (150 hours for SLS; 250 hours for D263). The density of the de-alkalized glass and glass substrate remained stable throughout the experiment for D263 samples.

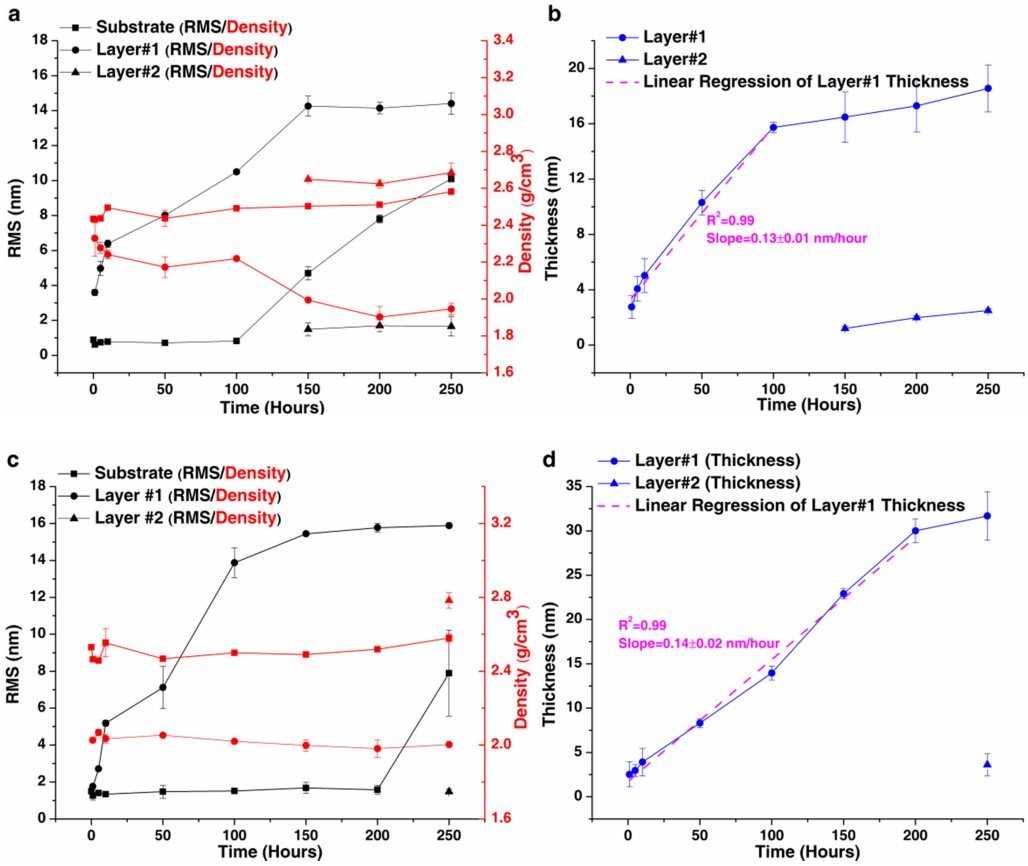


Figure IV.3 (a) roughness and density of layers as a function of reaction time glass, (b) thickness of layers as a function of reaction time for test performed on SLS glass; (c) roughness and density of layers as a function of reaction time glass, (d) thickness of layers as a function of reaction time for test performed on D263 glass. Lines are guides to eyes in exception of the dashed lines used to fit layer#1 thickness prior to the formation of layer#2.

However, a drop of density values from 2.28±0.04 to 1.99±0.01 g/cm$^3$ was observed for SLS samples after 150 hours of reaction, and the density of de-alkalized glass remained stable at 1.99±0.01 g/cm$^3$ from 150 hours to 250 hours. This drop of

density observed in de-alkalized SLS glass layer resulted from the void spaces of roughness features created by the large interface roughness (from 4.70±0.37 to 10.10±0.01 nm after 150 hours). For both sets of experiments, the formation of dense silica layer was accompanied by a sudden increase of interface roughness of (de-alkalized glass and glass substrate). Such sudden increase of de-alkalized glass and substrate interface roughness along with the highly texturized dense silica layer (roughness value close to the thickness) can be accounted for the observed porosities (or void spaces) found in altered glass outer rims as reported elsewhere [5, 6]. Particularly, the de-alkalized glass layer thickness as a function of reaction time (e.g. Figure IV.3b and 4.3d) was studied for its linearity under two layer constructions. Prior to the formation of the dense silica layer, the de-alkalized glass layer thickness (SLS and D263) showed a linear relationship (with $R^2$>0.99) with the reaction time and followed the linear behavior of ionic exchange process as mentioned previously. The growth rate of de-alkalized layer thickness, as under the two layer constructions, was 0.13±0.01 and 0.14±0.02 nm/hour for SLS and D263 samples, respectively. The identical growth rate of de-alkalized glass layer thickness suggested a close ionic exchange rate in both glasses under same solution environment. After the formation of the dense silica layer, the thickness of de-alkalized glass grew at a lowered rate. However, it needs to be pointed out that the fitting of XRR and XDS data greatly relies on the constructed model, and a set of XRR and XDS data can be fitted in multiple methods. The method used, as for this study, was based on the understanding/assumptions associated with two known corrosion mechanisms (the hydration coupled ion exchange process, and the interfacial dissolution and reprecipitation process); also, XPS data was used to minimize the possible errors

associated with the XRR and XDS fitting. A more appropriate approach could be used to accurately determine some of the fitting parameters, e.g. roughness of top surface can be obtained using AFM and density of each layer can be quantified using neutron depth profile with proper standardization.

To visualize the general mechanism of SLS and D263 glass corrosion, the cross-section of the sample is schematically shown in Figure IV.4. The mechanism is summarized as follows: 1) the glass surface formed a de-alkalized glass layer upon contact with aqueous solution, and the thickness of the de-alkalized layer grows linearly with time and roughness increases with time; 2) after forming a highly texturized dense silica layer, the de-alkalized glass thickness grows in a lowered rate; 3) the interfaces between each layers are highly texturized (roughness close to layer thickness) to hold porosity; 4) there is no density gradient between each layers, thus the sharpened interface suggests a corrosion mechanism contradicting the diffusion coupled hydration and leaching of modifier ions.

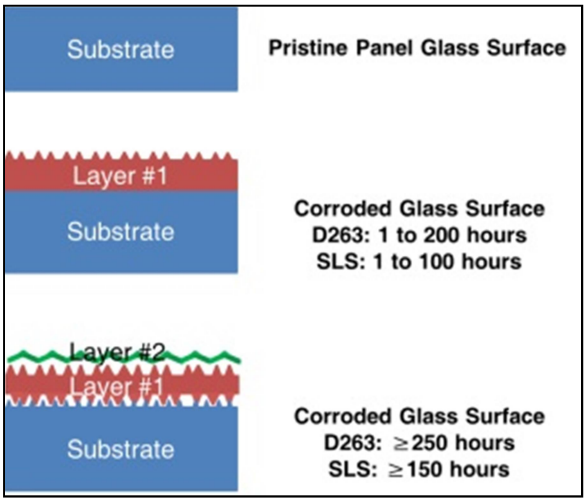


Figure IV.4 The schematic of the cross-section of the SLS and D263 sample at different time and construction of layers.

Thus, the observations on the simulation of XRR and XDS of two types of corroded glass most likely favor the interfacial dissolution and reprecipitation mechanism of silica layer formation.

To further investigate the corresponding mechanism to the phenomenological observations, the modeling was performed on the origin of dense silica layer to answer the question that "where Si in silica layer came from? solution or de-alkalized glass?".

### 3.2 Determination and simulation of the origin of the dense silica layer

The formation of dense silica layer (e.g. Figure IV.4) can lower the growth rate of the de-alkalized glass layer thickness (e.g. Figure IV.3b and 4.3d) due to the limited transportation of water [5, 6]. However, such role of dense silica layer as a diffusion barrier should not change the linearity of the growth of the de-alkalized glass layer thickness versus time. Thus, the thickness of the de-alkalized glass was calculated with two different origins of dense silica layer assuming that the dense silica layer was from either bulk solution or recondensation of the de-alkalized glass. The D263 samples only formed the dense silica layer after 250 hours of reaction, and thus were not used to model the origin of the dense silica layer. Under the assumption that the dense silica layer was originated from the bulk solution, the as-measured thickness of the de-alkalized glass using XRR/XDS should be the "actual" thicknesses. Under such assumption, the growing thickness of de-alkalized glass and the formation/growth of the dense silica layer are two different phenomenological events that have no effect on the thickness of each layer.

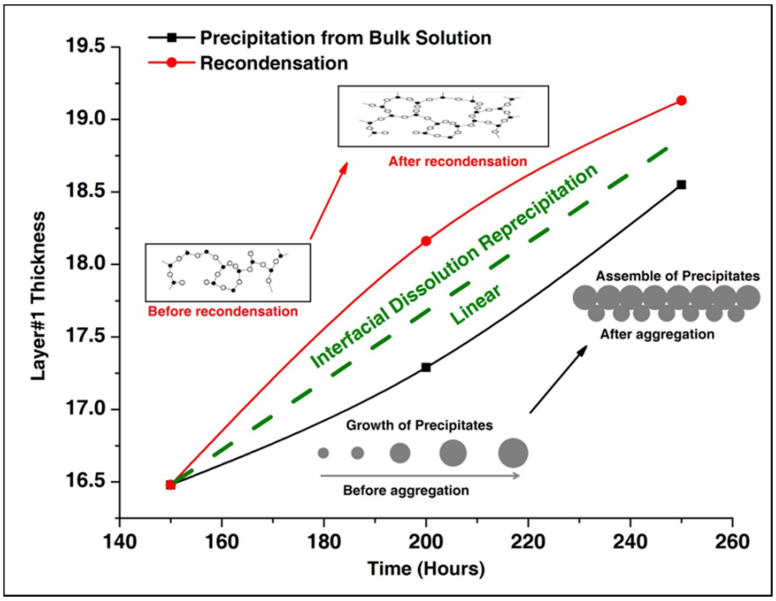


Figure IV.5 The modeled thickness of de-alkalized glass as a function of time under two different mechanisms. Red line: recondensation of the de-alkalized glass; black line: precipitation of dense silica layer from bulk solution. The insets show the corresponding mechanism of dense silica layer formation, particularly the recondensation of the de-alkalized glass mechanism is associated with the dense silica layer thickness.

The as-measured de-alkalized glass layer thickness (or the assumption that dense silica gel is from precipitation of bulk solution) is plotted versus time in Figure IV.5. The inset below the curve shows a typical process of $SiO_2$ precipitations from bulk solution and their assembly to be a highly textured dense silica dense layer. The change in the thickness of dense silica layer ($\Delta d_{layer\#2}$) from 150 to 200 hours and 200 hours to 250 hours was 0.78±0.20 and 0.52±0.18 nm, respectively. If assuming that the dense silica layer was formed by the recondensation of de-alkalized glass, the $\Delta d_{layer\#2}$ should be compensated to evaluate the "actual" thickness of the de-alkalized glass. Thus, the following equation based on recondensation of de-alkalized glass and mass balance was used to calculate the compensate values ($\Delta d_{layer\#1}$):

$$\frac{\rho_{layer\#2}}{\rho_{layer\#1}} = \frac{V_{layer\#1}}{V_{layer\#2}} \approx \left(\frac{\Delta d_{layer\#1}}{\Delta d_{layer\#2}}\right)^3 \quad (6)$$

where ρ is the density (g/cm$^3$) measured by XRR, and V is the volume of transformed glass. The calculated $\Delta d_{layer\#1}$ is 0.87±0.22 and 0.58±0.20 nm (errors were calculated from algorithms in error propagation) from 150 to 200 hours and 200 to 250 hours, respectively. The $\Delta d_{layer\#1}$ was added to the as-measured thickness of de-alkalized glass, and then plotted versus time as shown in Figure IV.5. Under this mechanism, glass network was restructured to reach a low chemical affinity state, often a higher density, and thus most thermodynamically stable state. It needs to be pointed out that the propagated errors in Figure IV.5 were not significant compared to the mean value (less than 5%), and thus were not shown. As shown in Figure IV.5, the mechanism of recondensation and bulk solution precipitation both showed a non-linear relationship between the thickness of de-alkalized glass and the reaction time. Thus, the assumed mechanisms shown in Figure IV.5 are unlikely to be reasonable when accounting for the linearity of de-alkalized glass thickness versus time. Given the linearity of the de-alkalized glass thickness (as a process of ionic exchange), it is probable that a linear line placing between both non-linear curves in Figure IV.5 represents the "real" mechanism of silica layer formation. However, the "actual" position of the dashed linear line (thickness versus time) cannot be calculated or modeled to the author's best knowledge. The origin of the dense silica layer is most likely to be an interfacial dissolution and reprecipitation controlled mechanism given the involvement of Si dissolution from de-alkalized glass (decrease in relative thickness) and reprecipitation of dissolved Si from supersaturated thin solution layer [6]. The interfacial dissolution and reprecipitation mechanism can be treated as an event phenomenologically containing the features from

both assumed processes (recondensation and precipitation). Thus, the position of "real" de-alkalized glass thickness versus time should be placed in between the two non-linear lines. In this study, a preliminary effort towards the origin of dense silica gel through coupled modeling of XRR/XDS data was shown. The errors and assumptions associated with this approach of determining the origin of silica layer can be better evaluated using in-situ characterization techniques, but are not further discussed in this study.

### 3.3 Comparison between modeled and measured surface composition

The density of de-alkalized glass was calculated from the composition measured using XPS. In order to perform such calculation, the thickness of the layer must be larger than the depth of analysis ~6.8 nm of XPS. When the de-alkalized glass is textured (roughness larger than the measured thickness), the thickness of the de-alkalized was assumed to be two times the roughness value (amplitude of thickness in the vertical direction) [18]. Thus, SLS samples from 1 hour to 150 hours and D263 samples from 5 to 200 hours were used to perform the density calculations. The calculations of density based on glass composition were developed using the database of commercially available SciGlass® software and are detailed in [19]. However, the outermost surface composition of SLS glass after 100 hours and D263 glass after 150 hours was over the composition limit. For SLS glass, the XPS calculated density values varied at 2.38±0.23 g/cm$^3$ from 1 hour to 50 hours. The mean XPS calculated the density of the de-alkalized SLS glass was slightly higher than the mean XRR measured density of 2.28±0.04 g/cm$^3$. Similarly, the XPS calculated density (2.13±0.08 g/cm$^3$) of the de-alkalized D263 glass was slightly higher than the XRR measured density (2.02±0.03 g/cm$^3$). It appears that such minor

discrepancy in measured and calculated density values could be the fact that XPS is not capable of accounting for the void spaces between roughness features.

Since XPS cannot account for the void spaces between roughness features, with its capability of picking up chemical information at given depth of analysis ~ 6.8 nm, the XPS composition of the outermost surface after forming a dense silica gel was modeled. Figure IV.6 is the schematic presentation of the calculation model used for the outermost surface composition. As shown in Figure IV.6, the lower bound of percentage signals from dense silica layer was assigned as the $d_{layer\#2}/d_{analysis}$, and the upper bound of percentage signals from dense silica layer was assigned as the $2*RMS_{layer\#2}/d_{analysis}$ to account for the vertical amplitude of the silica layer [18].

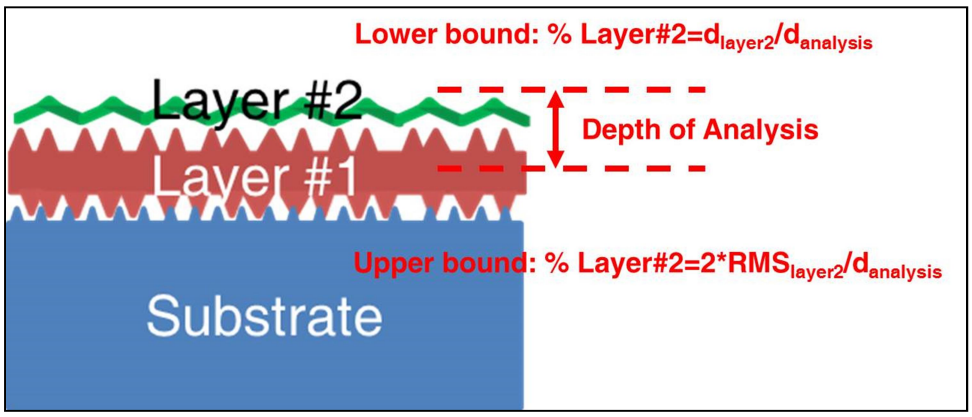


Figure IV.6 The schematics of a corroded glass sample cross-section after forming a textured (zigzag shaped) dense silica gel.

When the dense silica layer thickness is higher than the roughness, the upper bound was assigned as $d_{layer\#2}/d_{analysis}$. Also, the composition of the de-alkalized glass was assumed as the composition prior to the formation of dense silica layer (100 hours XPS composition for SLS; 200 hours XPS composition for D263). Generally, the modeled composition is:

$$C_i = \frac{d_{layer\#2}}{d_{analysis}} * C_{i,SiO2} + \left(1 - \frac{d_{layer\#2}}{d_{analysis}}\right) * C_{i,de-alkalized\ glass} \quad (7)$$

where C$i$ is the concentration of element $i$. As shown in Table 4.4, the measured composition using XPS falls into the calculated range of compositions for both sets of samples.

Table 4.4 The Calculated Composition Range of the Outermost Glass Surface after the Formation of Dense Silica Layer Occurs

| Sample | SLS 150 hours | | SLS 200 hours | | SLS 250 Hours | | D263 250 Hours | |
|---|---|---|---|---|---|---|---|---|
| Lower Bound | **Na** | 2.1 | **Na** | 1.8 | **Na** | 1.6 | **K** | 0.2 |
| | **Ca** | 0.9 | **Ca** | 0.8 | **Ca** | 0.7 | **Al** | 0.3 |
| | **Si** | 28.8 | **Si** | 29.4 | **Si** | 29.8 | **Si** | 31.4 |
| | **O** | 68.2 | **O** | 68.0 | **O** | 67.8 | **O** | 68.2 |
| Upper Bound | **Na** | 1.2 | **Na** | 1.0 | **Na** | 0.3 | **K** | 0.1 |
| | **Ca** | 0.5 | **Ca** | 0.4 | **Ca** | 0.1 | **Al** | 0.1 |
| | **Si** | 30.8 | **Si** | 31.1 | **Si** | 32.7 | **Si** | 33.0 |
| | **O** | 67.5 | **O** | 67.4 | **O** | 66.9 | **O** | 66.8 |

Thus, it was convincing that the conclusions and simulation results obtained from the XRR/XDS data were appropriate based on the agreement between measured and calculated densities and compositions.

## Conclusions

For the first time, synchrotron radiated XRR/XDS was coupled to measure the aqueous corroded flat panel glasses. The results of the best XRR/XDS fittings suggested that a textured dense silica layer was probably formed on top of the de-alkalized glass with a rough, sharp, and non-density gradient interface. The constructed models from XRR/XDS results provided new evidence in favor of the interfacial dissolution and reprecipitation mechanism to account for the textured silica layer observed in laboratory experiments and historical glasses. In addition, the de-alkalized glass thickness after

silica layer formation was calculated through the surface controlled growing de-alkalized glass. The attempts were made to identify the origin of the silica layer, and the results were more likely in support of the interfacial dissolution and reprecipitation mechanism rather than the hydration coupled ion exchange mechanism. Finally, the close agreement between measured and calculated densities, compositions suggested that the conclusion being made was appropriate under the proposed models.

**References**


1. R. Hellmann, S. Cotte, E. Cadel, S. Malladi, L. S. Karlsson, S. Lozano-Perez, M. Cabié, and A. Seyeux, "Nanometre-scale evidence for interfacial dissolution–reprecipitation control of silicate glass corrosion," *Nature Materials,* 14[3] 307-11 (2015).
2. R. C. Ewing, "Nuclear waste forms for actinides," *Proceedings of the National Academy of Sciences,* 96[7] 3432-39 (1999).
3. D. Rebiscoul, A. Van der Lee, F. Rieutord, F. Né, O. Spalla, A. El-Mansouri, P. Frugier, A. Ayral, and S. Gin, "Morphological evolution of alteration layers formed during nuclear glass alteration: new evidence of a gel as a diffusive barrier," *Journal of Nuclear Materials,* 326[1] 9-18 (2004).
4. D. Rebiscoul, A. Van Der Lee, P. Frugier, A. Ayral, and S. Gin, "X-ray reflectometry characterization of SON 68 glass alteration films," *Journal of Non-Crystalline Solids,* 325[1] 113-23 (2003).
5. T. Geisler, A. Janssen, D. Scheiter, T. Stephan, J. Berndt, and A. Putnis, "Aqueous corrosion of borosilicate glass under acidic conditions: a new corrosion mechanism," *Journal of Non-Crystalline Solids,* 356[28] 1458-65 (2010).

6. T. Geisler, T. Nagel, M. R. Kilburn, A. Janssen, J. P. Icenhower, R. O. Fonseca, M. Grange, and A. A. Nemchin, "The mechanism of borosilicate glass corrosion revisited," *Geochimica et Cosmochimica Acta,* 158 112-29 (2015).

7. S. Gin, L. Neill, M. Fournier, P. Frugier, T. Ducasse, M. Tribet, A. Abdelouas, B. Parruzot, J. Neeway, and N. Wall, "The controversial role of inter-diffusion in glass alteration," *Chemical Geology,* 440 115-23 (2016).

8. A. Gibaud and S. Hazra, "X-ray reflectivity and diffuse scattering," *CURRENT SCIENCE-BANGALORE-,* 78[12] 1467-77 (2000).

9. R. G. Newton, "Scattering theory of waves and particles.″ Springer Science & Business Media, (2013).

10. P. S. Pershan and J. Als-Nielsen, "X-ray reflectivity from the surface of a liquid crystal: Surface structure and absolute value of critical fluctuations," *Physical Review Letters,* 52[9] 759 (1984).

11. J. P. Hamilton, S. L. Brantley, C. G. Pantano, L. J. Criscenti, and J. D. Kubicki, "Dissolution of nepheline, jadeite and albite glasses: toward better models for aluminosilicate dissolution," *Geochimica et Cosmochimica Acta,* 65[21] 3683-702 (2001).

12. M. Seah and W. Dench, "Quantitative electron spectroscopy of surfaces: a standard data base for electron inelastic mean free paths in solids," *Surface and Interface Analysis,* 1[1] 2-11 (1979).

13. N. Mellott, S. Brantley, J. Hamilton, and C. Pantano, "Evaluation of surface preparation methods for glass," *Surface and Interface Analysis,* 31[5] 362-68 (2001).

14. K. C. Fairley, D. R. Merrill, K. N. Woods, J. Ditto, C. Xu, R. P. Oleksak, T. Gustafsson, D. W. Johnson, E. L. Garfunkel, and G. S. Herman, "Non-uniform Composition Profiles in Inorganic Thin Films from Aqueous Solutions," *ACS Applied Materials & Interfaces,* 8[1] 667-72 (2015).

15. K. Ferrand, A. Abdelouas, and B. Grambow, "Water diffusion in the simulated French nuclear waste glass SON 68 contacting silica rich solutions: Experimental and modeling," *Journal of Nuclear Materials,* 355[1] 54-67 (2006).

16. P. Frugier, S. Gin, Y. Minet, T. Chave, B. Bonin, N. Godon, J.-E. Lartigue, P. Jollivet, A. Ayral, and L. De Windt, "SON68 nuclear glass dissolution kinetics: Current state of knowledge and basis of the new GRAAL model," *Journal of Nuclear Materials,* 380[1] 8-21 (2008).

17. P. Van Iseghem, M. Aertsens, K. Lemmens, S. Gin, D. Deneele, B. Grambow, P. McGrail, D. Strachan, G. Wicks, and T. McMenamin, "GLAMOR: A critical evaluation of the dissolution mechanisms of high-level waste glasses in conditions of relevance for geological disposal," (2007).

18. T. Yamanaka, S. J. Fang, H.-C. Lin, J. P. Snyder, and C. R. Helms, "Correlation between inversion layer mobility and surface roughness measured by AFM," *IEEE Electron Device Letters,* 17[4] 178-80 (1996).

19. A. Fluegel, "Global Model for Calculating Room-Temperature Glass Density from the Composition," *Journal of the American Ceramic Society,* 90[8] 2622-25 (2007).

# APPENDIX A. SURFACE ROUGHNESS MEASUREMENTS USING POWER SPECTRUM DENSITY ANALYSIS WITH ENHANCED SPATIAL CORRELATION LENGTH

## Introduction

The properties of thin films can be significantly altered by the roughness of the substrate [1, 2, 3]. Thus, characterization and quality control of substrate roughness is crucial for film-based devices to reach their desired electrical, thermal, optical, mechanical, and chemical function. Rauofi [4] reported that the roughness of indium tin oxide (ITO) substrates alters the transparency, electrical conductivity, quantum efficiency, and topography of ZnO nanostructured thin films, while Castro-Rodriguez *et. al.* [5] found that the residual strain in CdS thin films varies as a function of the roughness of the ITO substrate. Fang *et. al.* [6] reported that nanoscale roughness (< 1 nm) can alter the gate oxide reliability of $SiO_2$ thin films deposited on Si substrates, and further affect the morphological features of deposited $SiO_2$ films at both the nanoscale and microscale ( > 1 μm). Several other authors [7, 8] also reported that the breakdown strength ($Q_{BD}$) of multilayer film-based devices is associated with the interface roughness between successive layers. However, those reported phenomena were based on roughness values specified using average roughness (Ra) or root-mean-square (RMS) roughness, which do not provide any information with respect to the spatial distribution of roughness or the scale dependency of roughness. More importantly, failure to fully understand the effect of roughness on material properties may lead to catastrophes when those materials are used in critical applications such as astronautics, defense technology, and nuclear technology [9,

[10, 11]. Likewise, comprehensive understanding of the roughness of materials and roughness related phenomena is beneficial to the development of biomaterial applications, novel energy harvesting devices, nuclear/high energy physics devices, etc. [9, 10, 11].

Roughness measurements are routinely made using X-ray reflectometry (XRR), light scattering, profilometry, laser interferometry, confocal scanning laser microscopy, and atomic force microscopy (AFM). Specifically, accurate measurements of roughness can be achieved with AFM due to its wide dynamic range, high lateral resolution and low vertical noise [6]. Since its introduction by Binnig, Quate and Gerber [12], the AFM community has enjoyed significant progress in the collection and analysis of images for quantifying the morphology and spatial characteristics of surfaces [13]. However, the impact of surface roughness on materials properties remains a rather controversial issue, in particular due to poorly-established methodologies of acquiring as well as analyzing AFM images.

AFM measured roughness is often represented by simple statistical parameters such as average roughness, root-mean-square (RMS) roughness, peak-to-valley (P/V) ratio, etc. In these statistical values, 250,000 (*x-, y-, z-)* coordinate data points (using 512 X 512 pixels$^2$ resolution for example) are represented by a single number. However, the resultant roughness value can be identical for drastically different surface morphologies [14, 15]. Such convergence of roughness values from different surface morphologies is caused by the fact that these roughness algorithms are insensitive to lateral structures. It has been established that roughness values based on statistical theories are greatly dependent on the sampling interval, scanning scale, randomness of measured areas as well as specifics of each measuring methods. Thus, it becomes crucial to understand and

evaluate the methodologies of acquiring as well as analyzing AFM images that can be most suitable for describing surface roughness comprehensively. Specifically, questions like “what scanning scale should be used” and “how scanning scale can affect roughness values” are not fully understood.

In addition to the above-mentioned analyses, AFM images can be analyzed using methods of fractal geometry such as power spectral density (PSD) functions to provide topographical parameters (equivalent roughness, fractal dimension, and Hurst exponent), which are relatively independent of the resolution of the instrument, scanning cycles performed and scanning scale used. The algorithm of the PSD function, in contrast to conventional statistical analysis, has proven successes in the description of various complex surface geometries as well as in understanding the effects of surface morphology on the properties of material systems [16]. By applying PSD functions, AFM images can be represented by spectral strength densities over a wide range of different spatial frequencies, therefore roughness data acquired from different spatial frequency regions can be directly compared.

The goal of this work is to demonstrate a method of AFM spectral analysis to obtain repeatable roughness values due to the enhancement of measured spatial correlation length. Detailed PSD function analysis is clarified with detailed theoretical definitions and performed on a commercially available roughness standard. This study is of particular importance to the accurate measurement of roughness by evaluating the fitting methods and algorithms of power density spectrum analysis. Enhanced correlation length was observed to maximize the accuracy of spectral fitting as well as the reproducibility of roughness value. Applying PSD to the control of surface topography

during materials processing is beyond the scope of this work and is well discussed elsewhere [17, 18, 19, 20]. However, it is worth noting that the application of PSD spectral analysis on patterned materials (eg. > 100s nm patterns produced by soft lithography) is excluded from the discussion of this work.

## Experimental Methods

### Atomic force microscopy

Surface morphology of a commercially available silicon nitride coated roughness standard (Ted Pella Product No. TCI-BudgetSensor TipCheck) was imaged and quantified using a Digital Instruments Nanoscope Dimension 3100 multimode atomic force microscope (AFM) equipped with $Ar/N_2$ gas floating table in Tapping Mode ®. Antimony doped silicon probes (Bruker TESP, cantilever length of 125 μm) with nominal tip radius of curvature of 8nm, nominal spring constant of 42 N/m and resonance frequency range of ~230-410 KHz were used for all measurements. Images were captured at a scanning rate of 1.0 Hz and resolution of 512 pixels × 512 pixels. Ten 1 μm × 1 μm, 5 μm × 5 μm and 10 μm × 10 μm scans were performed at same probing area with minor drift caused by the lateral force interaction between tip and roughness standard. In order to ensure the consistent force interaction between tip and surface at different scan scales, the setpoint amplitude was set at 1.38 mV. For each scan size, a new tip was used to limit the tip geometrical effect on the roughness values. Upon initiation of the measurement of each scan size, the drive amplitude and drive frequency of the tip was adjusted quickly minimizing any wear effects on the tip geometry.

The Bruker Nanoscope Analysis software (Version.1.50sr3) was used throughout this study for processing AFM images, obtaining RMS roughness and Ra. The RMS roughness and Ra was calculated and averaged from 10 acquired images of identical scan size. Line by line flattening and 3rd order plane fitting were performed on each image prior to analysis. The 3rd order plane fitting calculates a third-order polynomial fit to the image in the *x*- and *y*-directions and subtracts the polynomial fit from the image, removing tilt and S-shaped bow [21]. Thus, the 3rd order plane fitting removes the artifacts caused by the curvature of piezoelectric material, thermal drift, background vibration noise or lateral forces. Flattening removes the vertical offsets between scan lines through the calculation of a least-squares polynomial fit for a scan line, and the subtraction of the polynomial fit from original scan line.

**Theory**

Root-mean-square roughness (RMS) is defined as the root-mean-square average of height deviations from the mean elevation plane, calculated from the relative height of each pixel in the image

$$RMS = \sqrt{\left(\frac{z_1^2 + z_2^2 + \cdots + z_N^2}{N}\right)} \quad (1)$$

where $z_i$ equals the deviation in height from the mean plane height and N equals the number of points measured (value equals to scan resolution). However, RMS is only sensitive to vertical signals and ignores horizontal structures. Fortunately, PSD functions evaluate surface roughness as the spread of height deviations from a mean plane, and the

lateral distribution/distance over which the height variation occurs. The PSD function is applied to the 3-dimensional AFM surface profile as [22]:

$$S_2(f_x + f_y) = \frac{1}{L^2} * \left[\sum_{m=1}^{N} \sum_{n=1}^{N} Z_{mn} e^{-e\pi i \Delta L (f_x m + f_y n)} (\Delta L)^2\right]^2 \qquad (2)$$

where $S_2$ denotes the 2-D isotropic PSD, $L$ is the lateral scale of scanned surface, $N$ is the 1-D resolution for one direction ($x$ or $y$), $Z_{mn}$ is the profile height at location (m, n), $f_x$ & $f_y$ are the spatial frequencies in the $x$- and $y$- directions and $\Delta L = L/N$ is the distance between two adjacent sampling points [23].

This function is further translated into polar coordinates through spatial frequency and angular averaging (φ)

$$S_2(f) = \frac{1}{2\pi} * \int_0^{2\pi} S_2(f, \varphi)\, d\varphi \qquad (3)$$

Therefore, the PSD function depends only on the frequency of the surface roughness and can be plotted as a 2-D representation. The density of data points in the PSD at a given spatial frequency region is greatly dependent on the scan size and sampling distance. When applying the PSD model, accuracy of the spectral analysis can be affected by the density of the data points, which artificially yields a short correlation length of roughness distribution. Geometrical averaging of PSD functions collected at different spatial frequencies can mitigate this issue. In this work, PSD functions of the same scan number (1$^{st}$ scan of 1 μm, 5 μm and 10 μm) were averaged as:

$$PSD_{combined}(f) = [\prod_{i=1}^{M} PSD_i(f)]^{1/M} \quad (4)$$

where M is the number of scans combined (*e.g.* M=3, in this study). In this work, the scanning is centered at the same area for each scan size. PSD results (1 μm, 5 μm, 10 μm and combined) were then modelled using two different approaches in order to quantify the surface fractal dimension (*D*), Hurst exponent (*H*), and equivalent RMS roughness ($\sigma_{ABC}$). The fractal model was utilized to model the high frequency region (0.1 $nm^{-1}$ to 0.256 $nm^{-1}$) while the k-correlation model was used to model the low-frequency region (0.001 $nm^{-1}$ to 0.03 $nm^{-1}$).

The fractal model [24] is shown below:

$$PSD_{fractal}(f; K, s) = \frac{K}{f^s} \quad (5)$$

where *K* is the spectral strength and *s* is the slope of logarithmic plots (PSD vs spatial frequency) . The fractal dimension, *D*, can be determined as [25, 26]:

$$\begin{aligned} &D = 2, 0 \leq |s| < 1 \\ &D = \frac{1}{2}(8 - s) = 1/2[8 - (E + 2H)] \\ &D = 1, 3 < |s| \end{aligned} \quad (6)$$

where s is defined as s=E+2H where E is the Euclidean dimension of the Fourier transform used (E=2), and H is the roughness scaling factor or Hurst exponent, which represents the logarithmic spatial increase of the saturated roughness: $w_{sat} \propto L^H$ or $\Delta z \propto \Delta x^H$.

From Eq.6, the fractal dimension (D) can be used to derive the Hurst exponent (H), through the relation [27, 28]:

$$H = 3 - D \tag{7}$$

The k-correlation, or ABC model, was also applied to the PSD function (Eq. 8) in order to further quantify the surface topography, as given by [29]:

$$PSD_{ABC} = \frac{A}{(1+B^2 f^2)^{\frac{C+1}{2}}} \tag{8}$$

Experimental PSD profiles were fitted through this model to derive parameters A, B and C. The equivalent RMS roughness $\sigma_{ABC}$ can be then defined from these three parameters as follows:

$$\sigma_{ABC}^2 = \frac{2\pi A}{B^2(C-1)} \quad . \tag{9}$$

**Results and Discussion**

Figure A.1a-c displays representative AFM images of the TipCheck roughness standard captured at 1 µm, 5 µm and 10 µm scan scale, respectively. Consistency of image quality as well as image features was maintained, as the tapping drive frequency and amplitude were kept constant. Figure A.1a-c suggest the topographical feature of the roughness standard is homogeneous in terms of feature size and height of the positive relief features. Figure A.1b and A.1c shows stripe-like negative relief features with stripe-like shape, attributed to mechanical scratching possibly occurred during sample cleaning and handling. Figure A.1b and A.1c exhibits a larger spatial description of topography than the 1 µm scan as shown in Figure A.1a. Topographies obtained from larger scan scales results in a significant loss of image resolution (*e.g.* decrease from 250,000 pixel$^2$/µm$^2$ of 1 µm scan to 2,500 pixel$^2$/µm$^2$ of 10 µm scan), and such loss of resolution is usually reflected by variations of roughness as a function of scan scale. However, the effect of scan scales, termed "scaling effect," can be eliminated by the use of PSD analysis given the fact that the PSD is a function of distribution of height values and spatial frequencies (*e.g.* Eq 2).

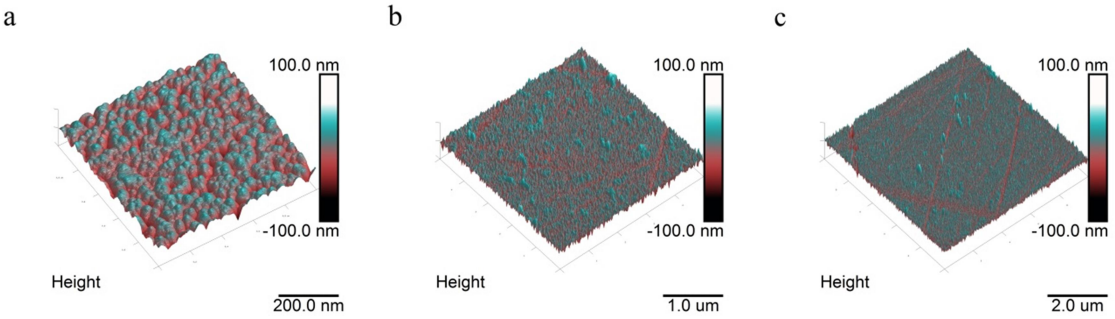


Figure A.1 Exemplary AFM images of TipCheck standard captured at a) 1 µm scan scale, b) 5 µm scan scale and c) 10 µm scan scale.

Figure A.2a-c shows the PSD profiles of 1 μm, 5 μm and 10 μm scans at different scanning cycles. Within each scan, the PSD profiles at different scan cycles overlap with no observable difference, indicating the quality of scan was well maintained. The spatial frequency of the "knee" of the PSD profiles is located at ~ $10^1$ $\mu m^{-1}$ for the 1 μm, 5 μm and 10 μm scans. The spatial frequency regions of the PSD profiles shrinks from 1 $\mu m^{-1}$~256 $\mu m^{-1}$ to 0.1 $\mu m^{-1}$~25.6 $\mu m^{-1}$ after the scan size was increased from 1 μm to 10 μm, respectively. This increase of scan size results in an increased data density at the given frequency region (*e.g.* 0.1 to 25.6 $\mu m^{-1}$), due to the fact that the numbers of data point remain the same. When applying the k-correlation model for obtaining the equivalent RMS and correlation length, the density of PSD profile data points near the "knee" is crucial for fitting accuracy. Therefore, maximizing the density of data (i.e. increase of the scan scale) at designated spatial frequencies is of great importance. However, in extreme cases k-correlation model fitting of a 40 μm scan PSD profile in the region of 0.025 $\mu m^{-1}$~6.40 $\mu m^{-1}$ can hardly be performed given the limitations of the lateral scan size, possible artifacts and bending of cantilever arms due to abrupt changes of the *z*-axis. More importantly, longer wavelength scans can sacrifice the ability to quantify spatial distributions of roughness, which are obtained from short wavelength scans.

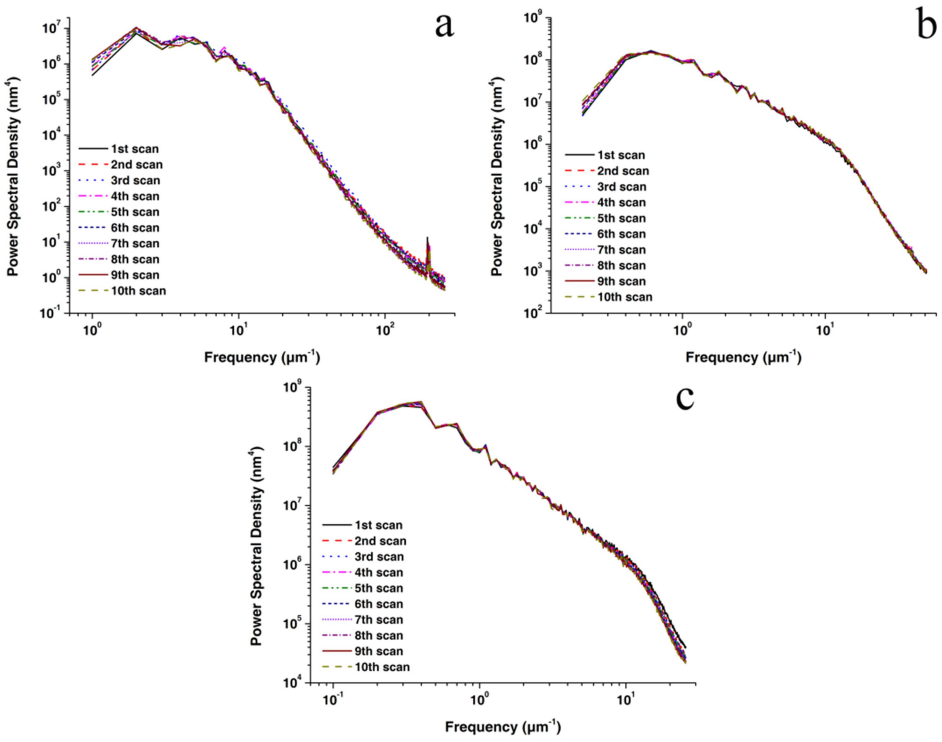


Figure A.2 PSD profiles of a) 1 μm scan scale, b) 5 μm scan scale and c) 10 μm scan scale at different scan cycles.

Longer wavelength scans enable the fitting of the k-correlation model (the "knee" region) with a significantly higher data density. Short wavelength scan profiles are capable of defining the fractal geometrical parameters not achievable from large scale scans. Therefore, an accurate, complimentary and optimized fitting of the PSD profile must consist of signals from both short and long wavelength scans. The PSD plot shown in Fig A.3 is the result of overlapping (0.1 to 25.6 $\mu m^{-1}$) scans from 1 μm, 5 μm and 10 μm and then transforming into a combined PSD profile using product rule (*e.g.* Eq.4), as shown in Figure A.3b.

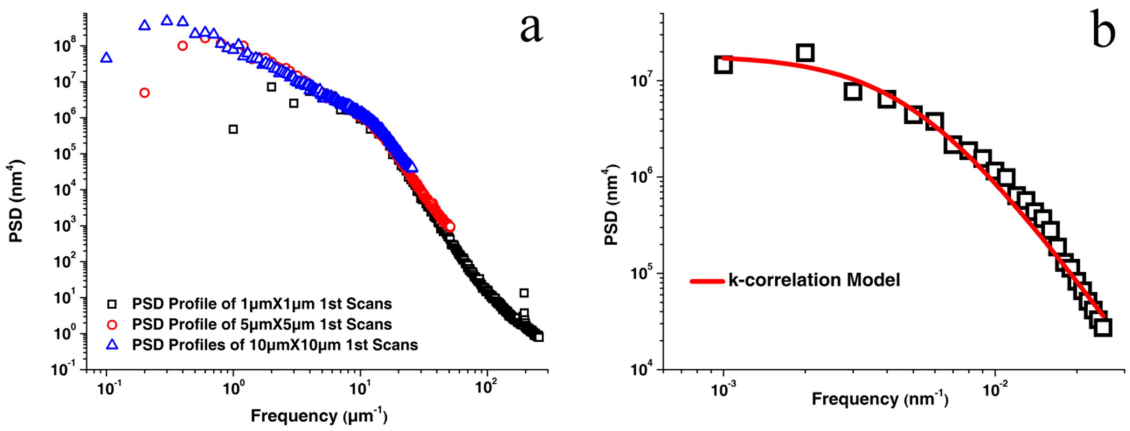


Figure A.3 PSD profile of a) 1st scan performed at 1 μm, 5 μm and 10 μm scan scale, b) algorithm combined 1st scan of 1 μm, 5 μm and 10 μm scan scale with k-correlation model fitting.

To make direct comparisons between each scan size, the k-correlation derived roughness as well as the correlation length was used to fit PSD profiles in the spatial frequency region of 0.001 $nm^{-1}$~0.0256 $nm^{-1}$ as shown in Figure 4a-c. Additionally, the fractal model was used to model the 1 μm scan, in the spatial frequency region of 0.1 $nm^{-1}$~0.256 $nm^{-1}$, and to extract the fractal dimension and Hurst exponent (Figure A.4a). Fitting coefficients for 1 μm scans are listed in Table A.1. As shown in Table A.1, fractal dimension values are in the range of 2.51~2.56 while Hurst exponents of 10 cycles of 1 μm scans are in the range of 0.44~0.49; no direct relation was found between scan number and Hurst exponent. All Hurst exponents of all 1 μm scans are below 0.5, indicating the homogeneous spatial distribution of roughness; a Hurst value within the range of 0~0.5 indicates a spatial frequency series with continuous alternating features of high and low values (homogeneous distribution) while a Hurst exponent value between 0.5 and 1 represents a spatial frequency series with positive autocorrelation, suggesting abrupt value changes (inhomogeneous distribution) [30, 31, 32]. No observable trend of

correlation length (in the range of 68.5 nm ~ 125.9 nm) and equivalent RMS (10.1 nm ~ 12.0 nm) as a function of scan number are identified, as shown in Table A.1. A deviation of 25.1 % of correlation length from the mean value (80.8 ± 20.3 nm) indicates a relatively large error due to the lack of data points at the spatial frequency of 0.001 $nm^{-1}$~0.0256 $nm^{-1}$.

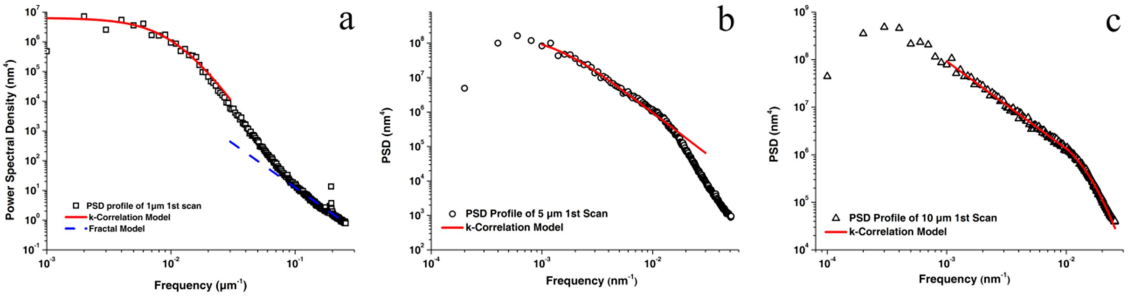


Figure A.4 Exemplary fittings of 1st scan PSD profiles at a) 1 μm scan scale (fractal model and k-correlation model), b) 5 μm scan scale (k-correlation model) and c) 10 μm scan scale (k-correlation model).

Tables A.2 and A.3 show the k-correlation fitting coefficients of the PSD spectra acquired at 5 μm and 10 μm scan size, respectively. The value of correlation length from 5 μm and 10 μm scans show no observable trend as a function of scan number, and the value varies slightly (< 10%) with scan number. Equivalent RMS values of the 5 μm scans increases to a stable range between 11.1 and 11.2 nm after the first 3 scan cycles, and a deviation of 0.1 nm from the mean value is treated as a propagated error as 0.1 nm does not hold any physical significance (*e.g.* oxygen atom size=0.155 nm).

However, an identifiable decrease of equivalent RMS roughness was found for the 10 μm scans after 10 scans (from 10.8 nm to 9.5 nm), which was concluded to be a result of contaminant agglomeration on the tip as evidenced by SEM (not shown here).

Agglomeration of contaminants was only found on the tip used for 10 μm scans. After increasing the scan scale to 10 μm, the correlation length was significantly lowered to 42.0 ~ 57.7 nm. As mentioned earlier, fluctuation of signals obtained at larger scan scales is likely responsible for the decrease in correlation length.

As proposed, combined PSD profiles from all 3 different scan sizes can greatly increase the data density of PSD profiles near the low frequency "knee" region, and thus the correlation length at a given spatial frequency region can be increased. An increased correlation length indicates a more stabilized roughness value and homogeneity of distribution at a given spatial frequency region. This results in an accurate roughness evaluation. As shown in Table A.4, the correlation length of the combined PSD profiles (198.8 nm ~ 292.6 nm) is significantly higher than that of PSD profiles from other scan sizes (10 μm: 42.0 nm~ 57.7 nm; 5 μm: 128.5 nm ~ 143.3 nm; 1 μm: 68.5 nm ~ 125.9 nm). This is additional evidence that increasing the density of data in PSD profiles at the low frequency regions can enhance the correlation length. Equivalent RMS of 10 scan cycles from combined PSD profiles is 13.2±0.3 nm (or with 1.9% roughness deviation) and can be considered as equivalent in value. Equivalent PSD profile combination methods have been applied by various authors [23, 33] for ease in k-correlation model fitting; however, these reports did not show the increase in correlation length or discuss the physical meanings behind the combination algorithm.

In order to verify the consistency between each type of roughness value, roughness values gathered from the k-correlation model fitting of the PSDs and root-

mean-square (RMS) were compared by the Table A.1 through A.4. The equivalent RMS follows the changing trend of apparent RMS and average roughness as a function of scanning cycles (*e.g.* Table 1 through 4). Such relationship between equivalent RMS, apparent RMS and average roughness is also well reported elsewhere [34].

## Conclusions

In this work, a method to enhance the spatial correlation length resulting in roughness measurements with improved accuracy was shown. The approach involves increasing the density of PSD profiles in the frequency region of 0.001 $nm^{-1}$ to 0.03 $nm^{-1}$, resulting in a more complete description of the vertical and spatial distribution of roughness of a surface. In order to increase the PSD profile density over this region, product rule combination was used for different scan sizes in overlapped spatial frequency regions. The variation of equivalent RMS as a function of scanning cycles follows the variations observed for RMS roughness at all measured scan scales. Thus, the equivalent RMS (with an enhanced spatial correlation length) is more definitive in describing surface roughness as well as the variations of surface roughness.

## References

1. J. Takadoum and H. H. Bennani, "Influence of substrate roughness and coating thickness on adhesion, friction and wear of TiN films," *Surface and Coatings Technology,* 96[2–3] 272-82 (1997).

2. M. Mellali, P. Fauchais, and A. Grimaud, "Influence of substrate roughness and temperature on the adhesion/cohesion of alumina coatings," *Surface and Coatings Technology,* 81[2–3] 275-86 (1996).

3. Y. Y. Wang, C. J. Li, and A. Ohmori, "Influence of substrate roughness on the bonding mechanisms of high velocity oxy-fuel sprayed coatings," *Thin Solid Films,* 485[1–2] 141-47 (2005).

4. D. Raoufi, "Fractal analyses of ITO thin films: A study based on power spectral density," *Physica B: Condensed Matter,* 405[1] 451-55 (2010).

5. R. Castro-Rodríguez, A. I. Oliva, V. Sosa, F. Caballero-Briones, and J. L. Peña, "Effect of indium tin oxide substrate roughness on the morphology, structural and optical properties of CdS thin films," *Applied Surface Science,* 161[3–4] 340-46 (2000).

6. S. J. Fang, S. Haplepete, W. Chen, C. R. Helms, and H. Edwards, "Analyzing atomic force microscopy images using spectral methods," *Journal of Applied Physics,* 82[12] 5891-98 (1997).

7. M. Depas, M. Heynes, T. Nigam, K. Kenis, H. Sprey, R. Wilhelm, A. Crossley, C. Sofield, and D. Graf, "Electrochem. Soc." in. PV-96-1, 352, 1996.

8. M. Kimura, J. Mitsuhashi, and H. Koyama, "Si/SiO2 interface states and neutral oxide traps induced by surface microroughness," *Journal of Applied Physics,* 77[4] 1569-75 (1995).

9. P. Dash, P. Mallick, H. Rath, A. Tripathi, J. Prakash, D. K. Avasthi, S. Mazumder, S. Varma, P. V. Satyam, and N. C. Mishra, "Surface roughness and power spectral density study of SHI irradiated ultra-thin gold films," *Applied Surface Science,* 256[2] 558-61 (2009).

10. T. Itoh and N. Yamauchi, "Surface morphology characterization of pentacene thin film and its substrate with under-layers by power spectral density using fast Fourier transform algorithms," *Applied Surface Science,* 253[14] 6196-202 (2007).

11. L. Vepsäläinen, P. Stenberg, P. Pääkkönen, M. Kuittinen, M. Suvanto, and T. A. Pakkanen, "Roughness analysis for textured surfaces over several orders of magnitudes," *Applied Surface Science,* 284[0] 222-28 (2013).

12. G. Binnig, C. F. Quate, and C. Gerber, "Atomic Force Microscope," *Physical Review Letters,* 56[9] 930-33 (1986).

13. C. F. Quate, "The AFM as a tool for surface imaging," *Surface Science,* 299–300[0] 980-95 (1994).

14. S. D. Halepete, H. C. Lin, S. J. Fang, and C. R. Helms, "Analyzing Atomic Force Micrographs Using Spectral Methods," *MRS Online Proceedings Library,* 386 null-null (1995).

15. S. J. Fang, W. Chen, T. Yamanaka, and C. R. Helms, "Comparison of Si surface roughness measured by atomic force microscopy and ellipsometry," *Applied Physics Letters,* 68[20] 2837-39 (1996).

16. P. Pfeifer, Y. J. Wu, M. W. Cole, and J. Krim, "Multilayer adsorption on a fractally rough surface," *Physical Review Letters,* 62[17] 1997-2000 (1989).

17. T. Yamanaka, S. J. Fang, L. Heng-Chih, J. P. Snyder, and C. R. Helms, "Correlation between inversion layer mobility and surface roughness measured by AFM," *Electron Device Letters, IEEE,* 17[4] 178-80 (1996).

18. S. Fang, H. Lin, J. Snyder, C. Helms, and T. Yamanaka, "A quantitative correlation between inversion layer mobility and Si/SiO2 interface roughness," *Proc.*

*Electrochemical Society, the Physics and Chemistry of SiO2 and the SiSiO2 Interface* 96-1 (1996).

19. H.-C. Lin, J.-F. Ying, T. Yamanaka, S. J. Fang, and C. R. Helms, "Analysis of interface roughness's effect on metal–oxide–semiconductor Fowler-Nordheim tunneling behavior using atomic force microscope images," *Journal of Vacuum Science & Technology A,* 15[3] 790-96 (1997).
20. S. J. Fang, W. Chen, T. Yamanaka, and C. R. Helms, "Influence of Interface Roughness on Silicon Oxide Thickness Measured by Ellipsometry," *Journal of The Electrochemical Society,* 144[8] L231-L33 (1997).
21. N. P. Mellott and C. G. Pantano, "A Mechanism of Corrosion-Induced Roughening of Glass Surfaces," *International Journal of Applied Glass Science,* 4[3] 274-79 (2013).
22. J. Ferré-Borrull, A. Duparré, and E. Quesnel, "Procedure to characterize microroughness of optical thin films: application to ion-beam-sputtered vacuum-ultraviolet coatings," *Appl. Opt.,* 40[13] 2190-99 (2001).
23. M. Senthilkumar, N. K. Sahoo, S. Thakur, and R. B. Tokas, "Characterization of microroughness parameters in gadolinium oxide thin films: A study based on extended power spectral density analyses," *Applied Surface Science,* 252[5] 1608-19 (2005).
24. E. L. Church, "Fractal surface finish," *Appl. Opt.,* 27[8] 1518-26 (1988).
25. B. B. Mandelbrot, "The fractal geometry of nature,″ Vol. 173. Macmillan, (1983).

26. M. B. Khamesee, Y. Kurosaki, M. Matsui, and K. Murai, "Nanofractal analysis of material surfaces using atomic force microscopy," *Materials Transactions,* 45[2] 469-78 (2004).

27. J. C. Russ, "Fractal surfaces.″ Springer, (1994).

28. D. Ph, B. Bouffakhreddine, C. Amra, O. Vatel, E. Andre, R. Galindo, and F. Salvan, "Quantitative Microroughness Analysis down to the Nanometer Scale," *EPL (Europhysics Letters),* 22[9] 717 (1993).

29. E. L. Church, P. Z. Takacs, and T. A. Leonard, "The Prediction Of BRDFs From Surface Profile Measurements,″ pp. 136-50. Vol. 1165.

30. J. Bassingthwaighte and G. Raymond, "Evaluating rescaled range analysis for time series," *Ann Biomed Eng,* 22[4] 432-44 (1994).

31. Y. Zhang and S. Sundararajan, "Generating random surfaces with desired autocorrelation length," *Applied Physics Letters,* 88[14] - (2006).

32. A. V. Novak and V. R. Novak, "Roughness of amorphous, polycrystalline and hemispherical-grained silicon films," *Tech. Phys. Lett.,* 39[10] 858-61 (2013).

33. H. Inoue, A. Masuno, K. Ishibashi, H. Tawarayama, Y. Zhang, F. Utsuno, K. Koya, A. Fujinoki, and H. Kawazoe, "Surface characterization of silica glass substrates treated by atomic hydrogen," *Materials Characterization,* 86[0] 283-89 (2013).

34. A. G. Khurshudov, K. Kato, and H. Koide, "Wear of the AFM diamond tip sliding against silicon," *Wear,* 203–204[0] 22-27 (1997).

Table A.1 Fitting Coefficients of PSD Spectra of 1 μm Scans

| # of scan | Fractal Model | | k-Correlation Model | | | | |
|---|---|---|---|---|---|---|---|
| | D | H | A ($10^5$nm) | B (nm) | C | Equivalent RMS (nm) | Apparent RMS (nm) |
| 1st | 2.52 | 0.48 | 63.8 | 89.92 | 4.96 | 11.11 | 8.89 |
| 2nd | 2.55 | 0.45 | 83.1 | 118.24 | 3.82 | 11.44 | 8.79 |
| 3rd | 2.55 | 0.45 | 76.7 | 86.21 | 5.47 | 11.96 | 9.66 |
| 4th | 2.54 | 0.46 | 75.9 | 85.66 | 5.87 | 11.48 | 9.08 |
| 5th | 2.51 | 0.49 | 73.7 | 98.26 | 4.75 | 11.23 | 8.85 |
| 6th | 2.54 | 0.46 | 50.3 | 77.81 | 5.91 | 10.24 | 8.56 |
| 7th | 2.55 | 0.45 | 63.4 | 68.49 | 8.43 | 10.62 | 8.61 |
| 8th | 2.53 | 0.47 | 97.8 | 125.86 | 3.96 | 11.38 | 8.57 |
| 9th | 2.53 | 0.47 | 61.3 | 72.85 | 7.56 | 10.45 | 8.44 |
| 10th | 2.56 | 0.44 | 55.9 | 64.38 | 9.22 | 10.09 | 8.10 |

Table A.2 Fitting Coefficients of PSD Spectra of 5 μm Scans

| # of scan | k-Correlation Model | | | |
|---|---|---|---|---|
| | A ($10^5$nm) | B (nm) | C | Equivalent RMS (nm) |
| 1st Scan | 97 | 129.51 | 4.37 | 10.32 |
| 2nd Scan | 115 | 137.74 | 4.21 | 10.84 |
| 3rd Scan | 120 | 141.39 | 4.10 | 10.97 |
| 4th Scan | 125 | 139.92 | 4.19 | 11.13 |
| 5th Scan | 127 | 143.25 | 4.10 | 11.13 |
| 6th Scan | 121 | 134.64 | 4.31 | 11.17 |
| 7th Scan | 126 | 140.08 | 4.18 | 11.17 |
| 8th Scan | 128 | 140.52 | 4.19 | 11.21 |
| 9th Scan | 115 | 128.55 | 4.44 | 11.18 |
| 10th Scan | 116 | 128.51 | 4.47 | 11.20 |

Table A.3 Fitting Coefficients of PSD Spectra of 10 μm Scans

| # of scan | k-Correlation Model | | | |
|---|---|---|---|---|
| | A ($10^5$nm) | B (nm) | C | Equivalent RMS (nm) |
| 1st Scan | 49.5 | 57.65 | 8.92 | 10.80 |
| 2nd Scan | 47.4 | 55.03 | 9.94 | 10.42 |
| 3rd Scan | 40.3 | 46.98 | 12.27 | 10.03 |
| 4th Scan | 42.4 | 51.03 | 11.26 | 9.92 |
| 5th Scan | 37.9 | 44.04 | 13.51 | 9.84 |
| 6th Scan | 43.4 | 52.29 | 11.07 | 9.88 |
| 7th Scan | 35.9 | 41.99 | 14.91 | 9.53 |
| 8th Scan | 43.3 | 54.69 | 10.65 | 9.65 |
| 9th Scan | 36.3 | 44.26 | 14.08 | 9.38 |
| 10th Scan | 42.9 | 54.56 | 10.85 | 9.52 |

Table A.4 Fitting Coefficients of Combined PSD Spectra

| # of scan | k-Correlation Model | | | |
|---|---|---|---|---|
| | A ($10^5$nm) | B (nm) | C | Equivalent RMS (nm) |
| 1st Scan | 185 | 198.81 | 2.84 | 12.56 |
| 2nd Scan | 213 | 223.19 | 2.58 | 12.97 |
| 3rd Scan | 206 | 218.39 | 2.49 | 13.42 |
| 4th Scan | 228 | 243.31 | 2.32 | 13.48 |
| 5th Scan | 215 | 240.22 | 2.30 | 13.32 |
| 6th Scan | 245 | 255.01 | 2.35 | 13.17 |
| 7th Scan | 246 | 264.14 | 2.25 | 13.23 |
| 8th Scan | 264 | 263.62 | 2.35 | 13.19 |
| 9th Scan | 262 | 282.23 | 2.18 | 13.14 |
| 10th Scan | 261 | 292.61 | 2.10 | 13.10 |

# APPENDIX B. AFM IMAGES AND XPS DEPTH PROFILES OF CORRODED ISG MELT SURFACES AND POLISHED SURFACES

## Materials and Methods

Glasses used in this study were commercially melted by Mo-Sci Corporation, with melting procedures documented in detail in Chapter I and briefly described here. The ISG glasses were batched and melted to yield a nominal weight% composition of 56.2 % $SiO_2$, 17.3 % $B_2O_3$, 12.2 % $Na_2O$, 6.1 $Al_2O_3$, 5.0 % CaO and 2.8 % $ZrO_2$. Initial batch melting was performed in a platinum-rhodium crucible in an electric oven at 1300 $^oC$ for 4 hours. The initial batch of ISG glass was water-quenched, the resultant glass frits & cullet were re-melted twice under the same conditions. The final batch of melted glass was poured into graphite molds to form ingots. The ingots were annealed near Tg at 569 $^oC$ for 6 hours and cooled to room temperature at a rate of 50 $^oC$ per hour. Bulk glass composition was determined by spectrochemical analyses, based on $LiBO_2$ fusion techniques followed by analyte determination using a Perkin-Elmer Optima 5300 inductively coupled plasma atomic emission spectroscopy (ICP-AES).

The ISG glass was cut with a 5 inch Buehler diamond saw blade to 1.0 cm × 1.0 cm × 0.2cm. Compositional equivalent polish and melt ISG glass surfaces were prepared by sequentially polishing and heat treatment respectively, details regarding both surface finishing techniques were discussed in Chapter I. Pulverized melt and polish surface are confirmed to be X-ray amorphous by powder diffraction. All prepared melt surfaces and polish surfaces were kept in vacuum desiccator prior to any analysis or experiments. Corrosion experiments were carried out in a static setup using HDPE wide mouth bottles

(Nalgene) at room temperature (~25 $^{o}$C). The areas of melt surfaces and polish surfaces used in the leaching experiment were calibrated using CAD SA database with an error < 1%. Static corrosion experiment were carried out for 8 time spans (1 day, 3 days, 5 days, 10 days, 15 days, 25 days, 37 days and 45 days) at a glass surface-area-to-solution volume (SA/V) ratio of 10 $m^{-1}$ and with two imposed solutions (3±0.02, de-ionized water). The pH 3 solutions were diluted from 1 M HCl solution. pH value of solutions were measured upon ending of each time span. Two identical samples (melt surface or polish, top surface) were placed in the reacting bottles with the bottoms of glass surfaces covered with 3M diagnostic tape in order to avoid the misleading results from reaction of bottom surface. Bottles were kept static without stirring during leaching experiments, and the bottle caps were sealed with Parafilm. Acquired solutions for each time span were filtered with Millipore non-sterile PTFE membrane solution filter (pore size=0.2 μm) prior to solutions analysis. In addition, air-fractured pristine ISG glass were reacted in identical HCl solutions used in this study to confirm the features found on melt surfaces are not introduced by heat treatment.

Surface morphology of corroded glass surfaces was imaged and quantified using a Digital Instruments Nanoscope Dimension 3100 multimode atomic force microscope (AFM) equipped with $Ar/N_2$ gas floating table in Tapping Mode ®. Antimony doped silicon probes (Bruker TESP, cantilever length of 125 μm) with nominal tip radius of curvature of 8nm, nominal spring constant of 42 N/m and resonance frequency range of ~230-410 KHz was used for all measurements. Images were taken with a scanning rate of 1.0 Hz and resolution of 512 pixels × 512 pixels. Qualitative tip size and shape calibration was performed periodically during measurements using a commercially

available standard (Ted Pella Product No. TCI-BudgetSensor TipCheck). Multiple (10 - 1 μm × 1 μm scans & 2 - 10 μm × 10 μm scans) scans were taken of each sample at different locations on the surface to ensure a large-scale spatial averaging of roughness.

Quantitative sputter profiling was performed on unreacted and reacted samples of particular interests using a Kratos Analytical Axis Ultra X-ray photoelectron spectrometer (XPS). The analysis area of all sputter profiles performed is adjusted to 200 μm in diameter to yield a sputter rate of 1 Å/s. In order to compensate the weak signal caused by relatively small analysis area, the pass energy was adjusted to 80 eV. The sputter rate of the resultant glass surfaces was calibrated using a $SiO_2$ film on Si wafer of known thickness. Relative sensitivity factors of all elements ($RSF_{Si}$=1, $RSF_{Al}$=0.59, $RSF_{B}$=0.50, $RSF_{Zr}$=7.87, $RSF_{Na}$=5.08, $RSF_{Ca}$=5.39 and $RSF_{O}$=2.22) in sputter profiles were derived from 80 eV pass energy XPS scans of fresh air-fractured pristine ISG glass surface.

XPS data qualitative and quantitative analyses were perform on PHI MultiPak V8.0 software, peak position was shifted/calibrated using C1s peak with the peak position at 284.60 eV. Areas of sputter profile XPS peaks were fitted by the Shirley-model after automated background subtraction.

**AFM Images of Corroded Glass Surfaces**

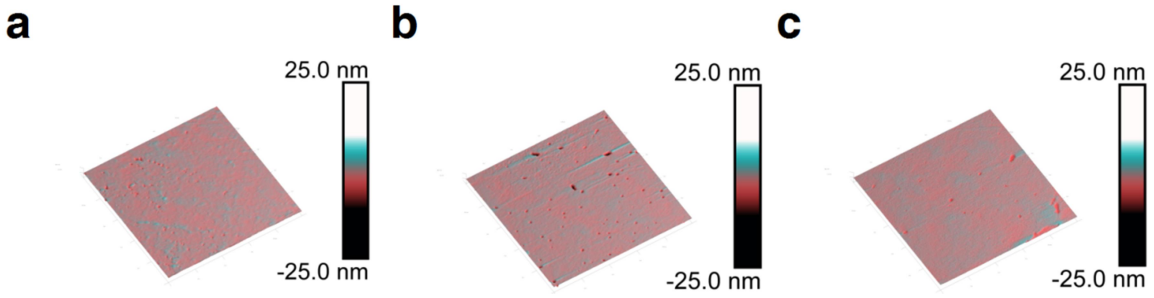


Figure B.1 Atomic force micrographs in 1 μm X 1 μm of ISG glass a) melt surface reacted in acid for 25 days, b) melt surface reacted in neutral for 45 days and c) pristine fracture surface reacted in acid for 15 days; all presented micrographs show clearly identified pits.

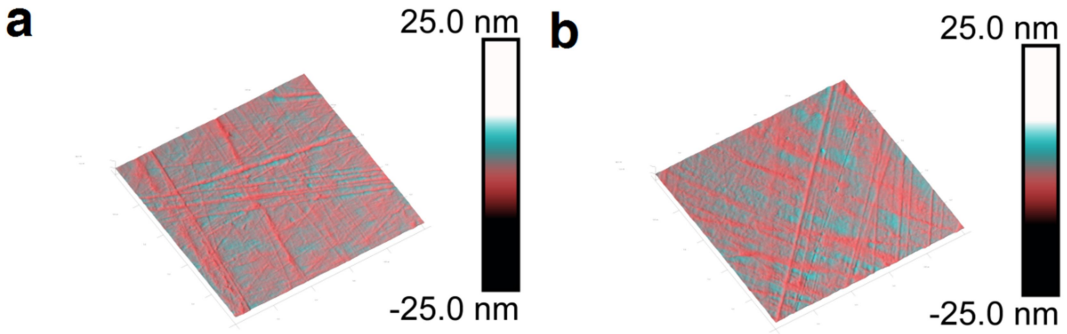


Figure B.2 Atomic force micrograph of a) polished ISG glass surface reacted in acid for 45 days and b) polished ISG glass surface reacted in neutral for 45 days.

## XPS Depth Profiles

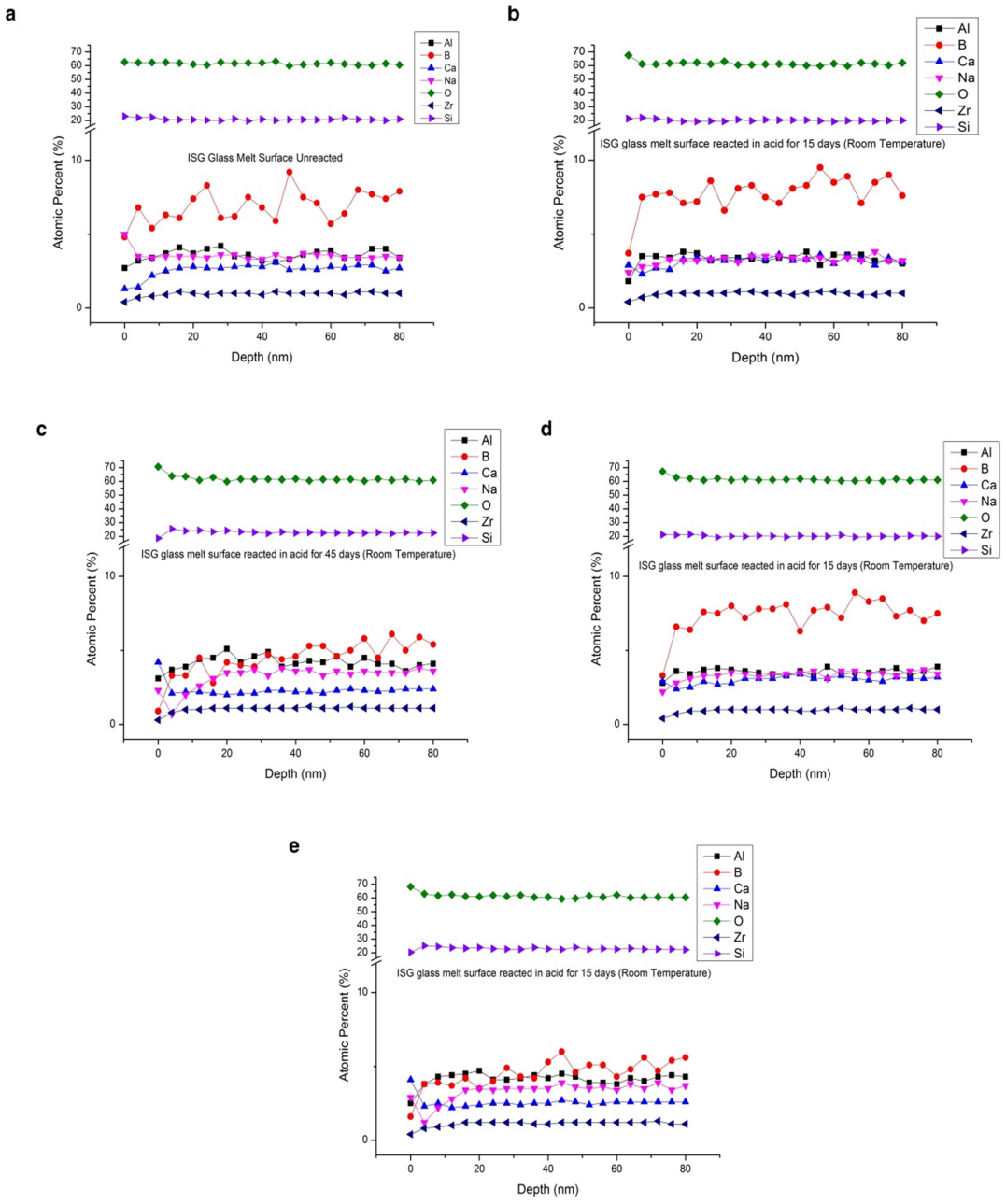


Figure B.3 XPS depth profiling of (a) unreacted melt ISG glass surface, (b) melt ISG glass surface reacted in acid for 15 days, (c) melt ISG glass surface reacted in DI-water for 15 days, (d) melt ISG glass surface reacted in acid for 45 days and (e) melt ISG glass surface reacted in DI-water for 45 days.

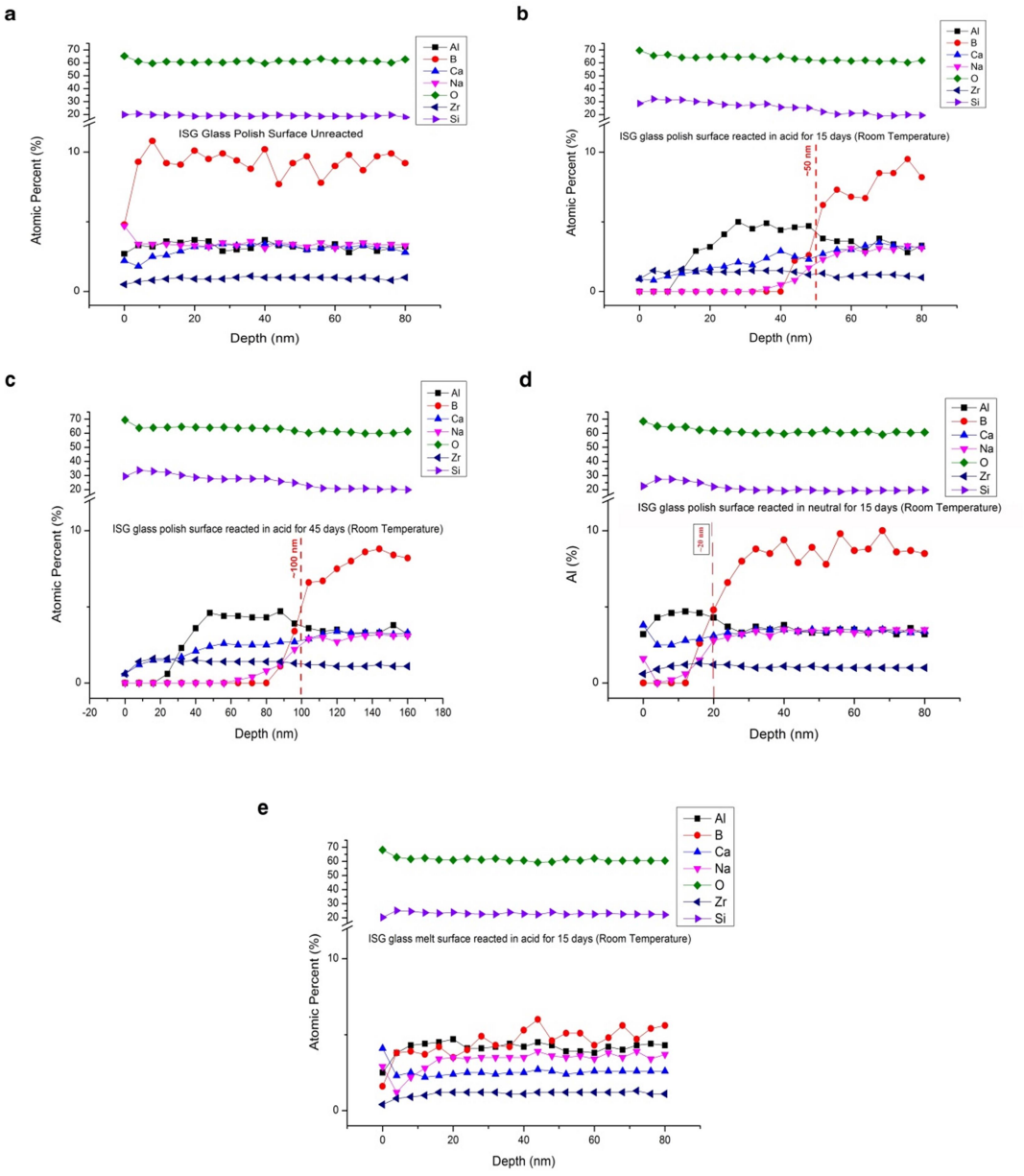


Figure B.4 XPS depth profiling of (a) unreacted polished ISG glass surface, (b) polished ISG glass surface reacted in acid for 15 days, (c) polished ISG glass surface reacted in DI-water for 15 days, (d) polished ISG glass surface reacted in acid for 45 days and (e) polished ISG glass surface reacted in DI-water for 45 days.

# APPENDIX C. DETAILED CHEMICAL COMPOSITION OF REACTED ALUMINOBOROSILICATE GLASS SURFACES IN CHAPTER III

Table C.1 Chemical Composition of Reacted Glass Surfaces in Buffered pH2 Solution

| Glass coupon reacted in pH=2 solution | | | | | | | | | | | | |
|---|---|---|---|---|---|---|---|---|---|---|---|---|
| Element | Bulk | 0 hour | 24 hours | 48 hours | 72 hours | 96 hours | 120 hours | 144 hours | 168 hours | 480 hours | 720 hours | 960 hours |
| O | 57.9 | 64.0 | 66.3 | 68.6 | 69.3 | 66.8 | 68.1 | 67.4 | 68.7 | 67.8 | 68.6 | 69.0 |
| Ca | 2.8 | 4.1 | 1.0 | 0.4 | 0.4 | 1.0 | 0.1 | 0.1 | 0.1 | 0.9 | 0.1 | 0.7 |
| Na | 11.2 | 6.6 | 0.9 | 0.7 | 0.3 | 1.2 | 0.4 | 0.4 | 0.3 | 0.7 | 0.5 | 0.2 |
| K | 0.5 | 2.1 | 2.1 | 1.6 | 1.5 | 1.6 | 0.6 | 0.8 | 0.8 | 0.9 | 0.5 | 1.1 |
| Mg | 1.2 | 2.1 | 0.8 | 0.3 | 0.3 | 0.6 | 0.2 | 0.0 | 0.0 | 0.0 | 0.0 | 0.0 |
| Al | 2.1 | 2.4 | 1.7 | 1.3 | 1.1 | 1.2 | 1.1 | 1.0 | 0.8 | 1.2 | 1.0 | 0.0 |
| B | 4.8 | 1.5 | 0.0 | 0.0 | 0.0 | 0.0 | 0.0 | 0.0 | 0.0 | 0.0 | 0.0 | 0.0 |
| Si | 19.4 | 17.2 | 27.2 | 27.2 | 27.1 | 27.7 | 29.6 | 30.3 | 29.1 | 28.6 | 29.3 | 29.0 |

Table C.2 Chemical Composition of Reacted Glass Surfaces in Buffered pH7 Solution

| Glass coupon reacted in pH=7 solution | | | | | | | | | | | | |
|---|---|---|---|---|---|---|---|---|---|---|---|---|
| Element | Bulk | 0 hour | 24 hours | 36 hours | 48 hours | 60 hours | 72 hours | 84 hours | 96 hours | 480 hours | 720 hours | 960 hours |
| O | 57.9 | 64.0 | 68.2 | 68.1 | 66.9 | 68.8 | 70.7 | 68.6 | 68.2 | 65.9 | 65.7 | 71.2 |
| Ca | 2.8 | 4.1 | 2.0 | 1.7 | 1.6 | 1.8 | 1.8 | 1.7 | 1.7 | 1.3 | 2.0 | 2.1 |
| Na | 11.2 | 6.6 | 0.5 | 0.3 | 0.0 | 0.0 | 0.0 | 0.0 | 0.0 | 0.6 | 0.3 | 0.2 |
| K | 0.5 | 2.1 | 0.0 | 0.0 | 0.0 | 0.0 | 0.0 | 0.0 | 0.0 | 0.4 | 0.0 | 0.0 |
| Mg | 1.2 | 2.1 | 0.0 | 0.0 | 0.0 | 0.0 | 0.0 | 0.0 | 0.0 | 0.0 | 0.0 | 0.0 |
| Al | 2.1 | 2.4 | 5.0 | 4.9 | 5.8 | 5.6 | 5.0 | 5.6 | 5.1 | 7.4 | 15.5 | 14.8 |
| B | 4.8 | 1.5 | 0.7 | 0.6 | 1.3 | 1.1 | 0.8 | 0.0 | 0.0 | 0.0 | 0.0 | 1.0 |
| Si | 19.4 | 17.2 | 23.6 | 24.1 | 23.7 | 22.4 | 21.4 | 23.8 | 24.7 | 24.4 | 16.5 | 10.8 |

Table C.3 Chemical Composition of Reacted Glass Surfaces in Buffered pH10 Solution

| Glass coupon reacted in pH=10 solution | | | | | | | | | | | | |
|---|---|---|---|---|---|---|---|---|---|---|---|---|
| Element | Bulk | 0 hour | 2 hours | 4 hours | 8 hours | 12 hours | 16 hours | 20 hours | 24 hours | 120 hours | 168 hours | 216 hours |
| O | 57.9 | 64.0 | 62.5 | 62.6 | 62.1 | 62.7 | 62.3 | 62.5 | 62.4 | 62.6 | 62.5 | 62.2 |
| Ca | 2.8 | 4.1 | 2.5 | 2.4 | 2.9 | 3.1 | 3.1 | 3.3 | 2.7 | 3.1 | 3.0 | 2.9 |
| Na | 11.2 | 6.6 | 4.9 | 4.7 | 4.7 | 4.6 | 4.6 | 4.9 | 4.5 | 4.5 | 4.3 | 4.7 |
| K | 0.5 | 2.1 | 1.8 | 2.2 | 1.8 | 1.4 | 1.5 | 1.3 | 1.9 | 1.8 | 1.9 | 2.1 |
| Mg | 1.2 | 2.1 | 1.8 | 2.0 | 1.8 | 1.9 | 1.4 | 1.7 | 1.4 | 1.7 | 1.8 | 1.7 |
| Al | 2.1 | 2.4 | 2.7 | 3.1 | 3.3 | 3.0 | 3.2 | 2.6 | 2.6 | 3.0 | 3.1 | 2.8 |
| B | 4.8 | 1.5 | 2.8 | 2.0 | 2.6 | 2.4 | 2.5 | 2.5 | 2.7 | 2.4 | 2.6 | 2.3 |
| Si | 19.4 | 17.2 | 21.0 | 21.0 | 20.8 | 20.9 | 21.3 | 21.2 | 21.8 | 20.9 | 20.8 | 21.3 |

| Element | 240 hours | 360 hours | 480 hours | 720 hours | 960 hours |
|---|---|---|---|---|---|
| O | 62.3 | 62.8 | 62.3 | 63.2 | 62.1 |
| Ca | 2.9 | 2.3 | 2.7 | 3.2 | 3.5 |
| Na | 4.5 | 4.9 | 5.0 | 4.8 | 4.1 |
| K | 2.2 | 1.4 | 1.6 | 1.6 | 1.8 |
| Mg | 2.1 | 1.9 | 1.5 | 1.2 | 1.0 |
| Al | 3.1 | 2.6 | 2.8 | 2.8 | 3.5 |
| B | 2.2 | 2.4 | 3.1 | 3.2 | 4.6 |
| Si | 20.7 | 21.7 | 21.0 | 19.9 | 19.3 |

# APPENDIX D. FITTED PARAMETERS OF XRR/XDS CURVES

Table D.1 Summary of Fitted Parameters of XRR/XDS Curves of SLS Glass Samples

| Summary of XRR/XDS Fitted Parameters (SLS Glass) | | | | | | | |
|---|---|---|---|---|---|---|---|
| Sample | Layer | Thickness (nm) | | RMS (nm) | | Density (g/cm$^3$) | |
| | | Value | Error | Value | Error | Value | Error |
| 0 hour | Sub | NA | NA | 0.89 | 0.05 | 2.43 | 0.01 |
| 1 hour | #1 | 2.75 | 0.82 | 3.59 | 0.18 | 2.33 | 0.10 |
| | Sub | NA | NA | 0.62 | 0.01 | 2.43 | 0.01 |
| 5 hours | #1 | 4.07 | 0.89 | 4.97 | 0.42 | 2.28 | 0.03 |
| | Sub | NA | NA | 0.75 | 0.10 | 2.44 | 0.01 |
| 10 hours | #1 | 5.02 | 1.23 | 6.39 | 0.21 | 2.24 | 0.02 |
| | Sub | NA | NA | 0.78 | 0.10 | 2.49 | 0.00 |
| 50 hours | #1 | 10.31 | 0.89 | 8.01 | 0.11 | 2.17 | 0.06 |
| | Sub | NA | NA | 0.71 | 0.10 | 2.44 | 0.04 |
| 100 hours | #1 | 15.7 | 0.4 | 10.49 | 0.11 | 2.22 | 0.01 |
| | Sub | NA | NA | 0.82 | 0.01 | 2.49 | 0.00 |
| 150 hours | #2 | 1.21 | 0.15 | 1.49 | 0.37 | 2.65 | 0.00 |
| | #1 | 16.48 | 1.83 | 14.26 | 0.57 | 1.99 | 0.01 |
| | Sub | NA | NA | 4.70 | 0.37 | 2.50 | 0.00 |
| 200 hours | #2 | 1.99 | 0.14 | 1.69 | 0.35 | 2.62 | 0.02 |
| | #1 | 17.29 | 1.91 | 14.14 | 0.33 | 1.90 | 0.06 |
| | Sub | NA | NA | 7.80 | 0.23 | 2.51 | 0.00 |
| 250 hours | #2 | 2.51 | 0.12 | 1.66 | 0.56 | 2.69 | 0.05 |
| | #1 | 18.55 | 1.70 | 14.40 | 0.62 | 1.95 | 0.03 |
| | Sub | NA | NA | 10.10 | 0.01 | 2.58 | 0.00 |

Table D.2 Summary of Fitted Parameters of XRR/XDS Curves of D263 Glass Samples

| Summary of XRR/XDS Fitted Parameters (D263 Glass) | | | | | | | |
|---|---|---|---|---|---|---|---|
| Sample | Layer | Thickness (nm) | | RMS (nm) | | Density (g/cm$^3$) | |
| | | Value | Error | Value | Error | Value | Error |
| 0 hour | Sub | NA | NA | 1.50 | 0.04 | 2.53 | 0.00 |
| 1 hour | #1 | 2.52 | 1.39 | 1.75 | 0.06 | 2.03 | 0.01 |
| | Sub | NA | NA | 1.27 | 0.24 | 2.46 | 0.00 |
| 5 hours | #1 | 2.95 | 0.79 | 2.71 | 0.07 | 2.03 | 0.02 |
| | Sub | NA | NA | 1.41 | 0.08 | 2.46 | 0.00 |
| 10 hours | #1 | 3.91 | 1.56 | 5.18 | 0.16 | 2.03 | 0.02 |
| | Sub | NA | NA | 1.34 | 0.12 | 2.55 | 0.08 |
| 50 hours | #1 | 8.31 | 0.47 | 7.12 | 1.14 | 2.05 | 0.01 |
| | Sub | NA | NA | 1.47 | 0.35 | 2.47 | 0.00 |
| 100 hours | #1 | 13.96 | 0.78 | 13.87 | 0.81 | 2.02 | 0.01 |
| | Sub | NA | NA | 1.51 | 0.04 | 2.50 | 0.00 |
| 150 hours | #1 | 22.91 | 0.59 | 15.44 | 0.11 | 2.00 | 0.03 |
| | Sub | NA | NA | 1.68 | 0.30 | 2.49 | 0.00 |
| 200 hours | #1 | 30.01 | 1.32 | 15.77 | 0.23 | 1.98 | 0.05 |
| | Sub | NA | NA | 1.58 | 0.23 | 2.52 | 0.00 |
| 250 hours | #2 | 3.63 | 1.26 | 1.48 | 0.13 | 2.78 | 0.04 |
| | #1 | 31.68 | 2.73 | 15.89 | 0.12 | 2.00 | 0.01 |
| | Sub | NA | NA | 7.90 | 2.32 | 2.58 | 0.02 |